Title
Electromagnetic Dissociation of 238U in Heavy-Ion Collisions at 120 MeV/A

Author
Justice, M.L.

Publication Date
1991-04-01

Lawrence Berkeley Laboratory
UNIVERSITY OF CALIFORNIA

Electromagnetic Dissociation of ^{238}U in Heavy-Ion Collisions at 120 MeV/A

M.L. Justice
(Ph.D. Thesis)

April 1991

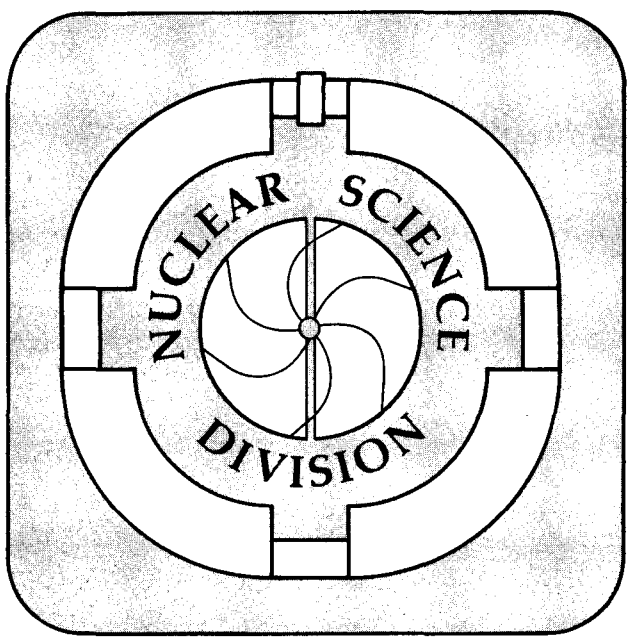

Prepared for the U.S. Department of Energy under Contract Number DE-AC03-76SF00098

DISCLAIMER

Electromagnetic Dissociation of ^{238}U in Heavy-Ion Collisions at 120 MeV/A

Marvin Lealon Justice

Ph.D. Thesis

Lawrence Berkeley Laboratory
University of California
Berkeley, CA 94720

April 1991

This work was supported by the Director, Office of Energy Research, Division of Nuclear Physics of the Office of High Energy and Nuclear Physics of the U.S. Department of Energy under Contract DE-AC03-76SF00098.

Abstract

This thesis describes a measurement of the heavy-ion induced electromagnetic dissociation of a 120 MeV/A ^{238}U beam incident on five targets: ^{9}Be, ^{27}Al, ^{nat}Cu, ^{nat}Ag, and ^{nat}U. Electromagnetic dissociation at this beam energy is essentially a two step process involving the excitation of a giant resonance followed by particle decay. At 120 MeV/A there is predicted to be a significant contribution ($\sim$ 25%) of the giant quadrupole resonance to the EMD cross sections.

The specific exit channel which was looked at was projectile fission. The two fission fragments were detected in coincidence by an array of solid-state ΔE-E detectors, allowing the charges of the fragments to be determined to within $\pm$.5 units. The events were sorted on the basis of the sums of the fragments' charges, acceptance corrections were applied, and total cross sections for the most peripheral events (*i.e.* those leading to charge sums of approximately 92) were determined. Electromagnetic fission at the beam energy of this experiment always leads to a true charge sum of 92. Due to the imperfect resolution of the detectors, charge sums of 91 and 93 were included in order to account for all of the electromagnetic fission events.

The experimentally observed cross sections are due to nuclear interaction processes as well as electromagnetic processes. Under the conditions of this experiment, the cross sections for the beryllium target are almost entirely due to nuclear processes. The nuclear cross sections for the other four targets were determined by extrapolation from the beryllium data using a geometrical scaling model.

After subtraction of the nuclear cross sections, the resulting electromagnetic cross sections are compared to theoretical calculations based on the equivalent photon approximation. Systematic uncertainties are discussed and suggestions for improving the experiment are given.

Contents

Acknowledgements

Many people contributed to the planning, setup, and execution of the experiment on which this thesis is based. I would like to take this opportunity to thank the entire collaboration: Yorick Blumenfeld, Nicola Colonna, Dimitri Delis, Giuseppe Guarino, Karl Hanold, Meng Jiangchen, Dick McDonald, Luciano Moretto, Graham Peaslee, and Gordon Wozniak. Without their hard work and dedication, this thesis would not have been possible. Thanks also to the operations staff at the BEVALAC for providing the beam and to the folks at the Silicon Detector Lab at LBL for their assistance with the detectors.

I would especially like to thank my thesis advisor, Prof. Luciano Moretto, along with the co-leader of the Moretto/Wozniak group, Dr. Gordon Wozniak, for welcoming me into their program at a time when I had seriously contemplated giving up graduate studies. Their support and encouragement helped to ease a difficult transition and restore my flagging self-confidence.

I would also like to thank Prof. Ken Crowe for his wise advice, and all the members of the Crowe/Rasmussen group for showing me the ropes as a beginning graduate student.

Grateful acknowledgements go to my thesis committee: Prof.'s Luciano Moretto, Darleane Hoffman, and Buford Price, for their instructive comments on how to improve this thesis, and also to my friend, Mark Karplus, for reading an early draft of the manuscript and making many useful suggestions.

Most of all, I would like to thank my parents, Marvin and Suzanne, my brother, Kirk, and my sister, Judy, for the moral support which they have given me over the many years. Without their love I would have given up a long time ago.

Finally, I would like to thank the taxpayers of the United States of America, past, present, and future, whose generous financial support made all this possible. This work was supported by the Director, Office of Energy Research, Division of Nuclear Physics of the the Office of High Energy and Nuclear Physics of the U.S. Department of Energy under Contract DE-AC03-76SF00098.

Chapter 1

Introduction

When two nuclei collide in such a manner that their volumes interpenetrate the reaction is dominated by the strong nuclear force. When they pass each other at larger distances the strong interaction is ineffective, due to its short range, but excitation of one or both of the nuclei can occur through the long range electromagnetic force. At high relative velocities the electromagnetic excitation of one nucleus by another is most conveniently described in the language of quantum electrodynamics, wherein the interaction is thought of as being mediated by the exchange of a virtual photon. Electromagnetic dissociation (EMD) occurs when one of the nuclei absorbs a virtual photon of sufficient energy to excite it above its particle emission threshold. The process is thus akin to ordinary photodisintegration, in which a nucleus decays through particle emission after absorption of a real photon, the difference being that, unlike real photons, virtual photons are not restricted to be transverse and massless. Moreover, the multipole spectrum of the virtual photons accompanying a heavy nucleus can be quite different from the multipole spectrum of a real photon beam.

More closely related to heavy-ion induced electromagnetic dissociation is the process of electrodisintegration, in which the source of virtual photons is a beam

of electrons (or positrons). Since the intensity of the virtual photon spectrum increases roughly as the Z^2 of the source, much larger cross sections can be observed for heavy-ion induced electromagnetic dissociation than for electrodisintegration. The electron is a much cleaner probe, however, since its interaction is purely electromagnetic, whereas one must contend with competing strong interaction processes in the analysis of a heavy-ion EMD experiment.

In addition to its Z^2 dependence, the virtual photon spectrum also depends upon the velocity of the source. As the source velocity increases, the spectrum hardens and becomes more intense. The consequence is that EMD cross sections for heavy-ions at ultrarelativistic energies, such as the 100 GeV/A Au + 100 GeV/A Au beams of the proposed RHIC collider, may be very large — of the order of 60 barns or more. Since such large fragmentation cross sections would constitute a major beam loss mechanism and be a source of unwanted background, a thorough understanding of EMD is called for on these grounds alone. On the other hand, the very high flux of virtual photons accompanying an ultrarelativistic heavy-ion could also be a potential source of interesting new physics. For example, the simultaneous absorption of more than one photon by a single nucleus, with subsequent decay into an exotic final state, might be observable [1]. Another possibility would be to use the virtual photons as a high luminosity source of γ-γ collisions [2]. The information gained on the virtual photon spectra from EMD experiments at currently accessible energies may be useful in preparing for these possibilities.

This thesis reports on an experimental study of the heavy-ion induced electromagnetic fission of a 120 MeV/A ^{238}U beam incident on a variety of targets, ranging from beryllium to uranium, in which the two fission fragments were detected in coincidence by an array of detector telescopes. Although higher energy EMD measurements have been made by others (see Chapter 3) there were some special features of this experiment that made it, potentially, unique. In particu-

lar, the contribution of the E2 multipole to the virtual photon spectrum, which is predicted to become equal to the E1 contribution at higher energies, is expected to be significantly enhanced in the energy region around 100 MeV per nucleon. Therefore, a careful measurement of EMD cross sections in this region could, in principle, provide a sensitive test of the most sophisticated calculations of the virtual photon spectra. In addition, while the virtual photon spectra extend out to higher energies as the beam energy is increased, the photodisintegration cross sections are dominated by the rather low energy, giant dipole and giant quadrupole resonances. For ^{238}U, which has a particularly strong photoabsorption cross section in the giant resonance region, the GDR and GQR peak at around 14 MeV and 10 MeV, respectively. The consequence is that this EMD experiment, which was the first to use uranium as both a target and a beam, measured cross sections comparable in magnitude to those observed in higher energy experiments with lower Z ions. Another unique feature was the choice of the fission exit channel. Most previous EMD measurements have been confined to processes in which the electromagnetically excited nucleus decays by emission of one or two nucleons.

Of course, in an experiment of this type, as in all EMD experiments, the same final state can be reached in non-electromagnetic interactions between the projectile and target. The assumption that is usually made in the analysis of EMD experiments is that the experimentally observed cross section is the sum of two terms:

$$\sigma_{\mathrm{EXP}} = \sigma_{\mathrm{EMD}} + \sigma_{\mathrm{NUC}} \ , \tag{1.1}$$

where σ_{NUC} is the contribution from strong interaction processes. The justification for Equation 1.1 lies in the short range of the nuclear force, which can contribute only when the two nuclei come into very close contact. At larger impact parameters, σ_{NUC} ceases to be important and the observed cross section is assumed to be entirely due to σ_{EMD}. Of course, in reality there will be a small but finite region of

impact parameters where both processes can occur. In this region the possibility of quantum mechanical interference exists and Equation 1.1 is no longer necessarily valid. The magnitude of such interference effects has been estimated with an idealized form of the nucleon-nucleon interaction, and was found to be at the level of less than one percent of the total cross section [3]. Quantum interference effects were neglected in the work presented in this thesis.

The presence of σ_{NUC} considerably complicates the analysis of any EMD experiment. The strategy adopted here was, first, to minimize its contribution by employing detectors which had the capability of providing charge identification of the two projectile fragments. Electromagnetic dissociation at the beam energy of this experiment is a low excitation energy phenomenon. Calculations presented in Section 2.4 show that the virtual photon energies involved are expected to be significantly lower than the $\sim$25 MeV threshold for the $^{238}\mathrm{U}(\gamma, pf)$ reaction. Thus, by requiring, in the off-line analysis, that the sum of the fragment charges add up to 92, all but the most peripheral nuclear-induced events can be removed. Due to the imperfect resolution of the detectors used in this experiment, the requirement had to be loosened to include charge sums of 91 and 93 in order to count all of the EMD events. Even with detectors of perfect resolution, however, one would not have been able to remove all of the nuclear events by placing a cut on the charge sum. For example, a single neutron can be knocked out of the projectile in a hard collision with a nucleon in the target. The subsequent fission of the residual $^{237}\mathrm{U}$ would be, for all intents and purposes, experimentally indistinguishable from the electromagnetic process.

The second part of the strategy, therefore, was to estimate the magnitude of the residual nuclear contribution by using as many different targets as possible. Arguments presented in the Appendix to this thesis show that, in contrast to the predicted Z^2 rise of σ_{EMD} with target atomic number, σ_{NUC} is expected to increase

much more slowly — more like $Z^{1/3}$. Therefore, by systematically varying the target material and including very light targets such as Be, where the EMD cross section is expected to be very small, the electromagnetic and nuclear contributions could be disentangled.

Chapter 2

Theoretical Background

2.1 Equivalent Photon Method

Classically, in the rest frame of one of the nuclei, the passage of the other appears as a brief pulse of electromagnetic radiation. Quantum mechanically, the interaction is viewed as proceeding through the exchange of one or more virtual photons. A connection between these two pictures is provided by the equivalent photon method, originally due to Fermi [4], in which the classical pulse of radiation is Fourier analyzed into a frequency spectrum of virtual photons. A good discussion of the equivalent photon method and its application to a wide variety of problems in heavy-ion physics can be found in the review article by Bertulani and Baur [1]. In this chapter the focus will be on the application of this method to the specific process in which a 120 MeV/A ^{238}U nucleus fissions after being electromagnetically excited by a target of charge Z_t. In the equivalent photon approximation the cross section is given by

$$\sigma_{\mathrm{EMD}} = \sum_{\pi l} \int d\omega \sigma^{\pi l}_{\gamma,f}(\omega)\, N^{\pi l}(\omega) \quad , \tag{2.1}$$

where $\sigma^{\pi l}_{\gamma,f}(\omega)$ is the fission cross section for *real* photons of energy ω and multipolarity πl, and $N^{\pi l}(\omega)$ is the number of virtual photons per unit energy and

multipolarity πl generated by the target. Calculations of the heavy-ion induced electromagnetic fission of ^{238}U have been done before [5,6], but only for energies, $E_{beam} \geq 1$ GeV/A.

2.2 Virtual Photon Spectra

The simplest form of the virtual photon spectrum is due to Weizsäcker and Williams [7] and is commonly referred to as the Weizsäcker-Williams approximation. In this approximation, a complete derivation of which can be found in the text by Jackson [8], the source of the virtual photons (the target in this experiment) is assumed to move along a straight-line trajectory at an impact parameter, b, past a non-recoiling absorbing system (the projectile in this experiment). The electromagnetic field generated by the target is approximated by two pulses of plane-polarized radiation, one in the beam direction, and the other perpendicular to it. A Fourier decomposition of the pulses is then made, and the various frequency components are equated to a spectrum of virtual photons. The resulting number spectrum of virtual photons for a given impact parameter is given by

$$n^{\pi l}(\omega, b) = \frac{Z_t^2 \alpha}{\pi^2} \frac{\omega}{\beta^4 \gamma^2} \left[K_1^2(x) + \frac{1}{\gamma^2} K_0^2(x) \right] \quad , \tag{2.2}$$

where

$$\begin{aligned} Z_t &= \text{charge of the target,} \\ \alpha &= \text{fine structure constant,} \\ \beta &= \text{projectile velocity,} \\ \gamma &= 1/\sqrt{1-\beta^2}, \\ x &= \omega b/\beta\gamma, \\ K_0(K_1) &= \text{modified Bessel function of order zero(one).} \end{aligned}$$

Integrating over impact parameters gives

$$N^{\pi l}(\omega) = 2\pi \int_{b_{min}}^{\infty} n^{\pi l}(\omega, b)\, b db$$
$$= \frac{2Z_t^2\alpha}{\pi\omega\beta^2}\left[\xi K_0(\xi) K_1(\xi) - \frac{\beta^2\xi^2}{2}\left(K_1^2(\xi) - K_0^2(\xi)\right)\right] , \quad (2.3)$$

where $\xi = \omega b_{min}/\beta\gamma$ and b_{min} is the cutoff impact parameter, below which nuclear processes take over and electromagnetic dissociation ceases to be important.

Since a plane-wave approximation to the electromagnetic field is made in the Weizsäcker-Williams approximation, all multipolarities are weighted equally in the resulting virtual photon spectrum. An approach that goes beyond the plane-wave approximation was given by Alder and Winther [9], and later put into the context of the virtual photon language by Bertulani and Baur [10]. In this approach, a proper multipole expansion of the electromagnetic field is made and an analytical expression for the equivalent photon numbers of all multipolarities is obtained. The general expression is quite complicated and will not be given here. The most important multipolarities are E1, E2, and M1. The expression for the E1 virtual photon spectrum is the same as the Weizsäcker-Williams expression, Equation 2.3, while the E2 spectrum is given by

$$N^{E2}(\omega) = \frac{2Z_t^2\alpha}{\pi\omega\beta^4}\left[2\left(1-\beta^2\right)K_1^2 + \left(2-\beta^2\right)^2 \xi K_0 K_1 - \frac{\xi^2\beta^4}{2}\left(K_1^2 - K_0^2\right)\right] , \quad (2.4)$$

where all K's are functions of ξ as in Equation 2.3. In the limit $\beta \to 1$, Equation 2.4 is seen to become equivalent to Equation 2.3. In fact, this is true in general; as the velocity of the projectile approaches the speed of light, the virtual photon spectra for all multipolarities become equivalent to the E1 spectrum. At 120 MeV/A, however, where the velocity is only approximately half the speed of light, the E2 spectrum, as given by Equation 2.4, is substantially enhanced in comparison to the E1 spectrum. The M1 spectrum, on the other hand, is slightly less intense than the E1 spectrum at this velocity. Since the cross section for

absorption of an M1 photon is much smaller than the corresponding cross section for an E1 photon, the M1 contribution was neglected in the calculations presented in this chapter.

In order to do calculations with Equations 2.3 and 2.4, a choice of the cutoff impact parameter, b_{min}, had to be made. One possibility was to use the simple parameterization of the hard-sphere model:

$$b_{min} = r_0 \left(A_p^{1/3} + A_t^{1/3} \right) \quad . \tag{2.5}$$

But, since real nuclei are not simple hard-spheres, a better parameterization is expected to be [11]:

$$b_{min} = r_0 \left(A_p^{1/3} + A_t^{1/3} - d \right) \quad , \tag{2.6}$$

where d is a small constant introduced to allow for the diffuse skin surrounding the nuclear core. This parameterization, with $r_0 = 1.35$ fm and $d = .83$, has been used in the analysis of previous EMD experiments [12,13]. A different parameterization was suggested by the authors of reference [3], who claim that d should be allowed to vary as a function of A_p and A_t. Their parameterization, which was obtained from a fit to Glauber model calculations for a variety of projectile-target combinations at 1.05 GeV/A, is

$$b_{min} = 1.34 \left[A_p^{1/3} + A_t^{1/3} - .75 \left(A_p^{-1/3} + A_t^{-1/3} \right) \right] \quad . \tag{2.7}$$

The b_{min} values calculated from Equations 2.6 and 2.7 for a ^{238}U projectile incident on the five targets used in this EMD experiment are listed in Table 2.1. The E1 and E2 virtual photon spectra obtained from Equations 2.3, 2.4, and 2.7, for the case of 120 MeV/A ^{238}U + ^{238}U, are displayed as the dashed curves in Figure 2.1. The arrow in this figure and subsequent figures of this chapter marks the 5.8 MeV fission threshold of ^{238}U. The virtual photon spectra calculated with the alternative b_{min} parameterization of Equation 2.6 are about 15% higher than those shown in the figure.

target	$b_{min}^{(2.6)}$	$b_{min}^{(2.7)}$
Be	10.05	10.45
Al	11.30	11.83
Cu	12.62	13.22
Ag	13.67	14.31
U	15.61	16.28

Table 2.1: b_{min} values in fm from Equations 2.6 and 2.7.

In the derivations of Equations 2.3 and 2.4, the projectile was assumed to move in a straight line past the target. While this may be a good assumption at very high energies, at 120 MeV/A a uranium nucleus will be slightly deflected by the Coulomb field of the target. Assuming it follows a classical Rutherford trajectory, the relationship between the distance of closest approach, ρ, and the impact parameter, b, is given by

$$\begin{aligned} \rho &= \left(b^2 + a^2\right)^{1/2} + a \\ &\approx b + a \ , \end{aligned} \tag{2.8}$$

where

$$a = \frac{Z_p Z_t e^2}{\mu \beta^2 \gamma} \ , \tag{2.9}$$

μ is the reduced mass of the projectile and target, β is the projectile velocity, and $\gamma = 1/\sqrt{1-\beta^2}$. For 120 MeV/A ^{238}U + ^{238}U, a = .45 fm, with correspondingly smaller values for the lighter targets. Bertulani and Baur [1] have studied in detail the effects of Rutherford bending on the virtual photon spectra. They were able to obtain an analytical expression for $N^{E1}(\omega)$ that is, nevertheless, much more complicated than Equation 2.3. For other multipolarities they were unable to express the results in closed form. However, they claim that their complicated

expressions are well approximated by a simple rescaling of the straight-line b_{min} values as follows:

$$b_{min} \longrightarrow b_{min} + \frac{\pi}{2}a \ . \tag{2.10}$$

The virtual photon spectra calculated with this rescaling correction are shown as the solid curves in Figure 2.1.

While the effects of Coulomb deflection on the virtual photon spectra have been studied in detail by the theorists, the effects of nuclear deformation have been completely ignored. In all of the theoretical papers that this author has seen, the nuclear charge distributions are assumed to be spherically symmetric. A ^{238}U nucleus, however, is known to have the shape of a prolate ellipsoid. In fact, from the splitting of the giant dipole resonance in ^{238}U (see Equation 2.12 and Figure 2.2), the difference in the lengths of the major and minor axes of the ellipsoid can be estimated to be $\sim 30\%$. For a deformed projectile incident on a spherical target, the effect of the deformation would enter through a dependence of the cutoff impact parameter on the particular orientation of the projectile. In the case where the target is also deformed, there could be an additional effect on the electromagnetic field generated by the target. A proper treatment of these effects would involve an averaging over the various possible orientations of the projectile and target. The averaging problem appears to be quite complicated, but perhaps some enterprising theorist might want to consider it.

2.3 Photofission Cross Sections

The other ingredients that are needed to calculate $\sigma_{\rm EMD}$ with Equation 2.1 are the ^{238}U photofission cross sections, $\sigma^{\pi l}_{\gamma,f}(\omega)$. The total photofission cross section,

$$\sigma_{\gamma,f}(\omega) = \sum_{\pi l} \sigma^{\pi l}_{\gamma,f}(\omega) \ , \tag{2.11}$$

along with the total photonuclear cross section, $\sigma_\gamma(\omega)$, was measured by Caldwell *et al.* [14] over the photon energy range, $\omega = 5.8$ to 18.3 MeV. In their paper, a fit was made to $\sigma_\gamma(\omega)$ with a double Lorentzian:

$$\sigma_\gamma(\omega) = \sigma_1 \frac{(\omega\Gamma_1)^2}{(\omega^2-\omega_1^2)^2+(\Gamma_1\omega)^2} + \sigma_2 \frac{(\omega\Gamma_2)^2}{(\omega^2-\omega_2^2)^2+(\Gamma_2\omega)^2} \ , \tag{2.12}$$

characteristic of the giant dipole resonance in a permanently deformed nucleus such as ^{238}U. No parameterization of $\sigma_{\gamma,f}(\omega)$ was given, however, so the author of this thesis had to construct his own.

The relationship between $\sigma_{\gamma,f}(\omega)$ and $\sigma_\gamma(\omega)$ is given by

$$\sigma_{\gamma,f}(\omega) = P_f(\omega)\,\sigma_\gamma(\omega) \ , \tag{2.13}$$

where $P_f(\omega)$ is the fission probability as a function of photon energy, ω. Therefore, a parameterization of $P_f(\omega)$ was sought. From just above threshold to $\sim$12.3 MeV, $P_f(\omega)$ is known to be nearly constant, with a value of .22 [14,15]. At around 12.3 MeV, however, the (γ, nf) reaction becomes energetically possible and $P_f(\omega)$ rises sharply† to a value of $\sim$.4 [15]. To obtain a smooth transition between the two regions, the following form was used:

$$P_f(\omega) = a - \frac{b}{1+e^{(\omega-c)/d}} \ , \tag{2.14}$$

with $a = .4$, $b = .18$, $c = 13.4$ MeV, and $d = .59$ MeV. A plot of $\sigma_{\gamma,f}(\omega)$ obtained with this parameterization is shown in Figure 2.2, which fairly represents the data of reference [14].

Since what is measured in a photofission experiment is a sum over multipoles, some additional information is needed in order to extract the $\sigma^{\pi l}_{\gamma,f}(\omega)$. In principle, electrofission or hadron-induced fission experiments can provide this information.

† Somewhere around 19 MeV the $(\gamma, 2nf)$ reaction becomes possible and $P_f(\omega)$ should rise again. However, it was found that, even if P_f was set equal to unity in this region, the contribution of virtual photons above 19 MeV to the EMD cross sections was negligible.

For ^{238}U, however, there has been some controversy over the E2 contribution as deduced from these two methods (see reference [16] and references therein). While not wishing to enter into this controversy, the author of this thesis has estimated $\sigma_\gamma^{E2}(\omega)$ as follows. First, the E2 photoabsorption cross section was assumed to be of the form [17] :

$$\sigma_\gamma^{E2}(\omega) = \frac{8\pi^3\alpha}{150(\hbar c)^2}\,\omega^3\,\frac{dB^{E2}}{d\omega} \quad , \tag{2.15}$$

with the following form for the strength function, $dB^{E2}/d\omega$,

$$\frac{dB^{E2}}{d\omega} = \frac{K}{\omega}\frac{\Gamma^2}{\left(\omega^2-\omega_0^2\right)^2+\omega^2\Gamma^2} \quad . \tag{2.16}$$

K was determined by assuming that the E2 cross section exhausts 100% of the energy-weighted sum rule [17] :

$$\int \frac{d\omega}{\omega^2}\sigma_\gamma^{E2}(\omega) = \frac{\pi^2\alpha Z^2}{3AMc^2}\left\langle R^2\right\rangle \quad , \tag{2.17}$$

where M is the nucleon mass, Z and A are the charge and mass number of ^{238}U, and $\langle R^2\rangle$ is its mean square charge radius. Inserting Equations 2.15 and 2.16 into this sum rule gives

$$\int d\omega\omega\frac{dB^{E2}}{d\omega} = \frac{25\hbar^2Z^2}{4\pi AM}\left\langle R^2\right\rangle \quad , \tag{2.18}$$

or

$$\frac{\pi\Gamma}{2\omega_0^2}K = \frac{25\hbar^2Z^2}{4\pi AM}\left\langle R^2\right\rangle \quad . \tag{2.19}$$

The numerical value of the right hand side of this equation was taken to be 1.00×10^5 MeV fm^4 [18]; ω_0 and Γ were taken to be 10 MeV and 3.5 MeV, respectively [19]. The result is

$$K = 1.819\times10^6\ \text{fm}^4\ \text{MeV}^2 \quad . \tag{2.20}$$

Finally, to get the E2 photo*fission* cross section:

$$\sigma_{\gamma,f}^{E2}(\omega) = P_f^{E2}(\omega)\sigma_\gamma^{E2}(\omega) \quad , \tag{2.21}$$

the same parameterization was used for $P_f^{E2}(\omega)$ as was used for $P_f(\omega)$. The final result of the calculation of $\sigma_{\gamma,f}^{E2}(\omega)$ is shown in Figure 2.3. Note the different scales of this figure and Figure 2.2. The E2 photofission cross section is roughly two orders of magnitude smaller than the total photofission cross section, which is almost entirely E1. However, since there are roughly two orders of magnitude more E2 than E1 virtual photons generated by the targets in this experiment, the E2 multipole can make a significant contribution to the EMD cross sections.

For the $\sigma_{\rm EMD}$ calculations presented below, it was assumed that the total photofission cross section of Figure 2.2 is composed of E1 and E2 multipoles only. The E1 cross section was then obtained by subtraction:

$$\sigma_{\gamma,f}^{E1}(\omega) = \sigma_{\gamma,f}(\omega) - \sigma_{\gamma,f}^{E2}(\omega) \ . \tag{2.22}$$

2.4 EMD Predictions

The equivalent photon spectra of Section 2.2 were folded together with the $\sigma_{\gamma,f}^{\pi l}(\omega)$ of Section 2.3, using numerical integration techniques, to obtain predictions for $\sigma_{\rm EMD}$ as a function of Z_t. The upper and lower integration limits were taken as 5.8 and 25 MeV, respectively, although the contribution above 20 MeV was found to be negligible. The results of calculations made with the b_{min} parameterization of Equation 2.7 are shown in Figure 2.4 where the solid/dashed curves are the results with/without the recoil correction of Equation 2.10.

For comparison, the results of a straightforward Weizsäcker-Williams calculation, with no recoil correction, are shown as the dot-dash curve in the figure. Since all multipolarities are weighted equally in this approximation, $N^{\pi l}(\omega)$ can be pulled out of the sum in Equation 2.1 :

$$\sigma_{\mathrm{EMD}}^{WW} = \int d\omega \sum_{\pi l} N^{WW}(\omega)\, \sigma_{\gamma,f}^{\pi l}(\omega)$$
$$= \int d\omega N^{WW}(\omega)\, \sigma_{\gamma,f}(\omega) \quad . \tag{2.23}$$

Consequently, one can use the total photofission cross section without worrying about its multipole decomposition. The predicted cross sections from all three calculations for the specific targets used in this experiment are listed in Table 2.2, where σ^{rc}/σ^{nrc} denote the cross sections calculated with/without the recoil correction.

From the figure and the table it is seen that the multipole expansion method predicts significantly larger cross sections than the Weizsäcker-Williams approximation. The inclusion of the recoil correction, on the other hand, cancels out much of the enhancement. The sensitivity of the predictions to b_{min} was tested in calculations with the parameterization of Equation 2.6; the results are given in Table 2.3. Comparing with Table 2.2, one sees that the the smaller b_{min} values have shifted all the calculations upward by about 15%.

Another quantity of interest is the mean energy of the absorbed virtual photon, defined as

$$\langle \omega_\gamma \rangle = \frac{\sum_{\pi l} \int d\omega \omega \sigma_{\gamma,f}^{\pi l}(\omega)\, N^{\pi l}(\omega)}{\sum_{\pi l} \int d\omega \sigma_{\gamma,f}^{\pi l}(\omega)\, N^{\pi l}(\omega)} \quad . \tag{2.24}$$

The predicted $\langle \omega_\gamma \rangle$ values are listed in Table 2.4. The dependence upon the specific b_{min} parameterization was found to be negligible.

target	σ^{rc}	σ^{nrc}	σ^{WW}
Be	4	5	4
Al	34	37	28
Cu	122	137	102
Ag	251	284	212
U	625	722	538

Table 2.2: σ_{EMD} predictions in mb.

target	σ^{rc}	σ^{nrc}	σ^{WW}
Be	5	5	4
Al	38	42	31
Cu	139	156	116
Ag	288	326	243
U	717	830	619

Table 2.3: Same as Table 2.2 only with the b_{min} parameterization of Equation 2.6.

target	$\langle\omega_\gamma\rangle^{rc}$	$\langle\omega_\gamma\rangle^{nrc}$	$\langle\omega_\gamma\rangle^{WW}$
Be	10.5	10.6	11.1
Al	10.4	10.4	10.9
Cu	10.2	10.3	10.7
Ag	10.1	10.1	10.6
U	9.9	10.0	10.3

Table 2.4: Mean virtual photon energies in MeV.

Chapter 3

Previous EMD Measurements

The first experimental evidence of the EMD process was seen in the cosmic ray experiments of Balasubrahmanyan *et al.* [21], who studied the absorption of high energy carbon and oxygen nuclei in a tungsten detector which had been carried to high altitudes aboard a balloon. Their data showed that, as the incident energy increased from 2 GeV/A to 15 GeV/A, the mean free paths of both the C and O nuclei decreased by a factor of ~ 2.5, but they were unable to come up with a plausible explanation for their observations. Soon afterwards, however, Artru and Yodh [22] postulated that electromagnetic fragmentation might be the explanation and were able, at least qualitatively, to account for the experimental results with a calculation based on the Weizsäcker-Williams approximation. In their paper, published in 1972, they suggested that confirmation of the EMD effect could be made at the BEVALAC which, at that time, was just beginning to accelerate test beams.

When heavy-ion beams became available on a regular basis at the BEVALAC, Heckman and Lindstrom [23] were able to confirm the existence of electromagnetic dissociation in experiments with 1.2 and 2.1 GeV/A ^{12}C and ^{16}O beams incident on a variety of targets, ranging from hydrogen to lead. Using a single-arm mag-

netic spectrometer with time-of-flight and dE/dx measurements, they measured the total cross sections for several projectile fragmentation channels and found a significant enhancement in the heavier target data for the processes in which only a single nucleon was removed. In order to subtract out the nuclear-induced component, they introduced the concept of factorization, which has been used in most subsequent EMD experiments.

For the process in which a fragment, F, is produced in a peripheral nuclear reaction between a projectile, P, and a target, T, factorization says that the cross section should be given by

$$\sigma_{\mathrm{NUC}}(P,T,F) = \gamma_P^F \gamma_{PT} \ , \tag{3.1}$$

where γ_P^F depends only on the projectile-fragment combination and γ_{PT} depends only on the projectile-target combination. In the geometrical model of the Appendix, γ_{PT} corresponds to (see Equation A.1):

$$\gamma_{PT} = 2\pi \left(b_{min}\,(P,T) - \frac{\Delta b}{2} \right) \tag{3.2}$$

and γ_P^F corresponds to:

$$\gamma_P^F = \Delta b \ . \tag{3.3}$$

Heckman and Lindstrom determined the γ_{PT} from fragmentation channels in which two or more nucleons were removed since, under the conditions of their experiments, electromagnetic dissociation was expected to have a negligible contribution to those processes. The γ_{PT} values determined in this manner were found to be proportional to:

$$\gamma_{PT} \propto A_P^{1/3} + A_T^{1/3} - 0.8 \ , \tag{3.4}$$

which is essentially the form suggested by the geometrical model. After subtraction of the empirically determined σ_{NUC} values from the single nucleon removal

cross sections, the authors compared the remainder to a Weizsäcker-Williams calculation and found good agreement, although their error bars were somewhat large.

Further EMD experiments at the BEVALAC were done by Westfall *et al.* [12] and Olson *et al.* [24]. In the first of these experiments, charge-changing cross sections of a 1.88 GeV/A ^{56}Fe beam incident on targets ranging from hydrogen through uranium were measured, and an EMD enhancement was observed for the $\Delta Z = 1$ channel in the high Z targets. Since no photonuclear data were available on the $^{56}\mathrm{Fe}(\gamma, p)^{55}\mathrm{Mn}$ reaction, the authors used a model, based on GDR sum rules, to predict the Fe photoabsorption cross section. From their data and a Weizsäcker-Williams calculation, they were then able to determine the branching ratio for proton emission. In Olson's experiment, EMD enhancements were seen in the $1p$, $1n$, and $2n$ removal channels of a 1.7 GeV/A ^{18}O beam incident on nine targets ranging from Be to U. Factorization was used to remove the nuclear contribution and the Z_{targ} dependence of the remainder was found to be given by

$$\sigma_{\mathrm{EMD}} \propto Z_{targ}^{1.8} \ , \tag{3.5}$$

in agreement with a Weizsäcker-Williams calculation in which a b_{min} parameterization similar to Equation 2.6 was used.

In contrast to the above experiments, which all measured the fragmentation of the projectile, a series of experiments by J.C. Hill and coworkers has studied the process in which the target is fragmented by virtual photons from the beam. Using radiochemical techniques, they have measured EMD cross sections for single neutron removal from ^{89}Y and single and double neutron removal from ^{59}Co and ^{197}Au with a variety of beams from the BEVALAC [25-29], and $1n$ removal from ^{197}Au with 60 and 200 GeV/A ^{16}O beams at CERN [27]. These authors have been the only ones to date to report significant deviations from theory. Their

claim is that the Weizsäcker-Williams approximation overpredicts $\sigma_{\rm EMD}$ for high Z projectiles and underpredicts $\sigma_{\rm EMD}$ at CERN energies.

Further measurements with the ultrarelativistic CERN beams were made by Price *et al.* [13], Brechtmann *et al.* [30,31], and Baroni *et al.* [33]. All of these experiments used nuclear track detectors — CR-39 plastic in the case of Price and Brechtmann, nuclear emulsion in the case of Baroni. In their experiment with a 200 GeV/A ^{32}S beam incident on Al, Cu, and Pb, the authors of reference [13] were the first to measure EMD enhancement for fragmentation channels in which up to 8 charges were removed from the projectile. Their measurement of $\sigma_{\rm EMD} = 4573$ mb for the sum production of $Z = 8$ through $Z = 15$ fragments with the Pb target, which was confirmed by the authors of reference [31], is the highest EMD cross section reported so far.

Finally, there have been two recently published papers on EMD experiments with 14.5 GeV/A ^{28}Si beams from the Brookhaven AGS [32,34]. The experiment of reference [34], which employed a magnetic spectrometer and a complex detector system, was unique in that an attempt was made to measure both the heavy fragment *and* the light particles resulting from electromagnetic dissociation. In addition, detectors were placed near the target to veto nuclear events in which the target was substantially perturbed. Their results, and the results of reference [32], were found to be consistent with the Weizsäcker-Williams approximation.

Chapter 4

Experimental Apparatus

4.1 Beam

The data presented in this thesis were all collected at the Lawrence Berkeley Laboratory's BEVALAC in November of 1989. The ^{238}U beam was first accelerated to an energy of 8.5 MeV/A and stripped to a charge state of 68^{+} at the SuperHILAC before being transferred to the Bevatron, where it was subsequently accelerated to the final energy of 120 MeV/A. The BEVALAC operates in a pulsed mode, delivering 15 pulses of particles or 'spills' per minute to the experimental area. The beam intensity on target for this experiment varied between 5×10^5 and 1×10^6 particles/spill, with a typical spill length of 300 to 500 msec.

In addition to the uranium beam used for data runs, several other beams were used to calibrate the detectors. Maximum use was made of the short time available for calibrations by exploiting the ability of the BEVALAC to provide 'cocktail' beams, in which two ions with very nearly the same charge-to-mass ratio are simultaneously accelerated and delivered to the experimental area. Doublet beams of 80 MeV/A ($^{28}Si^{9+}$,$^{56}Fe^{18+}$) and 80 and 120 MeV/A ($^{86}Kr^{20+}$,$^{129}Xe^{30+}$) were accelerated after the completion of data taking, and used for calibration

purposes.

4.2 Scattering Chamber

Upon extraction from the Bevatron, the beam was delivered to the 60″ diameter scattering chamber at the end of Beamline 44. To prevent interactions of the beam and beam fragments with atmospheric gas atoms, a vacuum of $< 10^{-4}$ torr was maintained inside the scattering chamber by a diffusion pump.

4.3 Collimation

Since the primary purpose of this experiment was to detect projectile fragments at small forward angles, it was necessary to collimate the beam. The collimator consisted of a 26″ long stainless steel cylinder with a 2.5″ outer diameter. The upstream end of the cylinder fit into a 3″ thick Al plate which, in turn, fit inside the port between the scattering chamber and beam pipe. Inside the cylinder were two annular rings of 3/16″ tantalum. This thickness was sufficient to stop ^{238}U beam particles along with any other high Z particles created upstream in the beam transport system. The first ring was at the upstream end of the cylinder, approximately 30″ from the target, and had a 3/8″ circular hole cut in its center to allow good beam particles to pass through. The downstream ring was about 5″ from the target and had a 1/2″ diameter hole. Light particles and neutrons were not stopped by this collimation system and were even generated by it, but since the thresholds of the detectors were set high for fission fragments, they created negligible background problems.

4.4 Telescope Arrays

At the heart of the detection system were the 16 position-sensitive ΔE-E-Plastic telescopes [35] used to detect the projectile fragments. Each telescope was comprised of a Si ΔE detector, followed by a Si(Li) E detector, followed by a plastic scintillator. They were arranged in two rings of eight telescopes each, placed concentrically about the beam as shown in Figure 4.1. The upstream ring intersected the beam axis 37.0 cm downstream of the target and covered the angular region of approximately $4.5° \leq \theta \leq 13.5°$, while the downstream ring intersected the beam axis 103.2 cm downstream of the target and covered approximately $1.5° \leq \theta \leq 4.5°$. The positions of the detectors with respect to the target were carefully surveyed before data taking and are estimated to be known to within ±2 mm.

As it turned out, the projectile fragments of interest were almost entirely concentrated in the downstream detectors. Of the eight telescopes in this array, one, D4, was not functioning properly at the time of the experiment, and the data from another, D6, could not be used in the final analysis because its gains had shifted between the data runs and the calibration runs. Removal of these two detectors from the analysis had the effect of reducing the acceptance for coincidence events from ~40% to ~20%. The quantity of data in the six remaining downstream telescopes, however, was such that the statistical uncertainties in the final results are negligible when compared to the systematic problems.

4.4.1 ΔE detectors

The ΔE detectors were ~ 300 μm thick, diffused junction n^+p Si diodes. Each detector had an outside dimension of 5.08 cm × 5.08 cm with an active area of 4.48 cm × 4.48 cm. Their absolute thicknesses were determined to ±10 μm

from capacitance measurements at the Silicon Detector Laboratory at LBL, and ranged from a minimum of 240 μm for detector D8 to a maximum of 365 μm for detector U5. Most of the detectors had reasonably uniform thicknesses across their faces, but some were found to vary by as much as 8%, especially near the edges. The non-uniformities were determined from a combination of capacitance measurements and calibration beams, and appropriate corrections were applied in the analysis.

A reverse bias voltage of +60 to +140 V was applied to the Au ohmic contact on the n^+ side of each ΔE detector, creating a depletion layer which extended essentially throughout its entire volume. The contact on the p side was divided into fifteen 2.42 mm wide, high conductivity strips separated by .607 mm wide, high resistivity gaps to give position information through the technique of resistive charge division. Electrons created by the passage of charged particles through the detector were collected at the n^+ contact giving a signal, Q_{tot}, proportional to the total amount of energy deposited. The holes, on the other hand, were collected through the p contact, one end of which was terminated through 50Ω. For a particle incident at a position, X, measured from the terminated end, the amount of charge exiting through the other end and reaching the preamp was (neglecting non-linearities) Q_{tot}X/L, where L is the total length of the detector (4.48 cm). X could then be determined off-line by dividing the position signal by the ΔE signal. Since all of the resistance appeared between the high conductivity strips, the position signals were discrete. This had the disadvantage of limiting the resolution to half the width of a strip plus a gap ($\sim$ 1.5 mm), but had the important advantage that the position signals were self-calibrating.

4.4.2 E detectors

The E detectors were ~ 5 mm thick, lithium drifted, Si(Li) diodes fabricated on p-type silicon, with the same outer dimensions as the ΔE's. As in the ΔE's, a thin layer of Au was deposited on one face to serve as the n contact while the opposite, p, contact was divided up into strips and gaps of high and low conductivity. The strips of the E detectors were rotated 90° with respect to the ΔE strips to give position information in the orthogonal, Y, direction. Reverse bias potentials of +600 V were needed to fully deplete these detectors. Monte Carlo studies showed that the 5 mm thickness was sufficient to stop beam fragments of $Z \geq 28$ for the beam energy of this experiment. For particles stopping in the detector, the total negative charge collected through the n contact gave a measure of the total energy deposited, while the amount of positive charge collected through the resistor-divider p contact allowed the Y position to be determined.

4.4.3 Plastic Detectors

Light particles of sufficient energy to punch through the silicon detectors were registered by the third stage of the detector telescopes: 7.6 cm thick, 5.2 cm $\times$ 5.2 cm, fast plastic scintillators coupled to RCA 2060 photomultiplier tubes. Since no light charged particles are expected to accompany the electromagnetic fission process, these detectors were not used in the main stage of the data analysis. They were useful as veto counters in certain steps of the calibrations, however.

4.5 PPAC's

When this experiment was originally proposed, the calculations presented in Chapter 2 had not yet been done, hence there were no firm theoretical predictions for

the magnitude of the electromagnetic fission cross section for ^{238}U projectiles incident on a U target at 120 MeV/A. However, at the time, it did not seem implausible that it could be large enough so that there would be an appreciable probability for events to occur in which both the projectile *and* the target absorb virtual photons of sufficient energy to undergo fission. In order to measure the energies, positions, and relative time-of-flights of the target fission fragments in these '4-fold' events, the target was surrounded with four 20 cm × 24 cm parallel plate avalanche counters (PPAC's). As it turned out, the EMD cross sections were low enough so that the few 4-fold events which were observed were completely dominated by nuclear processes, in which the sum charges of the two projectile fragments added up to less than 92. Although the PPAC's were not so useful for their original purpose, they did provide important confirming evidence of the low Z contaminant in the uranium target (see Section 6.1.2).

4.6 Targets

The targets used in this study are listed in Table 4.1. They were chosen to cover as wide a range in Z as possible. There is a noticeable gap between Ag and U, however, which was not possible to fill in due to time limitations. The five targets (along with an empty target frame for target-out runs) were mounted simultaneously on a target ladder. The vertical position of the ladder was continuously adjustable through a small d.c. motor controlled from the counting room, allowing the targets to be changed quickly without opening the scattering chamber.

For the light targets (Be, Al, Cu, and Ag), the thicknesses were chosen based on considerations of event rate and what was readily available. The U target was prepared specifically for this experiment; its thickness was chosen to minimize multiple scattering and energy loss of the target fission fragments for the 4-fold

target	Z	mg/cm^2
^{9}Be	4	2.60
^{27}Al	13	6.46
^{nat}Cu	29	4.79
^{nat}Ag	47	5.31
^{nat}U	92	1.33

Table 4.1: Targets

events, while still giving an acceptable event rate. To further minimize the amount of material through which the target fission fragments had to pass, the target ladder was rotated 40° away from normal incidence for the U target runs. The thicknesses of all the targets were written on their individual frames at the time of manufacture. As a check, the Al, Cu, and Ag targets were carefully weighed to within $\pm.5\%$ after the experiment. The Cu and Ag thicknesses agreed well with the values on their frames, but it was found that the true thickness of the Al target was $\sim 20\%$ higher than the frame value. It was not possible to weigh the Be target, so the value written on its frame had to be accepted on faith.

The U target was made by evaporating a known weight of natural uranium onto an aluminum backing. Supposedly, the backing was then etched away, leaving a free standing U target. In the data taken with this target, however, there is a sizeable number of events which appear to have come from a low Z contaminant. The most likely hypothesis is that the etching was not complete and a residual layer of aluminum remained on the surface. More details on the effect of the contaminant on the data are given in Section 6.1.2. Unfortunately, the U target was accidentally destroyed shortly after the experiment, so it was not possible to go back and determine its precise composition.

4.7 Beam Flux Monitor

The absolute beam flux was measured with a 1/4″ plastic scintillator paddle located just downstream of the thin Al exit window of the scattering chamber. Due to the high instantaneous rate ($\geq 5 \times 10^6$ s^{-1}) of incident beam particles, it was necessary to attenuate the flux hitting the scintillator by covering its front surface with a Pb mask 'sieve' — a 1/4″ thick sheet of Pb with an array of small holes drilled through it. The holes transmitted only $\sim$10% of the beam, thereby reducing the count rate to a manageable level. The drawback was that the exact transmission factor of the mask had to be determined (see Section 5.5). After passing through a discriminator, the logic pulses from the scintillator were split — one signal going directly to a scaler while another was gated by a $\overline{\text{BUSY}}$ signal before going to a different scaler. In this manner, the deadtime could be monitored on-line.

4.8 Electronics and Data Acquisition

A simplified schematic of the trigger electronics is shown in Figure 4.2. Although the main goal of this experiment was to detect two projectile fragments in coincidence, singles events were also written to tape in order to accumulate statistics for the Z calibrations. The tradeoff was a loss of coincidence statistics due to deadtime, which reached a maximum of around 30% for the Al target.

A valid event was defined at the hardware level as a coincidence within roughly 100 ns between the E and ΔE of any one of the 16 telescopes. In order to compress as much as possible the data written to tape, a bit register was used to indicate to the data acquisition system which detectors needed to be read out. The bit indicating that a given detector was to be read out was set by a 3-way OR between

the E, ΔE, and plastic, allowing some information on accidental background and light particles below the E and ΔE thresholds to be gathered.

The front end of the data acquisition system was a VME based microprocessor. The data were read from CAMAC by a VME crate and shipped via a local Ethernet to a VAX 11/780 where they were written to tape. Real-time samples were displayed on terminals in the experimental counting area for on-line monitoring.

Chapter 5

Calibrations

5.1 Position Calibrations

Position calibrations for the ΔE detectors were done by first forming the quantity:

$$POSX = \frac{X - X_i^0}{\Delta E - \Delta E_i^0} \ , \tag{5.1}$$

where X and ΔE were the raw position and amplitude signals, and X_i^0 and ΔE_i^0 were the d.c. offsets (pedestals). Likewise, for the E detectors,

$$POSY = \frac{Y - Y_i^0}{E - E_i^0} \ . \tag{5.2}$$

Since all the resistance appeared in the gaps between the high conductivity strips, events incident between the midpoint of gap j and the midpoint of gap $j+1$ had, to first order, the same value of POSX or POSY. Typical plots of POSX and POSY for singles events of all data runs summed together are shown in Figure 5.1 for telescope D7. Peaks corresponding to the fifteen strips in the x and y directions are clearly distinguishable. The non-linearity of POSY is most likely due to variations in thickness of the high resistivity gaps. While non-linearities of this sort would be a serious problem for continuous readout detectors, they were perfectly acceptable here, since the individual strips were still resolvable.

Individual gates were set around each position peak, giving 15 x and 15 y position bins for each detector. The position of a bin in centimeters, relative to the detector center, was taken to be the position of the midpoint of its high conductivity strip. Its width was given by the sum of a strip width (2.42 mm) plus a gap width (.607 mm) or ~ 3 mm. Transformation to the lab coordinate system introduced an additional estimated uncertainty of 2 mm from surveying errors, for a final position uncertainty of $\sqrt{1.5^2 + 2^2} = 2.5$ mm, where 1.5 mm is half a bin width.

5.2 ΔE Calibrations

After the completion of data taking, the telescope arrays were removed from their locations and placed on a d.c. driven motor mount inside the scattering chamber which was capable of moving each telescope directly into the path of the beam. Then, low intensity calibration beams of known energy were run directly into the detectors, first with the ΔE's in place and afterwards with the ΔE's removed. Due to time limitations, only a 120 MeV/A ^{86}Kr/^{129}Xe cocktail beam was run into the ΔE detectors, giving just two calibration points. In principle, this type of detector should behave very linearly, however, so two points should be enough. The energy deposited in MeV by the Kr and Xe particles was calculated with the program RANEN [36], and straight lines were drawn through plots of energy vs. channel number, giving a relationship:

$$\Delta E(MeV) = a + b\Delta E_{channel} \ , \tag{5.3}$$

between the deposited energy and the ADC channel. A calibrated plot of ΔE in MeV for the "best" ΔE detector, D7, is shown in Figure 5.2.

The thickness of the ΔE detector for telescope D7 was very uniform across its face; for other ΔE's, however, the situation was not as good. The Kr/Xe ΔE plot

for a more typical detector, D1, is shown in Figure 5.3. The broad widths and ugly shapes of the peaks are due to variations in thickness of the order of 5% from one region of the detector to another. For an incremental change in thickness, δs, relative to some fiducial point where the thickness is s_0, the incremental change in the deposited energy is

$$\frac{\delta \Delta E}{\Delta E_0} = \frac{\delta s}{s_0} \ . \tag{5.4}$$

Since the incident position of a particle was simultaneously measured along with its pulse-height, and the absolute thickness at the center of each detector could be fairly reliably determined from capacitance measurements, it was possible, in principle, to determine the absolute thickness at every location across the faces of the detectors from the calibration data. The relationship between the ADC channel and ΔE energy in MeV could then be modified to read:

$$\Delta E(MeV) = (a + b\Delta E_{channel})\, \delta s \ . \tag{5.5}$$

A plot of the data of Figure 5.3, corrected for thickness variations, is shown in Figure 5.4. The problem was that, unfortunately, the calibration beams were not spread completely over the faces of the detectors. In fact, most detectors had less than 50% of their surfaces covered. An attempt was made to map the uncovered regions using capacitance measurements, but this technique was inherently less precise than the calibration beam method.

When a particle passes through a ΔE detector it loses energy primarily through interactions with the electrons in the solid. The mean energy loss is well described by the familiar Bethe-Bloch equation, but there will always be a distribution about the mean. The theoretical distribution function was worked out by Vavilov [37]. For the range of particle velocities and masses relevant to this experiment, it is essentially Gaussian, with a variance:

$$\sigma^2 = .3071 \frac{Z}{A} \frac{z^2}{2\beta^2} \epsilon_{max} \left(1 - \frac{\beta^2}{2}\right) \Delta x \ , \tag{5.6}$$

where Z and A are the atomic number and atomic mass of the absorbing material (Si in this case), z and β are the charge and velocity of the incident particle, Δx is the thickness of the detector in g/cm^2, and $\epsilon_{max} \approx 2m_e\beta^2\gamma^2$ is the maximum energy that can be transferred to an electron in a single collision. For 120 MeV/A heavy-ions, $\epsilon_{max} \approx 280$ keV. The range of 280 keV electrons in silicon is extremely short, of the order of nanometers, so all of the deposited energy is expected to remain well contained in the detector. For detector D7 (.077 g/cm^2), Equation 5.6 predicts σ's of 3 and 4.5 MeV for Kr and Xe, while Gaussian fits to the two peaks in Figure 5.2 give σ's of 5 and 13 MeV. Other detectors showed comparable deviations from the theoretical limit after thickness corrections. The large discrepancy is not completely understood, but is most likely due to noise inherent in the detectors and associated electronics.

5.3 E Calibrations

After the ΔE calibration runs were done, the ΔE's were removed and cocktail beams of 80 MeV/A ^{28}Si/^{56}Fe and 80 and 120 MeV/A ^{86}Kr/^{129}Xe were run directly into the E detectors. Exact beam kinetic energies were determined from the values of the Bevatron magnetic field and the beam radius at extraction through the relations:

$$p = \frac{Ze}{c}BR$$

$$E = \sqrt{p^2 + M^2} - M \ ,$$

and were found to differ from the whole number values quoted above by less than .5 MeV/A. (Of course, the energy per nucleon of the individual members of a doublet were not precisely the same, owing to binding energy effects, but such differences were less than .1%.) A typical raw ADC spectrum from the 120 MeV/A Kr/Xe run is shown in Figure 5.5. The width of the Xe peak is $\sim$4.5 channels

Ion	ADC channel	E_{true}(MeV)	PHD/ballistic deficit (%)
Si	229	2231	.15
Fe	442	4462	.73
Kr	659	6874	1.8
Kr	957	10280	2.2
Xe	939	10311	4.7
Xe	1372	15419	6.1

Table 5.1: E calibration points for detector D2

FWHM, corresponding to roughly 50 MeV FWHM. The total deposited energy in this case is 15419 MeV, therefore the fractional width of the peak is $\sim$.3%. Since the spread of beam particle energies from the Bevatron is expected to be at least this large, the energy resolution of the E detectors was probably better than .3%.

The linearity of the E detectors is quite a different matter. The energies of the six calibration points and the corresponding ADC channel numbers for detector D2 are given in Table 5.1 and plotted in Figure 5.6, along with the best straight line fit, which has a χ^2 per degree of freedom of around 75. In particular note that, although the 80 MeV/A Xe point (E_{true}=10311 MeV) had a higher total energy value than the 120 MeV/A Kr point (E_{true}=10280 MeV), its ADC channel number was actually lower. All detectors showed this behavior, which was initially thought to be due to the usual pulse height defect.

Pulse height defect is defined as the difference between the pulse heights of a detector in response to an alpha particle and to a heavy-ion of the same total kinetic energy. For semiconductor detectors, such as the E detectors used in this experiment, it is a well-studied phenomenon. The major contributing factors are thought to be [38]: 1) loss of charge carriers through recombination in the dense

plasma column created by the heavily-ionizing particle or at trapping centers; 2) energy lost in non-ionizing collisions with the nuclei of the semiconductor crystal; and 3) energy lost at the incident surface due to the presence of a dead layer. Various empirical formulas have been used to characterize the PHD, generally of the power law form [39]:

$$PHD \propto Z^a E_d^b \ ,$$

where Z is the charge of the incident ion, E_d is its measured energy, and a and b are, in general, functions of Z. The important point is that, for all previous studies of which this author is aware, $b < 1$. This means that the fractional PHD, $\frac{PHD}{E}$, decreases as the incident energy increases. Detailed study of the calibration data for this experiment, which included ions of the same Z at different energies, indicated that the fractional difference between the measured and true energies actually *increased* in going from 80 to 120 MeV/A.

The cause of this behavior is not fully understood, but subsequent tests indicated that, in addition to the normal pulse height deficit, there may have been some ballistic deficit present when the data of this thesis were taken. Ballistic deficit occurs when the time constant of the shaping amplifier is not long enough in comparison to the charge collection time in the detector itself. The charges constituting the energy signal were collected through the incident front surfaces of the E detectors. Since higher energy particles penetrated more deeply into the detector, the charge collection time and, therefore, the ballistic deficit, could have increased with incident energy.

Regardless of the origin of the problem, an empirical formula with which to correct the data was sought. From the calibration data it was clear that the size of the correction depended upon the charge of the incident ion. For the calibration points the charges were known, but for the actual data they could only be determined once the correction was made. Therefore, some iteration was

going to be required. Many different forms were tried; the one that seemed to work best was:

$$E = a + bE_{channel} + c\left[(E+\Delta E)^{1.66} - E^{1.66}\right]^{2/3} E^{1.66} \ , \qquad (5.7)$$

where E and ΔE are the deposited energies in MeV for the E and ΔE detectors, and $E_{channel}$ is the ADC channel number for the E detector. As discussed below in the section on Z calibrations, the quantity in brackets is proportional to Z_{par}, the experimentally determined Z parameter:

$$\begin{aligned} Z_{par} &\propto (E+\Delta E)^{1.66} - E^{1.66} \\ &\propto M^{2/3}Z^2 \ , \end{aligned}$$

and $E^{1.66}$ is roughly proportional to the range, R, of the particle in the E detector:

$$E^{1.66} \propto M^{2/3}Z^2R \ ,$$

where M is the particle mass. The correction term is, therefore, roughly of the form $Z^{4.5}R$.

Since E appears on both sides, it was necessary to iterate Equation 5.7, with good convergence occurring after four iterations. Fits to the six calibration points were made to determine the coefficients a, b, and c for each detector. For some of the detectors the fits were quite good, giving E values differing by less than .5% from the actual values. For other detectors, however, deviations of up to 3% were obtained, especially for the Si and Fe points. In general, there was a strong correlation between the quality of the E fit for a given detector and the ultimate Z resolution for that detector.

5.4 Z Calibrations

The amount of energy deposited by a particle in the E and ΔE detectors can be used to identify it. The method used in this analysis is based on the fact that, in

the energy region of this experiment, the range of a heavy-ion in matter is well represented by the power law form [40]:

$$R = \frac{aM}{Z^2}\left(\frac{E}{M}\right)^b \quad , \tag{5.8}$$

where Z, M, and E are the charge, mass, and kinetic energy of the ion. The usefulness of this equation lies in the fact that, for a given absorbing material, the parameters a and b are nearly independent of ion species. For example, for 50 to 150 MeV/A ions incident on silicon, b varies from 1.66 for ^{86}Kr to 1.60 for ^{129}Xe.

If an ion deposits an energy ΔE in a detector of thickness Δx, then stops in another detector, depositing an energy E, we have from Equation 5.8:

$$\Delta x = \frac{a}{M^{b-1}Z^2}\left[(E+\Delta E)^b - E^b\right] \quad . \tag{5.9}$$

This equation can be rearranged to define a Z parameter:

$$Z_{par} \equiv c\left[(E+\Delta E)^b - E^b\right] \tag{5.10}$$

$$= \frac{c}{a}M^{b-1}Z^2\Delta x \quad , \tag{5.11}$$

where c is a small constant inserted to scale down the right hand side to reasonable values. In principle, Equation 5.11 provides a mean of identifying both the mass and the charge of the particles. In practice, the separation in Z_{par} values between different isotopes of the same Z is too small to be experimentally resolvable, so one is only able to determine the charge. Even the charge identification may not be entirely unambiguous, however, since high mass isotopes of charge Z can have nearly the same value of Z_{par} as low mass isotopes of charge $Z+1$.

A plot of Z_{par} for Monte Carlo generated events of charge 29 through 63 passing through a 300 μm Si detector, with incident energies between 100 to 140 MeV/A, is shown in Figure 5.7. Each species of ion was given a fixed mass in the calculation, corresponding to the expected most probable mass, A_{mp}, for low

excitation energy ^{238}U fission, as extrapolated from measurements of A_{mp} in ^{235}U fission [41]. The energy deposited in the ΔE detector was calculated with the Bethe-Bloch equation and perfect energy resolution was assumed. Fixed values of $b = 1.66$ and $c = 8 \times 10^{-4}$ were used for all events, which causes the small amount of jitter in the spikes. The Monte Carlo was then modified to include: 1) the amount of ΔE broadening seen in the calibration data; 2) a 1% error in the E determination; and 3) a Gaussian A dispersion for each Z, with a width ($\sigma = 1.5$) similar to what is seen in low excitation energy fission [42]. The result is Figure 5.8, which might be what one would expect the actual data to look like.

Unfortunately, the real data do not come close to approaching the resolution of Figure 5.8. Figure 5.9 shows the Z_{par} distribution for singles events of all data runs added together for one of the best detectors, D7, and one of the worst, D1. The reason for the poor resolution is not fully understood. Much effort was spent in checking and rechecking the calibrations and in trying to improve the resolution. In the end, a slight improvement was made by modifying Z_{par} with a small correction factor:

$$Z_{par} \longrightarrow Z_{par} - f\,(Z_{par})\,\Delta E \ , \tag{5.12}$$

where the function, $f\,(Z_{par})$, was determined from a combination of calibration data and Monte Carlo. The data of Figure 5.9 include this correction.

In the Z_{par} plot for the detector with the best resolution, D7, distinguishable peaks for Z's up to 50 ($Z_{par} \sim 700$) are clearly visible. Beyond that, the resolution deteriorates rapidly and it would seem hopeless to try to determine where events of a particular Z fall. With the aid of a Monte Carlo calculation, however, one can determine where they *should* fall and, with a little effort, one can see structures in the distribution all the way out to around $Z = 52$. The resolution for the other detectors was not as good, but the distinguishable structures which do show up

invariably appear where calculations say a peak should be.

The procedure adopted for the Z calibrations, therefore, was to rely entirely on the Monte Carlo. The Z_{par} values for the various ion species were calculated as in Figure 5.7, only using slightly different masses (see Section 6.1.5), and bins extending between the midpoints of the peaks were defined. In the data analysis, all the events within a given bin were assigned the same Z value. Of course, many fragments were misidentified in this manner since neighboring Z's clearly overlap. A subsequent stage of the analysis sought to address the problem of Z misidentification and correct for it (see Section 6.2).

5.5 Mask Calibrations

As pointed out in Section 4.7, the plastic scintillator counter used to measure the beam flux was covered with a Pb mask during data taking in order to attenuate the amount of beam hitting it to countable levels. The mask transmission fraction was determined in separate calibration runs by comparing the number of counts registered by the scintillator with and without the mask to an independent measurement of the beam intensity. This independent measurement was provided by a Secondary Emission Monitor (SEM) located just at the exit of the Bevatron, at a point called F1, which is the first focal point for particles entering the external beam line. The SEM is maintained and operated by the people of the BEVALAC facility and is basically a stack of several .25 mil thick, Al sheets. As the beam particles traverse it, charge is built up on the Al and read out through a calibrated current integrator. The SEM reading, in terms of particles/spill, can be displayed on a TV monitor in the experimenters' area and is supposed to be an indicator of the beam intensity. The beam intensity it measures is not the intensity on target, however, since a substantial fraction can get lost in the 50 meters or so between

F1 and the target.

The mask calibration runs were done with the beam intensity lowered by an order of magnitude from its level during data taking. First, with the mask on and the blank target in position, a short run was made, during which the number of scintillator counts for each spill and the corresponding SEM reading were recorded. Mask-on runs with various levels of beam intensities and with real targets in position were also made. Then, similar runs were made with the mask removed. For each run an average ratio of scintillator to SEM, $\langle SC/SEM \rangle$, was formed. Assuming that the fraction of beam lost between F1 and the scintillator remained constant in time, the ratio:

$$T = \frac{\left\langle \frac{SC}{SEM} \right\rangle_{\text{on}}}{\left\langle \frac{SC}{SEM} \right\rangle_{\text{off}}} , \tag{5.13}$$

should give the mask transmission factor independent of the absolute calibration of the SEM. As it turned out, however, different pairs of mask-on/mask-off runs resulted in T values which differed by as much as 20%. Moreover, the mask was removed and then put back on between the Be-Ag data runs and the U data runs, necessitating a completely separate mask calibration for the uranium target data. Therefore, although the relative normalization of the light target data should be good, the relative normalization of the U data to the light target data could be in error by as much as 40%. With an estimated 20% error, the mask transmission factors were determined to be:

$$T = \begin{cases} .084 \pm .017 & \text{Be, Al, Cu, Ag} \\ .121 \pm .024 & \text{U} \end{cases} .$$

Chapter 6

Data Analysis

6.1 Raw Data

6.1.1 Selection of Binary Events

The first step of the analysis was to select those events in which at least two of the six properly functioning downstream telescopes had ΔE and E ADC signals above a low threshold. The raw ADC signals were then converted to MeV, Z_{par} values were calculated, and Z values were assigned to each fragment. If one of the Z values was determined to be less than the punch-through limit of 29, that event was discarded unless there were more than two hits, in which case the remaining hits were analyzed. Events with three or more hits were a very small fraction of the data ($< .5\%$), since the hardware thresholds of the detectors were set high, and were determined to consist mostly of accidental background.

Aside from the Z values of the fragments, the other important quantities were their velocity vectors, which were needed for efficiency corrections. The magnitudes of the velocities could be calculated from the incident kinetic energies,

$E_i^{kin} = E_i + \Delta E_i$, and the relation:

$$\beta_i = \left[1 - \left(\frac{M_i}{E_i^{kin} + M_i}\right)^2\right]^{1/2} , \tag{6.1}$$

if the masses, M_i, were known. In the first pass through the data, the most probable mass for a given Z, A_{mp}, as determined from studies on low excitation energy uranium fission [41], was used. As described below, these masses resulted in velocities which were deemed too low by about 2%, so slightly different masses were used in the final analysis. To obtain the $\vec{\beta}_i$ from the β_i, the position signals of the fragments were converted into x and y coordinates relative to the centers of the detector faces, then transformed to lab x, y, and z coordinates. A polar coordinate system with z along the beam axis was defined and emission angles, θ_i and ϕ_i, were calculated by assuming that all fragments originated from the center of the target. Velocity components were then calculated with the usual formulae, $\beta_i^x = \beta_i \sin\theta_i \cos\phi_i$, etc.

The individual velocity vectors were turned into a velocity for the emitting source through the relation:

$$\vec{\beta}_s = \frac{\vec{P}_s}{[P_s^2 + M_s^2]^{1/2}} , \tag{6.2}$$

where

$$\begin{aligned} \vec{P}_s &\equiv \vec{p_1} + \vec{p_2} \\ &= M_1\vec{\beta}_1\gamma_1 + M_2\vec{\beta}_2\gamma_2 \\ M_s &\equiv M_1 + M_2 \ . \end{aligned}$$

6.1.2 Discovery of a Low Z Contaminant in the U Target

The source velocities were decomposed into a component along the beam direction, $\beta_{||}$, and a transverse component, $\beta_\perp$. Plots of the transverse component, gated

on Z_{tot} ($\equiv Z_1 + Z_2$) = 92, for the five targets, are shown in Figure 6.1. As the target atomic number increases from Be to Ag, the $\beta_\perp$ distributions shift outward. This behavior is easily explained as being due to the increasing Coulomb kick the projectile receives from the target in these very peripheral collisions. The arrows in the plots are the transverse velocities one would expect at impact parameters:

$$b = 1.2\left(A_{proj}^{1/3} + A_{targ}^{1/3}\right) \ ,$$

assuming the beam particles followed classical Rutherford trajectories.

For the U target, however, there are two distinct components in the $\beta_\perp$ distribution, one of which fits the pattern nicely, while the other is very suggestive of a low Z contaminant. Subsequently, two pieces of confirming evidence that such a contaminant was present were discovered. The first came from the Z distributions for $Z_{tot} = 92$ events which, as demonstrated below in Section 6.1.3, are a very distinctive indicator of the target atomic number. The Z distribution for the events with $\beta_\perp > .005$ agrees nicely with one's expectations for what the Z distribution for a U target should look like, based on extrapolations from the lighter targets. The Z distribution for events with $\beta_\perp < .005$, on the other hand, looks just like the Z distribution for a low Z target. The second piece of evidence came from an analysis of the 4-fold events. When the requirement that two of the four PPAC's recorded valid hits was imposed, $\sim$360 out of a total of 14,500 coincident events for the U target survived — all of which had $\beta_\perp > .005$. Since the interaction of a beam particle with a low Z contaminant could not have led to a 4-fold event, the evidence seemed to be conclusive that the events with $\beta_\perp < .005$ occurred from interactions with a contaminant. Since the U target was prepared by evaporating uranium onto an aluminum backing, the obvious candidate was Al.

Fortunately, the two $\beta_\perp$ peaks are well enough separated that the events arising from interactions with U could be almost completely recovered by simply placing

a cut at $\beta_\perp \geq .005$. The U target cross sections could still be calculated if the assumption was made that there were actually 1.33 mg/cm^2 of ^{nat}U present in the target and that the contaminant was introduced after the uranium was weighed.

Calculations based on the Al target data indicated that, if indeed Al was the contaminant and the mask transmission factors were determined correctly, a surface layer $\sim .3$ μm thick (.09 mg/cm^2) would have been sufficient to account for the observed number of low $\beta_\perp$ events. The U target itself would have been .7 μm thick, if 1.33 mg/cm^2 were present. In the remainder of this thesis, data presented for the U target have a cut placed at $\beta_\perp \geq .005$, unless explicitly stated otherwise.

6.1.3 $Z_1 + Z_2$ Distributions

Raw $Z_1 + Z_2$ distributions, uncorrected for charge misidentification, are plotted in Figure 6.2. All the distributions peak at 92, with the sharpness of the peak tending to increase with Z_{targ}. In the geometrical model presented in the Appendix, the ratio of the number of events with $Z_{tot} = 92$ to the number with $Z_{tot} = 91$, neglecting efficiency corrections and Z misidentification problems, can be crudely estimated as follows:

$$\begin{aligned}
\frac{N_{92}}{N_{91}} &\approx \frac{\sigma_{92}}{\sigma_{91}} \\
&\approx \frac{2\pi\left(\rho_{min} - a\right)\Delta\rho}{2\pi\left(\rho_{min} - \Delta\rho - a\right)\Delta\rho} \\
&= \frac{\rho_{min} - a}{\rho_{min} - \Delta\rho - a} \\
&\approx 1 + \frac{\Delta\rho}{\rho_{min} - a}\,.
\end{aligned}$$

Since $\rho_{min} - a$ increases with target atomic number, this simple picture predicts that, in the absence of electromagnetic dissociation, the sharpness of the peak at $Z_{tot} = 92$ should decrease with increasing Z_{targ}. The fact that the opposite behav-

ior is observed is qualitative evidence for the importance of an electromagnetic component in the cross sections. Quantitative calculations using the geometrical model are given in Chapter 7.

6.1.4 Z Distributions

Plots of the Z distributions for all coincidence events are shown in Figure 6.3. The sharp edge at $Z = 29$ is due to the cutoff imposed to avoid punch-through problems. Imposing the requirement that the sum of the charges of the two fragments be 92, gives the Z distributions of Figure 6.4, which become increasingly asymmetric as the target atomic number increases. The actual yields for all targets were more asymmetric than in Figure 6.4 since the geometrical efficiency of the detector system was biased toward symmetric splits (see Section 6.3).

As is well known from studies of light-particle induced fission, the magnitude of the asymmetric component in the fragment yields is a sensitive function of the amount of excitation energy imparted to the fissioning system [42]. Higher excitation energies lead to increased yields of the symmetric component in ^{238}U fission. Since the excitation energy associated with virtual photon absorption in this experiment was rather modest (< 20 MeV), the increasing asymmetries of Figure 6.4 are striking evidence for the onset of electromagnetic dissociation.

The spike at $Z = 46$ in the U data is a consequence of the fact that, for 46-46 splits, the bin of the histogram corresponding to $Z = 46$ gets incremented twice. In fact, there should be a spike at $Z = 46$ in all of the $Z_{tot} = 92$ distributions, and the fact that there isn't is an indication of the problems with the Z resolution. This is demonstrated in Figure 6.5, where the $Z = 46$ bins of Figure 6.4 have been divided by 2 to give distributions which should look more like the A distributions one normally sees plotted for fission fragment yields. Clearly, there is a problem

with the Be–Ag plots, although the U data look reasonable.

Also interesting are the Z distributions for $Z_{tot} = 91$ and 93 (Figures 6.6 and 6.7). Most of the asymmetry is gone from the 91's, although the Ag and U data are noticeably flatter. Since the true 91's are expected to arise entirely from nuclear processes, the small asymmetry in the $Z_{tot} = 91$ events for these targets is most likely due to misidentification of $Z_{tot} = 92$ events. This is more apparent in the $Z_{tot} = 93$ events, a substantial fraction of which can probably be attributed to Z misidentification.

6.1.5 Source Velocities

The extraction of source velocities from the data was described above in Section 6.1.1, where it was mentioned that using masses taken from data on low excitation energy fission resulted in source velocities that appeared too low. In the source velocities constructed from these masses, a distinction was made between M_i^{pre}, the initial mass of a fragment before neutron evaporation and M_i^{post}, the mass after evaporation. The individual fragment velocities were calculated using M^{post} (compare Equation 6.1):

$$\beta_i = \left[1 - \left(\frac{M_i^{post}}{E_i^{kin} + M_i^{post}}\right)^2\right]^{1/2} , \tag{6.3}$$

while the source momentum and mass were calculated using M^{pre}:

$$\begin{aligned} \vec{P}_s &= M_1^{pre}\vec{\beta}_1\gamma_1 + M_2^{pre}\vec{\beta}_2\gamma_2 \\ M_s &= M_1^{pre} + M_2^{pre} \ . \end{aligned}$$

For $Z_{tot} = 92$ events, M_s is always 238×931.5 with this definition. The parallel and perpendicular source velocity distributions constructed with this method, gated on $Z_{tot} = 92$, are shown in Figures 6.8 and 6.9. The low Z contaminant has been included in the $\beta_\perp$ plot for the U data but removed from the $\beta_{||}$ plot.

The arrows in the $\beta_{||}$ plots indicate the calculated beam velocity, $\beta_{beam} = .464$. For electromagnetic events the parallel velocity of the ^{238}U nucleus should have been essentially unchanged, while the minimum $\beta_{||}$ from a collision with a single stationary nucleon in the target is $\sim .460$. The distributions of Figure 6.8, on the other hand, all peak below .456. This behavior could be due to a systematic problem with the E calibrations, but the use of cold fission masses for the low Z targets, where higher excitation energy processes predominated, could have also contributed. In the final analysis a different set of masses was used and the distinction between M^{pre} and M^{post} was dropped. The new masses were, on average, 4.5 neutrons lighter than the M^{post} masses, with more neutrons removed from the lower Z ions and fewer from the high Z ions. The $\beta_{||}$ distributions extracted with the lighter masses are shown in Figure 6.10; the $\beta_{\perp}$ distributions are shown in Figure 6.1. The peaks and widths obtained from Gaussian fits to the parallel velocities of Figure 6.10, along with the peaks and widths of the $Z_{tot} = 91$ parallel velocities, which look similar to the $Z_{tot} = 92$'s, only slightly downshifted, are given in Table 6.1.

target	$\langle \beta_{||}^{92} \rangle$	$\langle \beta_{||}^{91} \rangle$
Be	.4599(.0047)	.4581(.0054)
Al	.4594(.0047)	.4576(.0054)
Cu	.4605(.0046)	.4584(.0053)
Ag	.4613(.0046)	.4586(.0053)
U	.4621(.0041)	.4592(.0052)

Table 6.1: Parallel source velocities.

The importance of the source velocities for the analysis was in the acceptance corrections. In Section 6.3, it is shown that the acceptance correction depends

primarily on $\beta_\perp$ and that the $\beta_{||}$ dependence is negligible. Comparing Figures 6.1 and 6.9, one sees that $\beta_\perp$ is relatively unaffected by the choice of masses.

6.2 Unfolding Correction

To estimate the effect of fragment Z misidentification, a simple unfolding procedure was devised. Let R_j be the true number of fragments of charge j in the singles distribution, and let D_j be the detected number. Then, since Z is a discrete variable, the relation of the detected number to the true number can be expressed as

$$D_i = f_{ij} R_j \ , \tag{6.4}$$

where repeated indices are summed over. Likewise, for the coincidence distribution, let R_{ij} be the true number of events with $Z_1 = i$ and $Z_2 = j$, and let D_{ij} be the corresponding detected number. Assuming the errors in the determination of Z_1 and Z_2 are statistically independent, we have

$$D_{ij} = f_{ik} f_{jl} R_{kl} \tag{6.5}$$

or, in matrix form:

$$\mathbf{D} = \mathbf{f R f^T} \ . \tag{6.6}$$

Using the fact that $(\mathbf{f^T})^{-1} = (\mathbf{f^{-1}})^{\mathbf{T}}$, Equation 6.6 can be inverted to give

$$\mathbf{R} = \mathbf{f^{-1} D (f^{-1})^T} \ . \tag{6.7}$$

Of course, to invert $\mathbf{f}$, one needs to know what it is first. Since there is no *a priori* knowledge of what $\mathbf{f}$ is, the best that can be done is an educated guess. Moreover, even if the true $\mathbf{f}$ was known, the true $\mathbf{R}$ does not necessarily follow from Equation 6.7 because of statistical fluctuations. From Equation 6.7, the statistical

error in the determination of R_{ij} is

$$\sigma^2_{R_{ij}} = \sum_{kl} \left(f^{-1}_{ik}\right)^2 \left(f^{-1}_{jl}\right)^2 \sigma^2_{D_{kl}} \quad . \tag{6.8}$$

The sum insures that

$$\frac{\sigma_{R_{ij}}}{R_{ij}} \geq \frac{\sigma_{D_{ij}}}{D_{ij}} \quad .$$

For the lack of a reason to choose anything else, the assumption was made that f_{ij} is Gaussian:

$$f_{ij} = \frac{1}{\sqrt{2\pi}\sigma_j} \int_{Z_i-.5}^{Z_i+.5} dZ_i e^{-(Z_i-Z_j)^2/2\sigma_j^2} \quad . \tag{6.9}$$

With this form, **f** is a well-behaved, positive definite matrix and Equation 6.6 was easily inverted with available computer library routines. The real question was what to take for the σ_j's. Since there was a direct relation between a fragment's Z value and its Z_{par} value, the observed smearing in the Z_{par} distribution (see Figure 5.9) was used as a guide. First, Monte Carlo events with Z_{par} values corresponding to the centers of the Z_{par} bins used in the data analysis were generated (top of Figure 6.11). Then, a set of σ_j^{Zpar}'s was chosen and the Monte Carlo events were given Gaussian smearings with these σ_j^{Zpar}'s. The results of one particular choice are shown in the bottom plot of Figure 6.11. The σ_j's associated with the Z distributions were then constructed from the σ_j^{Zpar}'s through the relation:

$$\sigma_j = \frac{\partial Z}{\partial Z_{par}} \sigma_j^{Zpar} \quad , \tag{6.10}$$

and a quadratic fit relating Z and Z_{par}. The matrix **f** was then constructed and inverted, and Equation 6.7 was used to construct **R**.

The σ_j's associated with the σ_j^{Zpar}'s of Figure 6.11 had an average value of $\sim .45$ Z units, implying that around 37% of the fragments were misidentified by one Z unit. The $Z_1 + Z_2$ distributions which resulted from unfolding with this set are shown in Figure 6.12. This figure should be compared with Figure 6.2, which

	92's		91's		93's	
	detected	unfolded	detected	unfolded	detected	unfolded
Be	4212(65)	5179(91)	4125(64)	4166(91)	1855(43)	1436(62)
Al	3260(57)	4145(80)	2798(53)	2639(75)	1556(39)	1259(57)
Cu	2541(50)	3271(71)	2184(47)	2051(66)	1135(34)	862(48)
Ag	2686(52)	3541(72)	2203(47)	1941(67)	1175(34)	848(49)
U	1812(43)	2361(60)	1396(37)	1229(53)	907(30)	764(43)

Table 6.2: Coincidence events for $Z_{tot} = 92$, 91, and 93 before and after unfolding.

shows the same distributions before unfolding. Table 6.2 contains the detected and unfolded number of $Z_{tot} = 92$, 91, and 93 events. From the figure and the table one sees that the effect of the unfolding has been to increase the number of $Z_{tot} = 92$'s by twenty to thirty percent and decrease the $Z_{tot} = 93$'s by a comparable fraction. The $Z_{tot} = 91$'s were less affected, having been slightly increased for Be and decreased for the rest.

Many other sets of σ_j's were tried. The general trend seemed to be that larger σ_j's led to greater increases in the 92's and decreases in the 93's, with the 91's being relatively unaffected. The sum of the 92's, 91's, and 93's for a given target, however, was observed to be relatively insensitive to the unfolding correction. From Equation 6.5, the spillover of the true 92's into other bins could be estimated. If the **f** used to calculate the values of Table 6.2 is realistic, then $\sim$61% of the true 92's were correctly identified, while slightly more than 36% were incorrectly identified as 91's or 93's, and less than 3% were misidentified by more than one charge unit. Results from unfolding with the largest set of σ_j's within reason implied that a maximum of 6% of the 92's were misidentified by more than one charge unit. This fact, along with the insensitivity of the sum of 91's, 92's, and 93's to the unfolding, is exploited in the extraction of electromagnetic

dissociation cross sections in Chapter 7.

The effect of the unfolding on the Z distributions is shown in Figures 6.13 through 6.15, which should be compared to Figures 6.4 through 6.7. The shape of the 92's has not been substantially altered, but the 91's and 93's look distinctly unnatural. Monte Carlo studies showed that, even if one knows the matrix $\mathbf{f}$ exactly, the unfolded shapes can come out looking unnatural due to statistical fluctuations. The *integrals* of the unfolded distributions, on the other hand, always gave the true answer to within statistical errors.

Of course, for the real data the exact $\mathbf{f}$ was not known. The fact that the Monte Carlo Z_{par} plot of Figure 6.11 looks similar to the real data can only be used to argue that the measured number of $Z_{tot} = 92$'s could easily be too low by 30% or more.

6.3 Efficiency Corrections

The coincidence efficiencies of the detector system for projectile fragments were calculated by Monte Carlo. For a general value of Z_{tot} this would have been a highly complicated matter, but for the most peripheral events, *i.e.* those leading to Z_{tot}'s of 91, 92, and 93, the process could be modeled as binary fission from a moving source. Initially, events were generated with several different values of the parallel source velocity. However, the calculated efficiencies were found to be very insensitive to this quantity over the range of measured values (see Figure 6.16), so in the final calculations the parallel source velocity was fixed at the beam velocity.

For the $Z_{tot} = 92$'s, 100,000 Monte Carlo events for each Z_1-Z_2 split between 29-63 and 46-46, at 16 discrete values of $\beta_\perp$ between 0 and .015, were generated. The efficiencies at points between these values of $\beta_\perp$ were determined by interpolation. The fragments were assumed to be emitted isotropically in the projectile rest

frame with kinetic energies (which are known to be very insensitive to the excitation energy of the source [42]) taken from measurements on proton-induced ^{238}U fission [43]. A Lorentz boost was then made to the lab frame and the fragments were allowed to follow straight-line trajectories until they either struck the active area of one of the detectors or passed by undetected. The results for all splits at $\beta_\perp = 0$ and for selected splits as a function of $\beta_\perp$ are shown in Figures 6.17 and 6.18. The bias toward symmetric events at low values of $\beta_\perp$ is mostly due to the loss of heavy fragments down the beam pipe. As $\beta_\perp$ increases, the heavy fragments are more likely to get enough sideways movement to hit a detector but light fragments are more likely to get emitted at too large angles. The net result is that the efficiencies become nearly independent of the split.

For $Z_{tot} = 91$ and 93, two ways of calculating the efficiency were tried. For the 91's, the first method was to use the previously calculated efficiencies for the 92's and assume that a proton was lost from one of the fragments after scission. The efficiency was then taken to be the average of the efficiencies for the two possible initial configurations. For example, for 45-46 splits, the efficiency was taken to be the average of 45-47 and 46-46 splits. Likewise, for the 93's the efficiency for a Z_1=i, Z_2=j split was calculated from the average of (i-1,j) and (i,j-1) splits. In the second method, the kinetic energies of the two fragments were calculated from the Coulomb repulsion of two touching spheres with total charge 91(93) and total mass 236(238), the radii of the two spheres being given by $R = 1.83A^{1/3}$ [44]. The results from the two methods (Figures 6.19 and 6.20) were found to differ only slightly, so only the first method was used in the final calculations.

The effect of the efficiency corrections on the Z distributions is shown in Figures 6.21 through 6.23. Comparing Figure 6.21 to Figure 6.4, one sees that the distributions for the $Z_{tot} = 92$'s have become more asymmetric, though the effect for the U target data is small because of the large transverse velocity. The

$Z_{tot} = 91$'s have also flattened out and become slightly more asymmetric and the $Z_{tot} = 93$'s still look like they could be mostly misidentified 92's.

As mentioned above in Section 6.1.4, the asymmetry of the fragment yields is a sensitive indication of the amount of excitation energy present in the fissioning source. Quantitative estimates of the mean excitation energies are complicated in this case by the Z resolution problems, but loose limits can be derived. From a rough comparison of Figures 6.21 and 6.22 to experimental data on ^{238}U fission fragment yields vs. excitation energy [45], the conclusion is that $\langle E^* \rangle \geq 50$ MeV for the $Z_{tot} = 91$ events of all targets and the $Z_{tot} = 92$ events of beryllium. For the uranium $Z_{tot} = 92$'s, on the other hand, the comparison gives $\langle E^* \rangle \leq 36$ MeV.

Chapter 7

Results

7.1 Total Cross Sections

Once the efficiencies were determined, the total fission cross sections in mb for $Z_{tot} = 92$ events were calculated from the relation:

$$\sigma_{92}^{tot} = \sum_{i,j=92-i} \frac{n_{ij} \cdot T \cdot A}{\epsilon_{ij} \cdot SC \cdot \Delta x \cdot N_A} \cdot 10^{30} \quad , \tag{7.1}$$

where

n_{ij} = number of detected (or unfolded) i,j events as a function of $\beta_\perp$,
ϵ_{ij} = coincidence efficiency as a function of $\beta_\perp$,
T = mask transmission factor,
A = atomic weight of the target,
Δx = effective thickness of the target in mg/cm^2,
SC = measured number of counts on the beam scintillator paddle gated by $\overline{\text{BUSY}}$,
N_A = Avogadro's number,

with similar expressions for the $Z_{tot} = 91$ and $Z_{tot} = 93$ cross sections. For the U target, which was rotated, the effective thickness was different from the actual thickness by a factor of $1/\cos 40°$. Assuming the uncertainties in the efficiency

calculations are negligible compared to other uncertainties, the errors in the cross sections are composed of two parts, a statistical error:

$$(\Delta\sigma)_{stat} = \frac{\sigma}{\sqrt{N}} \ , \tag{7.2}$$

where N is the total number of detected events for the given Z_{tot}, and a systematic error associated with the flux measurement:

$$(\Delta\sigma)_{norm} = \sigma\frac{\Delta T}{T} \ . \tag{7.3}$$

Total cross sections calculated for data with no unfolding correction and for data unfolded with two different sets of σ_j's are given in Tables 7.1–7.3 and plotted in Figure 7.1. The circles in the figure were calculated from data in which no unfolding correction had been applied, the squares from data unfolded with the set of σ_j's of Section 6.2, and the triangles from data unfolded with a somewhat larger set of σ_j's. The error bars in the figure reflect statistical uncertainties only. The errors associated with the flux normalization problems are given in the third entry of each column of the tables. All errors are 1σ. Although there is a 20% uncertainty in the absolute normalization of the Be-Ag data, the relative normalization of these points should be good. Recall from Section 5.5, however, that the Pb mask covering the beam counter was moved between the measurement with the Ag target and the measurement with the U target. Consequently, in addition to the uncertainty in the absolute normalization of the U data, there is an uncertainty in its relative normalization to the other points.

From Figure 7.1, it is clear that the magnitude of the cross sections for the individual Z_{tot}'s is highly sensitive to the unfolding correction. As pointed out in Section 6.2, however, the sum of the 91's, 92's, and 93's is relatively insensitive to the unfolding. This is demonstrated in Figure 7.2 and Table 7.4 where the sum cross sections are given. Since it is extremely improbable, at the beam energy of

this experiment, that the projectile can absorb a virtual photon of sufficient energy to emit a proton *and* retain enough excitation energy to undergo fission, the true Z_{tot} should be 92 for the EMD events. Owing to the imperfect charge resolution, many of these events were incorrectly identified, but the fraction misidentified by more than one Z_{tot} unit is estimated to be $< 6\%$. Consequently, the sum cross sections of Table 7.4 should contain almost all of the EMD events.

	σ_{92}^{tot}	σ_{91}^{tot}	σ_{93}^{tot}
Be	$197 \pm 3 \pm 39$	$199 \pm 3 \pm 40$	$86 \pm .4 \pm 17$
Al	$263 \pm 5 \pm 52$	$233 \pm 5 \pm 47$	$126 \pm .6 \pm 25$
Cu	$371 \pm 8 \pm 74$	$319 \pm 7 \pm 64$	$166 \pm 1 \pm 33$
Ag	$471 \pm 9 \pm 94$	$381 \pm 8 \pm 76$	$205 \pm 1 \pm 41$
U	$579 \pm 14 \pm 116$	$446 \pm 2 \pm 89$	$290 \pm 10 \pm 58$

Table 7.1: Total fission cross sections in mb, no unfolding correction.

	σ_{92}^{tot}	σ_{91}^{tot}	σ_{93}^{tot}
Be	$240 \pm 4 \pm 48$	$203 \pm 5 \pm 41$	$67 \pm 3 \pm 13$
Al	$331 \pm 7 \pm 66$	$222 \pm 7 \pm 44$	$103 \pm 5 \pm 21$
Cu	$478 \pm 11 \pm 95$	$297 \pm 10 \pm 59$	$126 \pm 7 \pm 25$
Ag	$623 \pm 13 \pm 124$	$332 \pm 12 \pm 66$	$148 \pm 9 \pm 30$
U	$755 \pm 19 \pm 151$	$392 \pm 17 \pm 78$	$245 \pm 14 \pm 49$

Table 7.2: Total fission cross sections in mb with unfolding correction using the set of σ_j's of Section 6.2.

	σ_{92}^{tot}	σ_{91}^{tot}	σ_{93}^{tot}
Be	$280 \pm 7 \pm 56$	$192 \pm 7 \pm 38$	$44 \pm 5 \pm 9$
Al	$397 \pm 10 \pm 79$	$191 \pm 10 \pm 38$	$69 \pm 8 \pm 14$
Cu	$581 \pm 16 \pm 116$	$248 \pm 16 \pm 50$	$74 \pm 11 \pm 15$
Ag	$776 \pm 20 \pm 155$	$240 \pm 18 \pm 48$	$71 \pm 13 \pm 14$
U	$924 \pm 30 \pm 185$	$293 \pm 26 \pm 59$	$173 \pm 22 \pm 35$

Table 7.3: Total fission cross sections in mb with unfolding correction using a somewhat larger set of σ_j's.

	σ_{Σ}^{tot}	σ_{Σ}^{tot}	σ_{Σ}^{tot}
Be	$482 \pm 5 \pm 96$	$510 \pm 7 \pm 102$	$516 \pm 11 \pm 103$
Al	$621 \pm 7 \pm 124$	$655 \pm 10 \pm 131$	$657 \pm 16 \pm 131$
Cu	$855 \pm 10 \pm 171$	$902 \pm 16 \pm 181$	$902 \pm 25 \pm 180$
Ag	$1057 \pm 12 \pm 211$	$1103 \pm 19 \pm 220$	$1088 \pm 30 \pm 217$
U	$1316 \pm 17 \pm 263$	$1392 \pm 29 \pm 279$	$1390 \pm 45 \pm 278$

Table 7.4: Total fission cross sections in mb for the sum of 91's, 92's, and 93's. The three columns contain no unfolding, unfolding as in Table 7.2, and unfolding as in Table 7.3, respectively.

7.2 Extraction of EMD Cross Sections

Two different approaches were used to extract the electromagnetic fission cross sections. Both approaches used the Be data as a non-EMD reference point for estimating the magnitudes of the nuclear contributions to the total cross sections. In the first method, the concept of factorization was used in an attempt to determine σ_{NUC} empirically from the data. The results of this approach were found to be very sensitive to the Z misidentification problems. The second method relied on the geometrical model of the Appendix to estimate the nuclear contribution, and got around the Z misidentification problems by using the sum cross sections of Table 7.4. Unfortunately, neither method was able to avoid the normalization problems associated with the mask transmission factors.

Recall from Equation 3.1 that, according to factorization, $\sigma_{\rm NUC}$ is given by

$$\sigma_{\rm NUC} = \gamma_P^F \gamma_{PT} \ . \tag{7.4}$$

In order to determine the factors γ_P^F and γ_{PT}, data in which there are no EMD events must be used. For this experiment, essentially all of the Be target data and the true $Z_{tot} = 91$'s for all targets should be purely nuclear. Therefore, assuming factorization is valid, the following relations can be written down:

$$\sigma_{92}^{Be} = \gamma_P^{92} \gamma_{P,Be} \ , \tag{7.5}$$

$$\sigma_{91}^{Be} = \gamma_P^{91} \gamma_{P,Be} \ , \tag{7.6}$$

$$\sigma_{92,nuc}^{X} = \gamma_P^{92} \gamma_{P,\dot{X}} \ , \tag{7.7}$$

$$\sigma_{91}^{X} = \gamma_P^{91} \gamma_{P,X} \ , \tag{7.8}$$

where X = Al, Cu, Ag, or U. These equations can be solved for $\sigma_{92,nuc}^{X}$:

$$\sigma_{92,nuc}^{X} = \sigma_{91}^{X} \frac{\sigma_{92}^{Be}}{\sigma_{91}^{Be}} \ . \tag{7.9}$$

The EMD cross sections can then be obtained by subtraction:

$$\sigma_{\rm EMD}^{X} = \sigma_{92}^{X} - \sigma_{92,nuc}^{X} \ . \tag{7.10}$$

The statistical uncertainty in $\sigma_{92,nuc}^{X}$ with this method is given by

$$\left(\frac{\Delta\sigma_{92,nuc}^{X}}{\sigma_{92,nuc}^{X}} \right)_{stat}^2 = \left(\frac{\Delta\sigma_{91}^{X}}{\sigma_{91}^{X}} \right)_{stat}^2 + \left(\frac{\Delta\sigma_{92}^{Be}}{\sigma_{92}^{Be}} \right)_{stat}^2 + \left(\frac{\Delta\sigma_{91}^{Be}}{\sigma_{91}^{Be}} \right)_{stat}^2 \ , \tag{7.11}$$

and the statistical error in $\sigma_{\rm EMD}^{X}$ by

$$\left(\Delta\sigma_{\rm EMD}^{X} \right)_{stat}^2 = \left(\Delta\sigma_{92}^{X} \right)_{stat}^2 + \left(\Delta\sigma_{92,nuc}^{X} \right)_{stat}^2 \ . \tag{7.12}$$

The systematic error associated with $\sigma_{92,nuc}^{X}$, on the other hand, is given by

$$\left(\Delta\sigma_{92,nuc}^{X} \right)_{norm} = \sigma_{92,nuc}^{X} \left(\frac{\Delta\sigma_{91}^{X}}{\sigma_{91}^{X}} \right)_{norm} \ , \tag{7.13}$$

	no unfolding σ_{EMD}	unfolding #1 σ_{EMD}	unfolding #2 σ_{EMD}
Al	$33 \pm 8 \pm 7$	$68 \pm 12 \pm 14$	$117 \pm 22 \pm 24$
Cu	$56 \pm 12 \pm 11$	$127 \pm 18 \pm 25$	$220 \pm 31 \pm 44$
Ag	$94 \pm 14 \pm 19$	$230 \pm 21 \pm 46$	$425 \pm 36 \pm 85$
U	$138 \pm 16 \pm 28$	$293 \pm 30 \pm 59$	$498 \pm 50 \pm 100$

Table 7.5: EMD cross sections in mb extracted with the first method described in the text. The first set of errors are statistical, the second set are systematic.

since the absolute normalizations of σ_{92}^{Be} and σ_{91}^{Be} are the same. The normalization error in $\sigma_{\rm EMD}^{X}$ is given by subtraction:

$$\left(\Delta\sigma_{\rm EMD}^{X}\right)_{norm} = \left(\Delta\sigma_{92,tot}^{X}\right)_{norm} - \left(\Delta\sigma_{92,nuc}^{X}\right)_{norm} \quad . \tag{7.14}$$

This normalization error is of the same order of magnitude as the normalization error in the total cross sections, $\sim 20\%$. The systematic errors in the Al, Cu, and Ag data have the effect of shifting these points in the same direction, by the same percentage, simultaneously. For the U data, however, the normalization uncertainty is completely independent of the other points.

The EMD cross sections extracted with this method are given in Table 7.5 and plotted in Figure 7.3. The symbols in the figure have the same meaning as the symbols of Figures 7.1 and 7.2, and the curves are the theoretical predictions of Figure 2.4. The plotted error bars for the light targets reflect the statistical uncertainties only, while the error bar for the U point was obtained by adding, in quadrature, the statistical and normalization errors. As is evident from the plot, the results are very sensitive to the unfolding, since the ratio of 92's to 91's depends very strongly on this correction. Consequently, although this first method is appealing in principle, the Z resolution problems make its practical application

to this data set unreliable.

Since the sum cross sections of Table 7.4 are relatively insensitive to the unfolding correction and, since essentially all of the electromagnetic dissociation events are expected to be in the $Z_{tot} = 91$, 92, and 93 bins, a better approach was to use the sum cross sections. The nuclear contributions to these cross sections could have been estimated through factorization by, for example, using the $Z_{tot} = 90$ events to determine the projectile-target factors, γ_{PT}. However, the lower statistics of these events, along with the difficulties of doing proper acceptance corrections, would have introduced large uncertainties in the results. Therefore, it was decided that the geometrical model of the Appendix would be just as reliable and easier to implement. First, Equation A.2, with the recoil correction, Equation A.5, was used to determine the parameter Δb from the Be data. With the b_{min} parameterization of Equation 2.7, the results, in fm, were:

$$\Delta b = \begin{cases} .79 \pm .01 \pm .16 & \text{no unfolding} \\ .84 \pm .01 \pm .17 & \text{first unfolding} \\ .85 \pm .02 \pm .18 & \text{second unfolding} \end{cases} ,$$

where the first errors are statistical and the second, systematic. Then, the recoil corrected version of Equation A.1 was used to extrapolate σ_{NUC} to the other targets. As in the first method, the specifically electromagnetic cross sections were obtained by subtraction:

$$\sigma^X_{\text{EMD}} = \sigma^X_{\Sigma} - \sigma^X_{\Sigma,nuc} \quad . \tag{7.15}$$

The results of this method are given in Table 7.6 and plotted in Figure 7.4. Again, only the statistical errors are plotted for the Al, Cu, and Ag cross sections, since the normalization error has the effect of shifting these points up or down simultaneously. For the U data point, however, the normalization uncertainty is no longer independent of the normalization of the Be point, since $\sigma^U_{\Sigma,nuc}$ was extrap-

	no unfolding σ_{EMD}	unfolding #1 σ_{EMD}	unfolding #2 σ_{EMD}
Al	$73 \pm 8 \pm 14$	$75 \pm 13 \pm 14$	$70 \pm 21 \pm 13$
Cu	$240 \pm 12 \pm 47$	$250 \pm 18 \pm 49$	$243 \pm 29 \pm 47$
Ag	$390 \pm 14 \pm 76$	$397 \pm 22 \pm 78$	$374 \pm 34 \pm 73$
U	$555 \pm 18 \pm 305$	$586 \pm 31 \pm 323$	$575 \pm 48 \pm 324$

Table 7.6: EMD cross sections in mb extracted with the second method described in the text.

olated from the Be data. With this method, the normalization error associated with $\sigma^U_{\rm EMD}$ is given by

$$\left(\Delta\sigma^U_{\rm EMD}\right)^2_{norm} = \left(\Delta\sigma^U_{\Sigma}\right)^2_{norm} + \left(\Delta\sigma^U_{\Sigma,nuc}\right)^2_{norm} \quad . \tag{7.16}$$

The correlation of $\left(\Delta\sigma^U_{\rm EMD}\right)_{norm}$ with the normalization of the other points makes the display of a meaningful error bar for the U cross section more problematical than in the first method. The error bar in the figure was computed from the quadrature sum of the statistical error and a 20% normalization error, which is not the same as the normalization error given by Equation 7.16 and listed in Table 7.6.

The agreement between data and theory in Figure 7.4 is very poor, to say the least. The Al, Cu, and Ag points appear to have the correct Z_{targ} dependence, but the U point is clearly too low in relation to the other points. One possibility is that the normalization of the light target data is correct and that the U point needs to be moved upward. In this case, the absolute magnitudes of the theoretical predictions would be too low by at least 20%. However, the theoretical calculations are quite sensitive to the cutoff impact parameters, b_{min}, so the discrepancy could be eliminated by simply adjusting these quantities downward. For example, changing the number outside of the brackets in Equation 2.7 from 1.34

to 1.17 shifts the solid curve of Figure 7.4 up into almost perfect agreement with the Al, Cu, and Ag points.† An upward shift of the U point by $\sim 32\%$, which is within its normalization error, then brings it into agreement with the revised theory.

Another possibility is that the U normalization is correct and that the normalization of the light targets is too high. Since the nuclear cross sections were determined by extrapolation from the Be point in this second method, shifting the normalization of the light targets downward, while leaving the U normalization unchanged, has the effect of increasing $\sigma^U_{\rm EMD}$. To see how large a shift in the normalization of the Be-Ag points is required to give results in agreement with the original calculations, a fit to the sum cross sections was made, in which the normalization, N, of the Be, Al, Cu, and Ag data points was allowed to vary as a free parameter. First, a χ^2 was defined:

$$\chi^2 = \sum_{i=1}^{4} \left[\frac{\sigma^i_{fit} - N\sigma^i_{data}}{\Delta\sigma^i_{data}} \right]^2 \quad , \tag{7.17}$$

where

$$\sigma^i_{fit} = \sigma^i_{\rm EMD} + \sigma^i_{\rm NUC} \quad , \tag{7.18}$$

and σ^i_{data} refers to the sum cross sections of Table 7.4. The electromagnetic cross sections were taken from one of the three columns of Table 2.2. The nuclear cross sections were calculated from the geometrical model, allowing Δb to be a second free parameter. The statistical errors of Table 7.4 were used for the weights, $\Delta\sigma^i_{data}$. The χ^2 was then minimized simultaneously with respect to N and Δb.

The quality of the fits depended slightly on the unfolding correction, with the data of the third column of Table 7.4 giving the lowest χ^2's. The results of the three fits for these data are given in Table 7.7 and plotted in Figure 7.5.

† The $\sigma_{\rm NUC}$ values calculated from the geometrical model are also affected by a change in the b_{min} values. This effect can be offset by adjusting Δb in the opposite direction, however.

	N	Δb	$\chi^2/d.f.$	T_{fit}	# std. dev.
rc	.67	.56	2.9	.056	1.6
nrc	.77	.65	3.0	.065	1.1
ww	.57	.49	3.0	.050	2.0

Table 7.7: Results of the normalization fits.

The triangles in the plot are at the same locations as the triangles of Figure 7.2, and give the sum cross sections as determined from the mask calibration data. The 20% normalization error of the U point has been included. The squares, circles, and diamonds are the Be-Ag points after multiplication by .77, .67, and .57, respectively (see the table). Likewise, the smooth curves represent the best fits for the three models. To get the normalized χ^2 in the table, the number of degrees of freedom was taken to be two. To the naked eye all the fits look reasonable. The high values of the χ^2's could reflect additional uncertainties in the data which were not included in the weights. For example, if an additional uncertainty of 2% is attributed to the data points, then good confidence levels for the fits can be obtained. On the other hand, the geometrical model used to calculate the nuclear contributions can hardly be expected to be accurate at the level of 2%. The location of the U point seems to favor the top curve in the figure, but its normalization error is so large that one cannot rule out the other two.

Recall from Section 5.5, that the mask transmission factor for the Be-Ag data points was determined, from the calibration data, to be

$$T = .084 \pm .017 \ .$$

The fourth column of Table 7.7 was obtained by multiplying this T by the fitted N. The fifth column was then obtained by subtracting T_{fit} from T and dividing by .017. The results show that, within two standard deviations, all of the fits are

consistent with the calibration data.

7.3 Conclusions

The results of the normalization fits show that the Be-Ag EMD cross sections, as extracted by the second method, have a Z_{targ} dependence which is consistent with the predictions of the equivalent photon approximation. However, fits to the light target points alone were not able to distinguish between calculations which included the E2 enhancement and/or the recoil correction, and the straightforward Weizsäcker-Williams calculation.

As far as the absolute magnitudes of the cross sections are concerned, one cannot say with certainty whether it is the U data point which is too low or whether the other points are too high. Calculations with the b_{min} parameterization of Equation 2.7 favor the second possibility, but a simple rescaling of that parameterization by 12% can give results in agreement with the first possibility.

Further measurements are clearly needed in order to resolve these ambiguities. The normalization problems which plague the results of this thesis can be easily avoided in future experiments by, for example, using an ion chamber to count the beam flux instead of a plastic scintillator covered with a Pb mask. In principle, the Z resolution could also be improved by adding one or more additional ΔE detectors to each telescope. Let δZ_{par} denote the spread in Z_{par} values for a given fragment species due to statistical fluctuations, $\delta\Delta E$, of the signals from the ΔE detectors. From a straightforward generalization of Equation 5.11 to the case where there are N ΔE detectors in a single telescope, it can be easily demonstrated that:

$$\frac{\delta Z_{par}}{Z_{par}} = \frac{1}{\sqrt{N}} \frac{\delta \Delta E}{\Delta E} \quad . \tag{7.19}$$

The problems with the Z resolution were not caused solely by the ΔE fluctuations,

so it is difficult to say exactly how much improvement could be gained by adding more ΔE detectors to the telescopes used in this experiment. An alternative possibility would be to use a completely different detector system, such as a Time Projection Chamber [46], to do this type of measurement.

Aside from improvements to the experimental apparatus, either more or different targets should be used in future experiments. In particular, measurements should be made on a target with an atomic number between silver and uranium, *e.g.* gold. Also, it seems likely that measurements at more than one beam energy will be needed in order to provide conclusive confirmation of the theoretically predicted E2 enhancement.

Appendix A

Geometrical Scaling of σNUC

A calculation from first principles of the nuclear contribution to the cross section of a process such as the fission of a 120 MeV/A ^{238}U projectile in a heavy-ion collision could, itself, be the subject of an entire thesis. However, it is not unreasonable to expect that the most important factor governing the target dependence of $\sigma_{\rm NUC}$ is the geometrical size of the target nucleus. The argument can be made, therefore, that the relative magnitude of $\sigma_{\rm NUC}$ from target to target should follow a simple scaling law. Thus, the argument goes, if one is able to measure the absolute magnitude of $\sigma_{\rm NUC}$ for one target, its absolute magnitude for other targets is also, to first order, determined.

First, consider the case where the projectile is assumed to move along a straight-line trajectory. Since two or three nucleons, at most, are lost from the projectile in the processes which we are interested in, only the most peripheral collisions will be expected to contribute — say, from where the surfaces of the two nuclei just begin to touch at an impact parameter, b_{min}, to some slightly smaller impact parameter, $b_{min} - \Delta b$. Such a region of impact parameters defines an annulus, centered at $b_{min} - \Delta b/2$ with a width Δb, the area of which gives the

classical geometrical cross section [3]:

$$\sigma_{\rm NUC}^{geom} = 2\pi \left(b_{min} - \frac{\Delta b}{2} \right) \Delta b \ . \tag{A.1}$$

If one of the parameterizations given in Chapter 2 for b_{min} is used and the total cross section is measured for a light target such as Be, where the electromagnetic contribution is expected to be negligible, then Δb can be determined:

$$\Delta b = b_{min} - \sqrt{b_{min}^2 - \frac{\sigma^{Be}}{\pi}} \ . \tag{A.2}$$

Equation A.1 can then be used to extrapolate $\sigma_{\rm NUC}$ to the heavier targets.

At the beam energy of this experiment, however, the projectile does not always travel in a straight line, so the above arguments need to be modified. As in Section 2.2, let ρ denote the distance of closest approach in a collision at impact parameter b. Assuming the projectile follows a classical Rutherford trajectory, the relation between ρ and b is given by (see Equation 2.8):

$$b^2 = (\rho - a)^2 - a^2 \ . \tag{A.3}$$

What we need to do is integrate over those impact parameters that lead to trajectories with ρ values between $\rho = \rho_{min}$ and $\rho = \rho_{min} - \Delta\rho$. Denoting these b values by b_2 and b_1:

$$\begin{aligned} \sigma_{\rm NUC}^{geom} &= 2\pi \int_{b_1}^{b_2} b db \\ &= \pi \left(b_2^2 - b_1^2 \right) \\ &= \pi \left[(\rho_{min} - a)^2 - (\rho_{min} - \Delta\rho - a)^2 \right] \\ &= 2\pi \left(\rho_{min} - a - \frac{\Delta\rho}{2} \right) \Delta\rho \ . \end{aligned} \tag{A.4}$$

Since, to first order in a, $\Delta\rho = \Delta b$, we see that the substitution:

$$b_{min} \longrightarrow b_{min} - a \ , \tag{A.5}$$

in Equation A.1, corrects for the Coulomb deflection of the trajectory. Note the opposite signs in this equation and Equation 2.10. The recoil correction has the effect of decreasing both σ_{EMD} and σ_{NUC}.

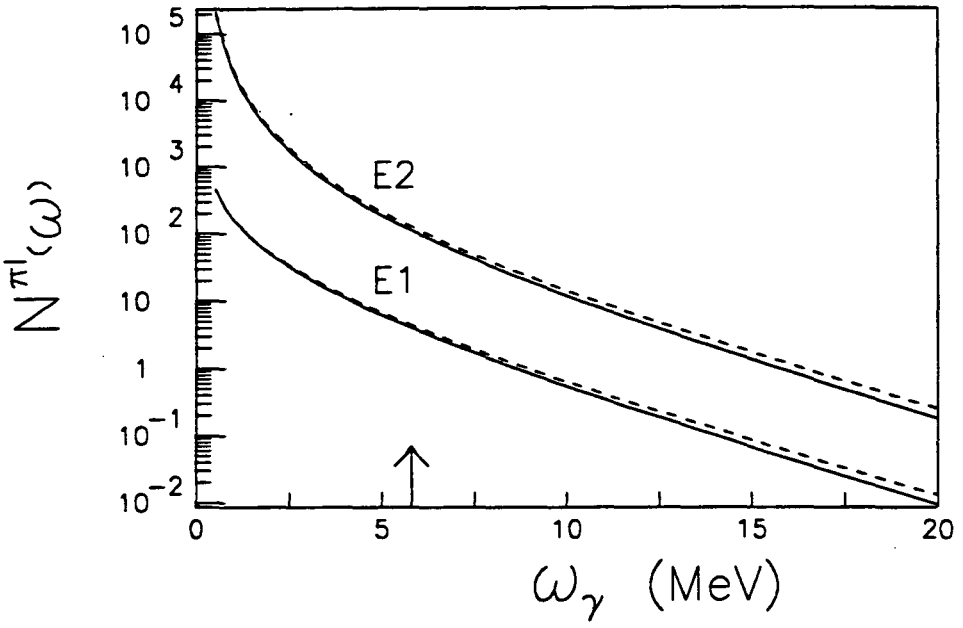

Figure 2.1: Equivalent photon number spectra with (solid) and without (dashed) the recoil correction.

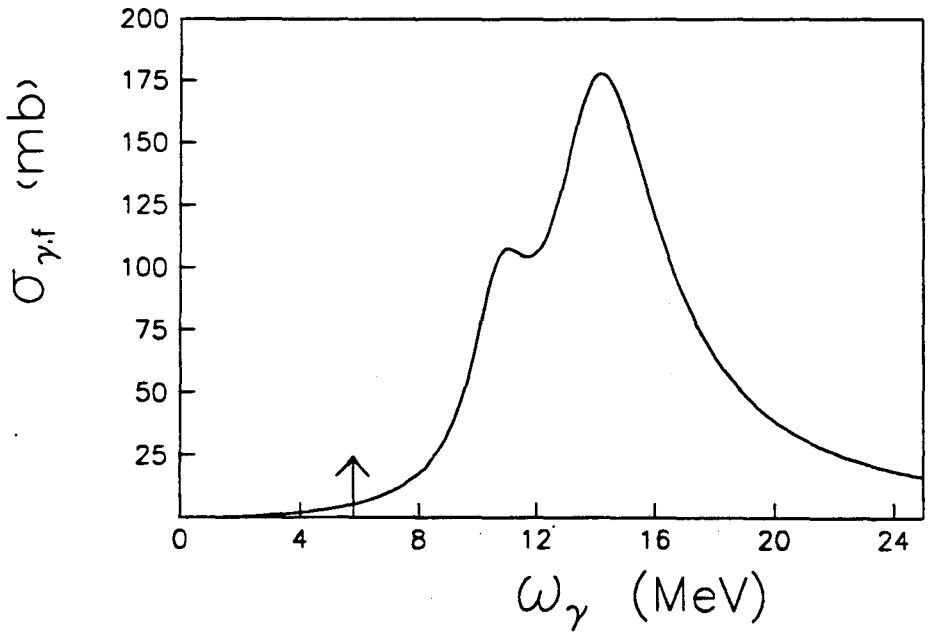

Figure 2.2: Total photofission cross section for ^{238}U.

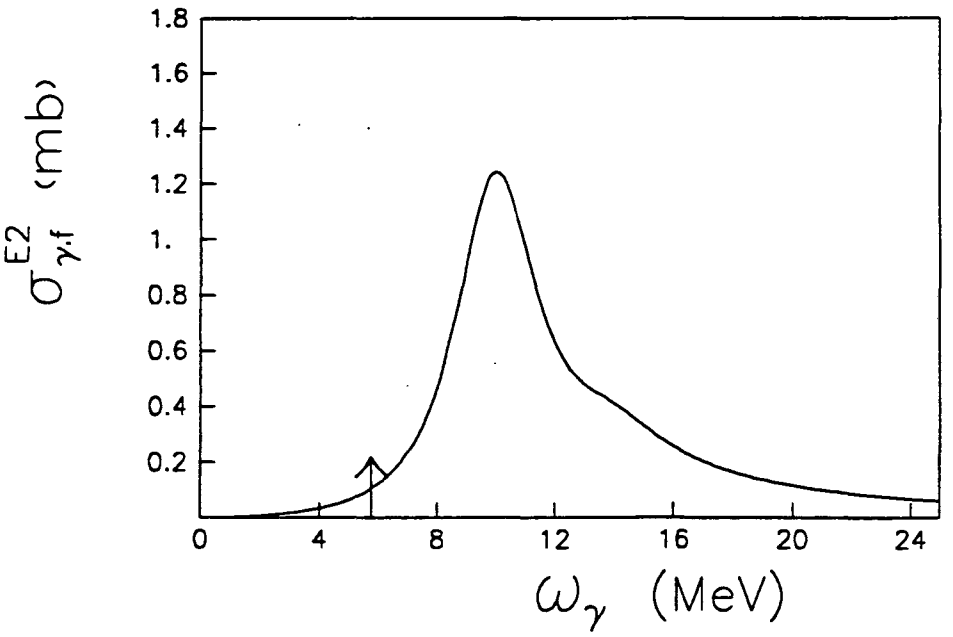

Figure 2.3: Calculated E2 photofission cross section for ^{238}U.

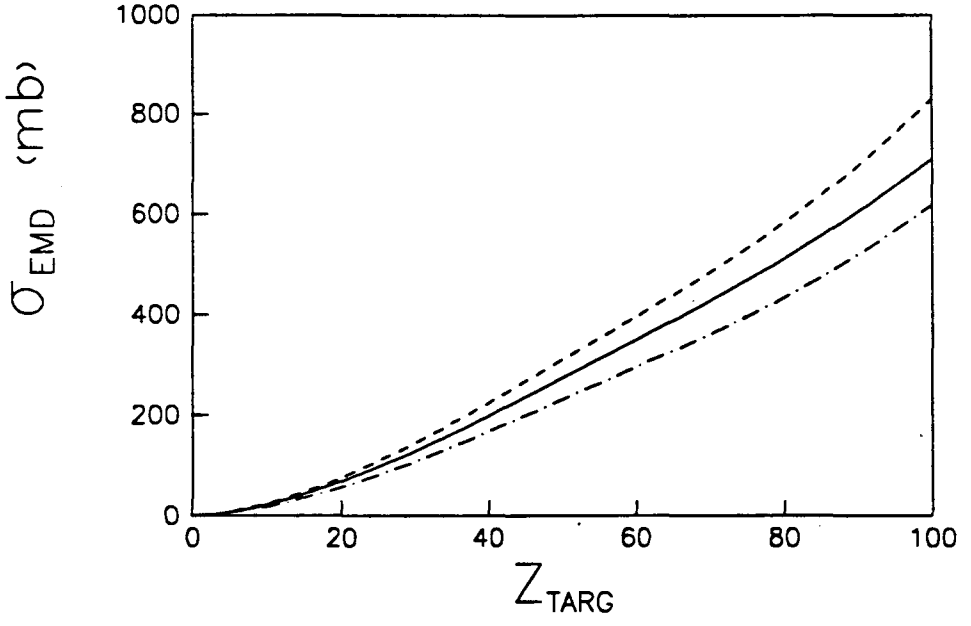

Figure 2.4: Predicted EMD cross sections.

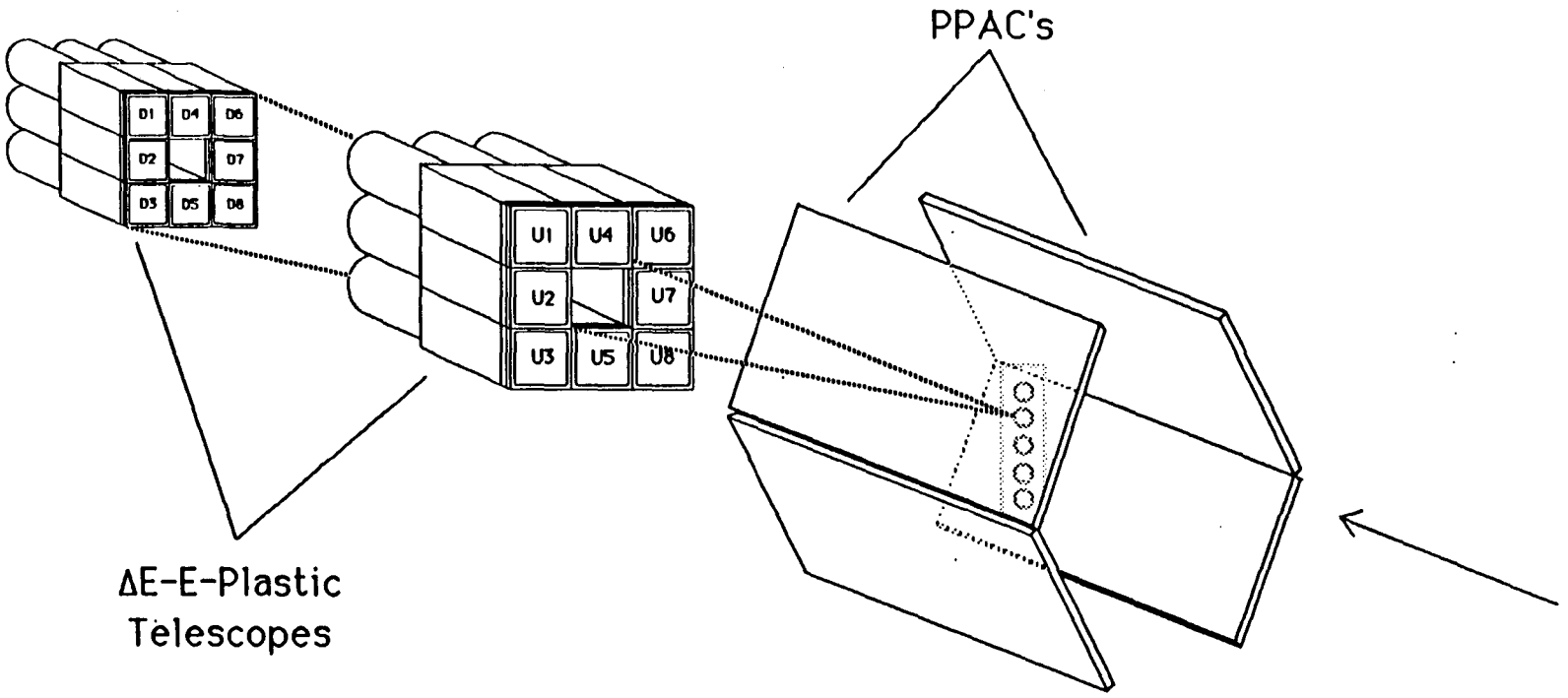

Figure 4.1: Detector setup for this experiment (not drawn to scale).

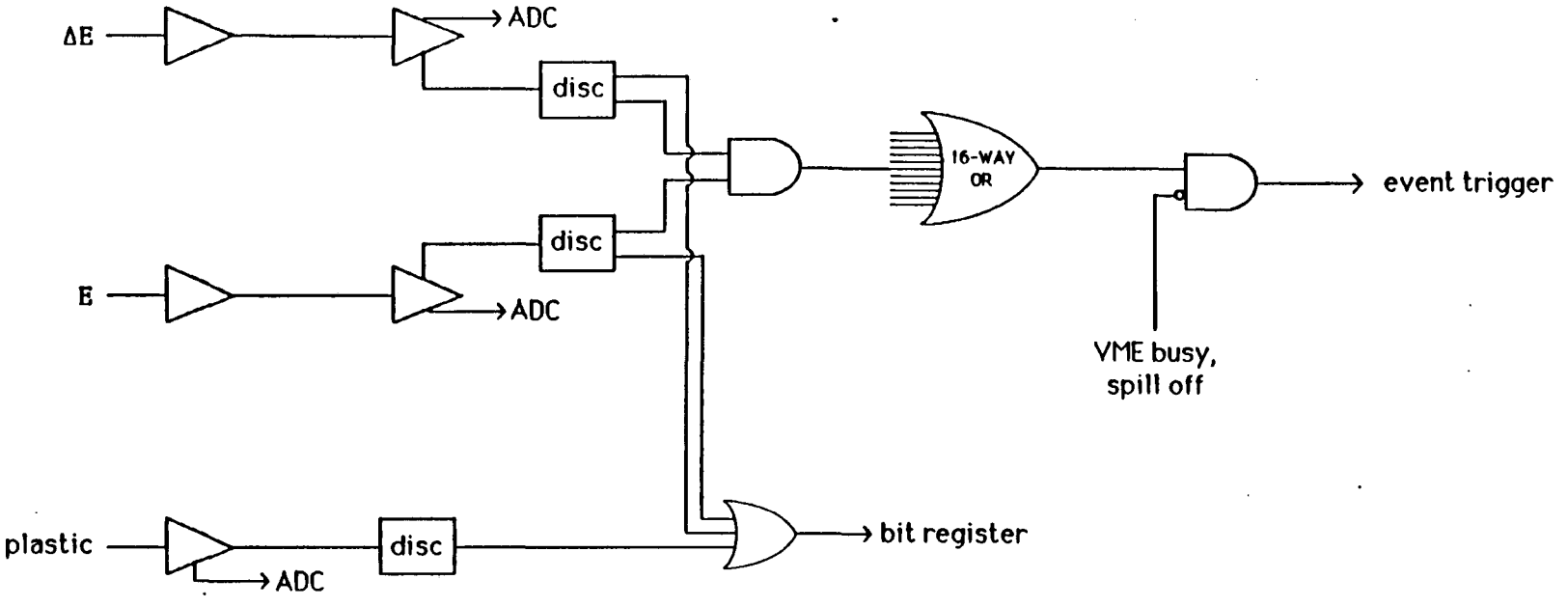

Figure 4.2: Schematic diagram of the trigger electronics.

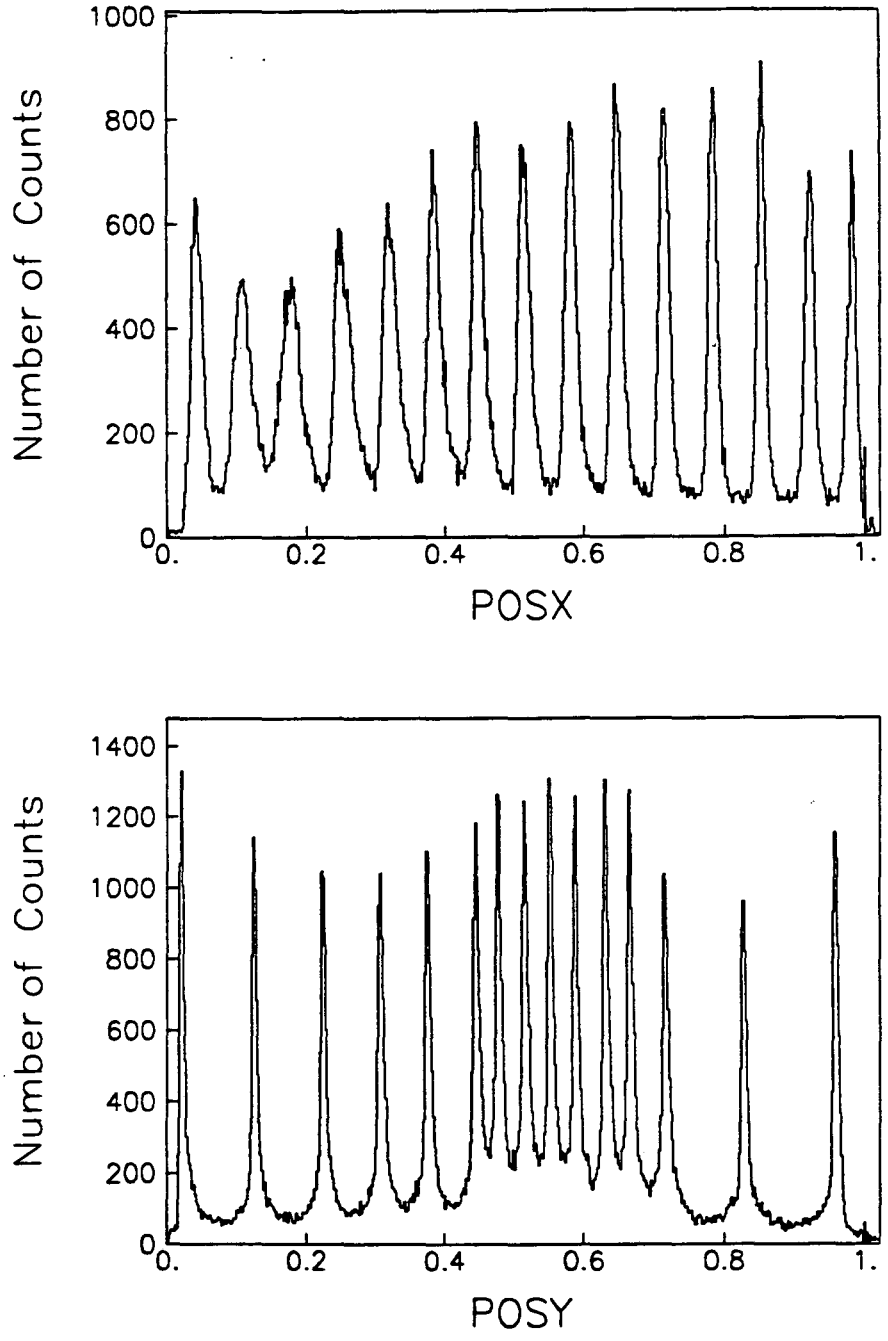

Figure 5.1: POSX and POSY for detector D7.

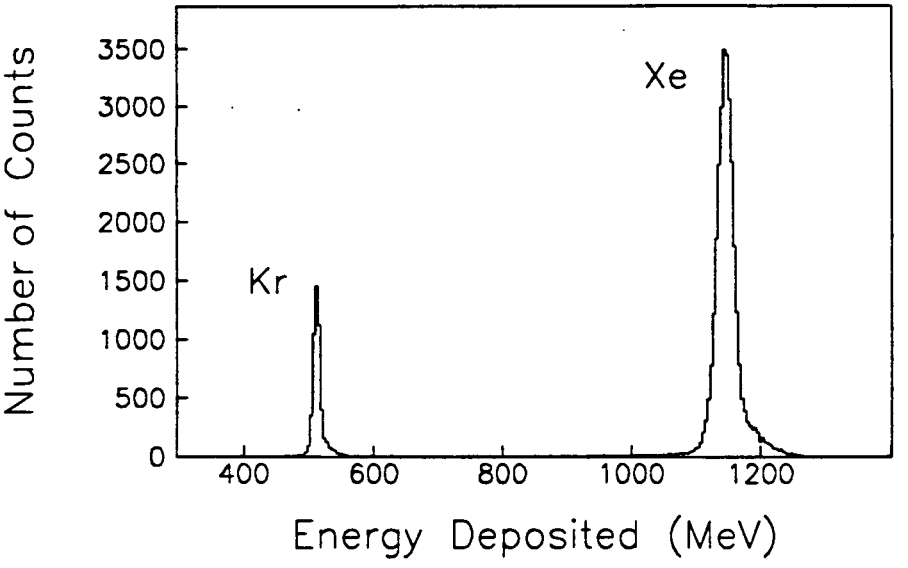

Figure 5.2: Kr/Xe calibration data for D7 ΔE.

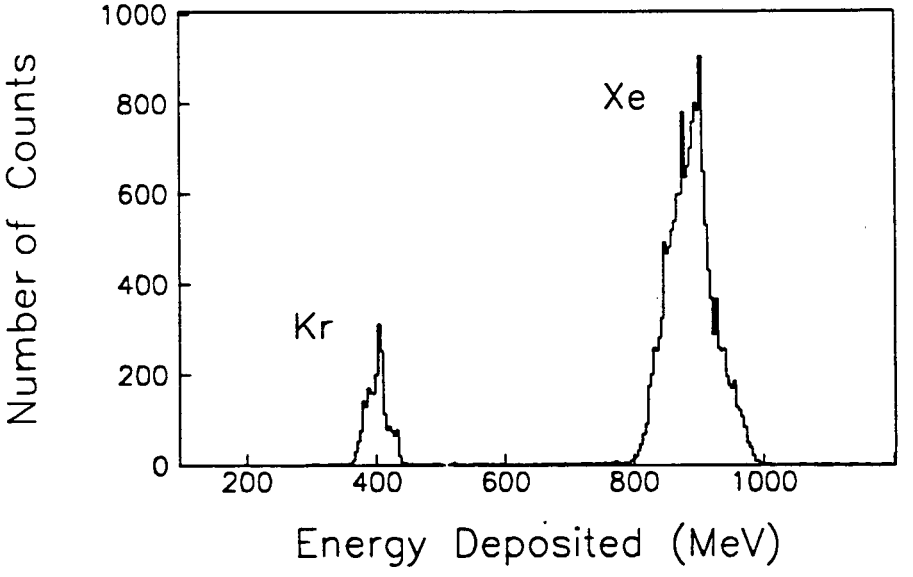

Figure 5.3: Kr/Xe calibration data for D1 ΔE.

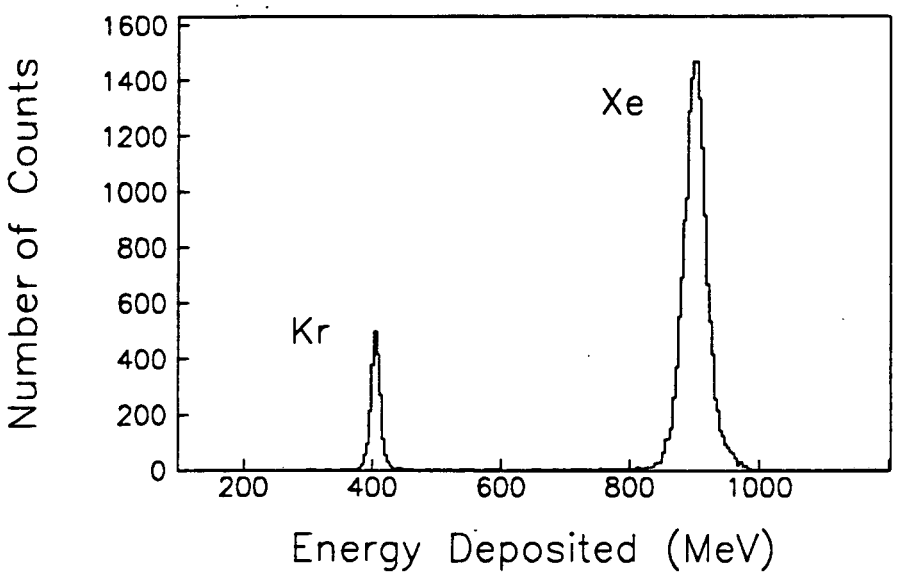

Figure 5.4: Kr/Xe calibration data for D1 ΔE after thickness correction.

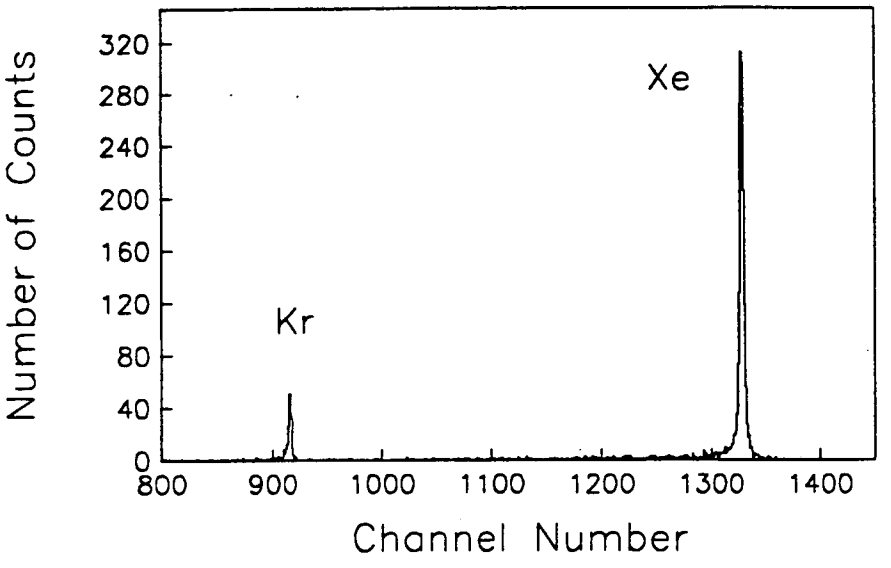

Figure 5.5: D1 E ADC spectrum for Kr/Xe calibration data.

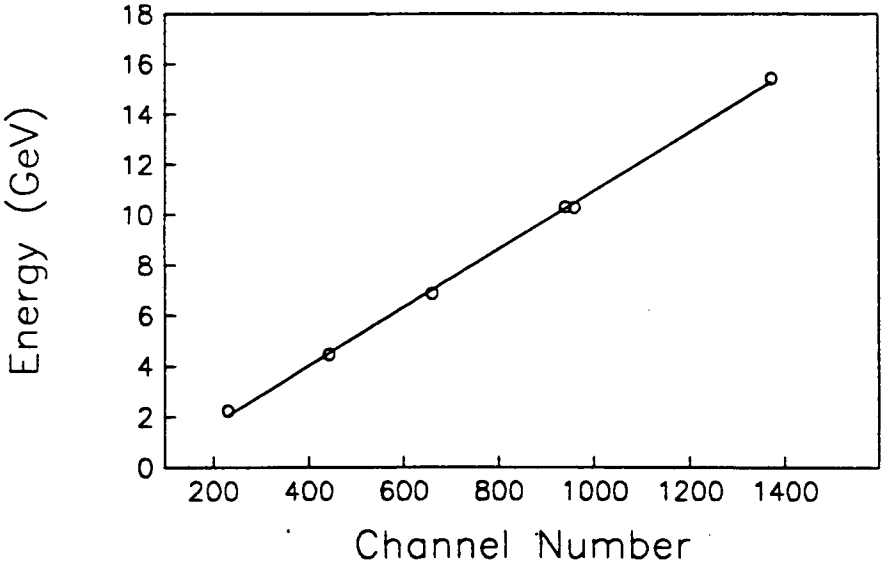

Figure 5.6: Total deposited energy vs. ADC channel number for D2 E detector.

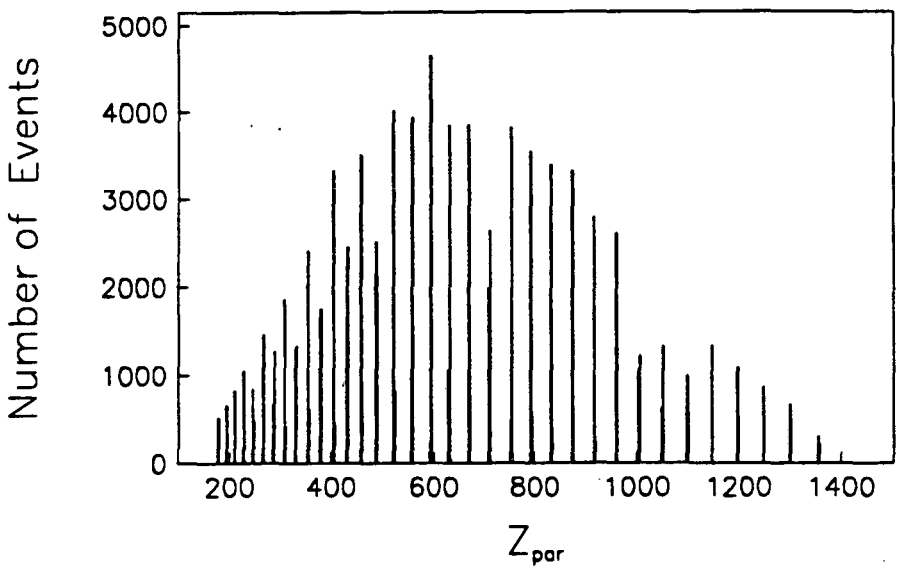

Figure 5.7: Monte Carlo events with perfect resolution.

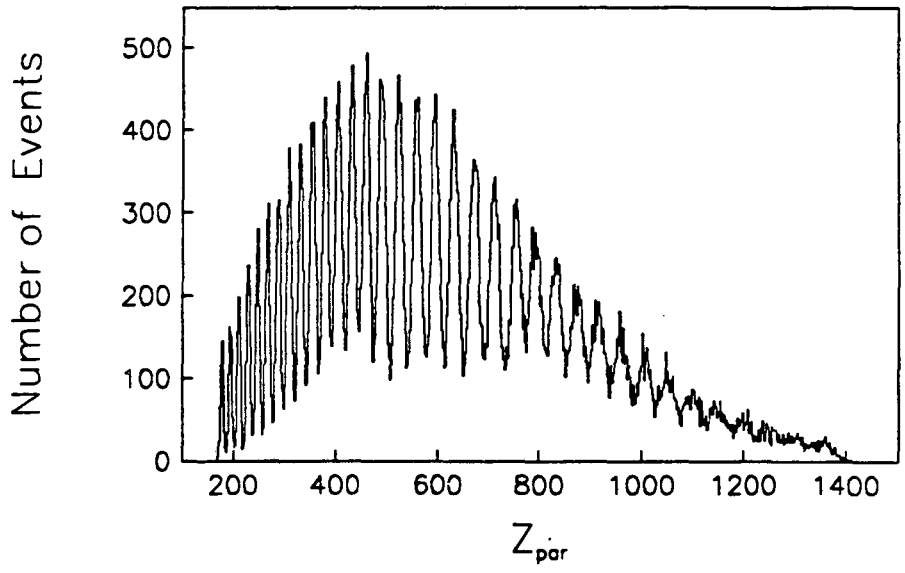

Figure 5.8: Monte Carlo events with E, ΔE, and A smearing.

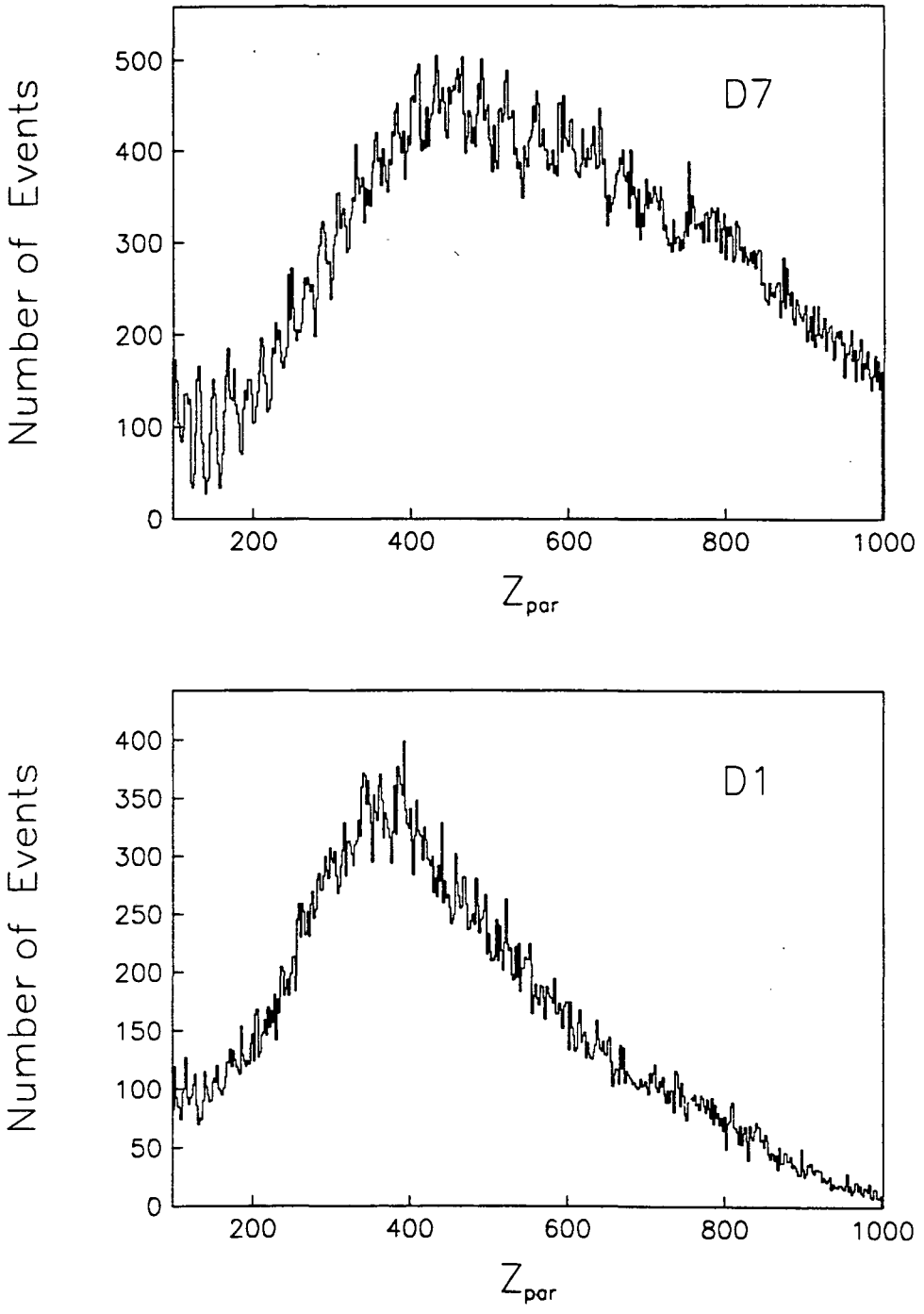

Figure 5.9: Z_{par} distributions for detectors D7 and D1.

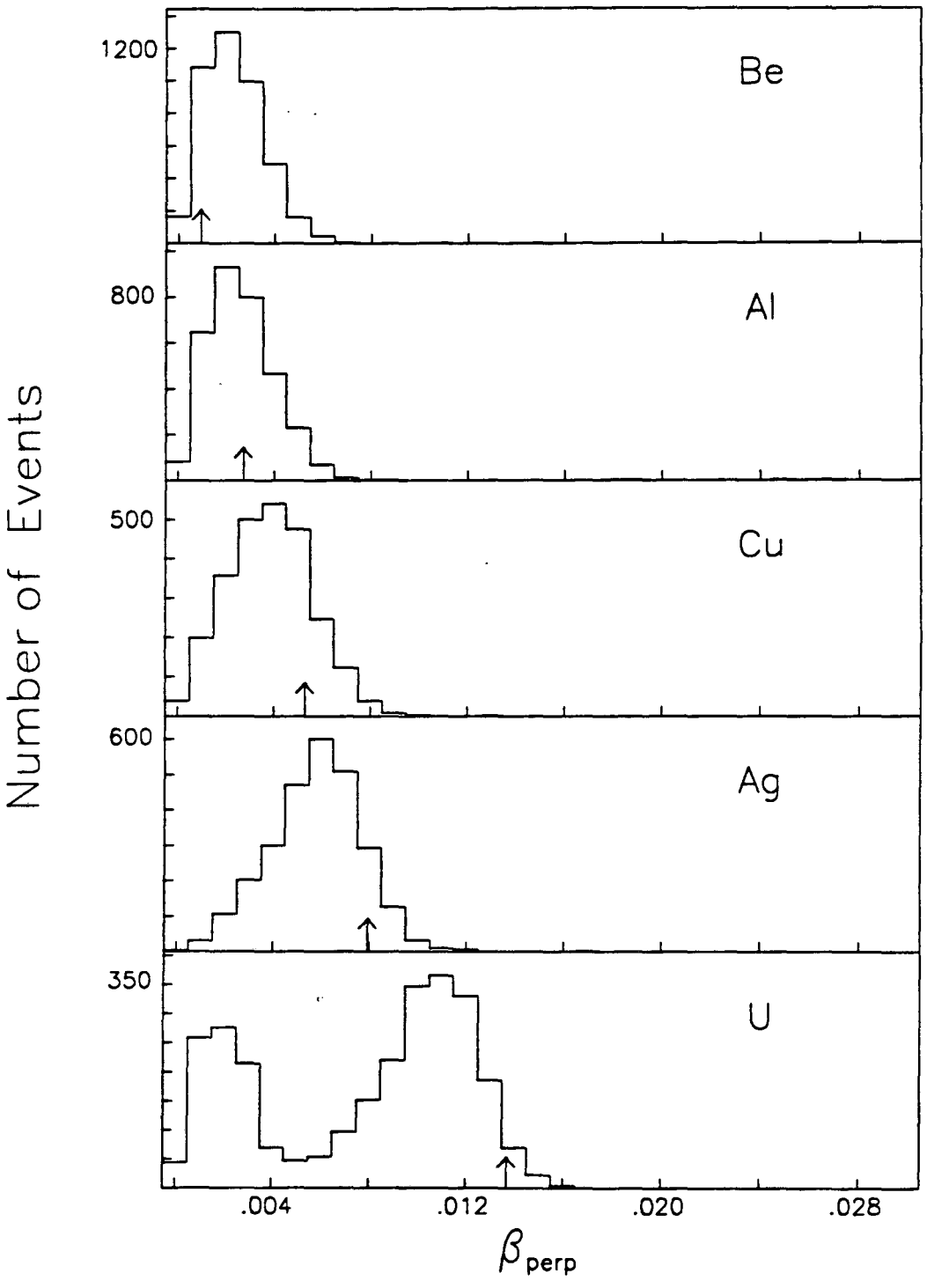

Figure 6.1: Transverse source velocities for $Z_{tot} = 92$ events.

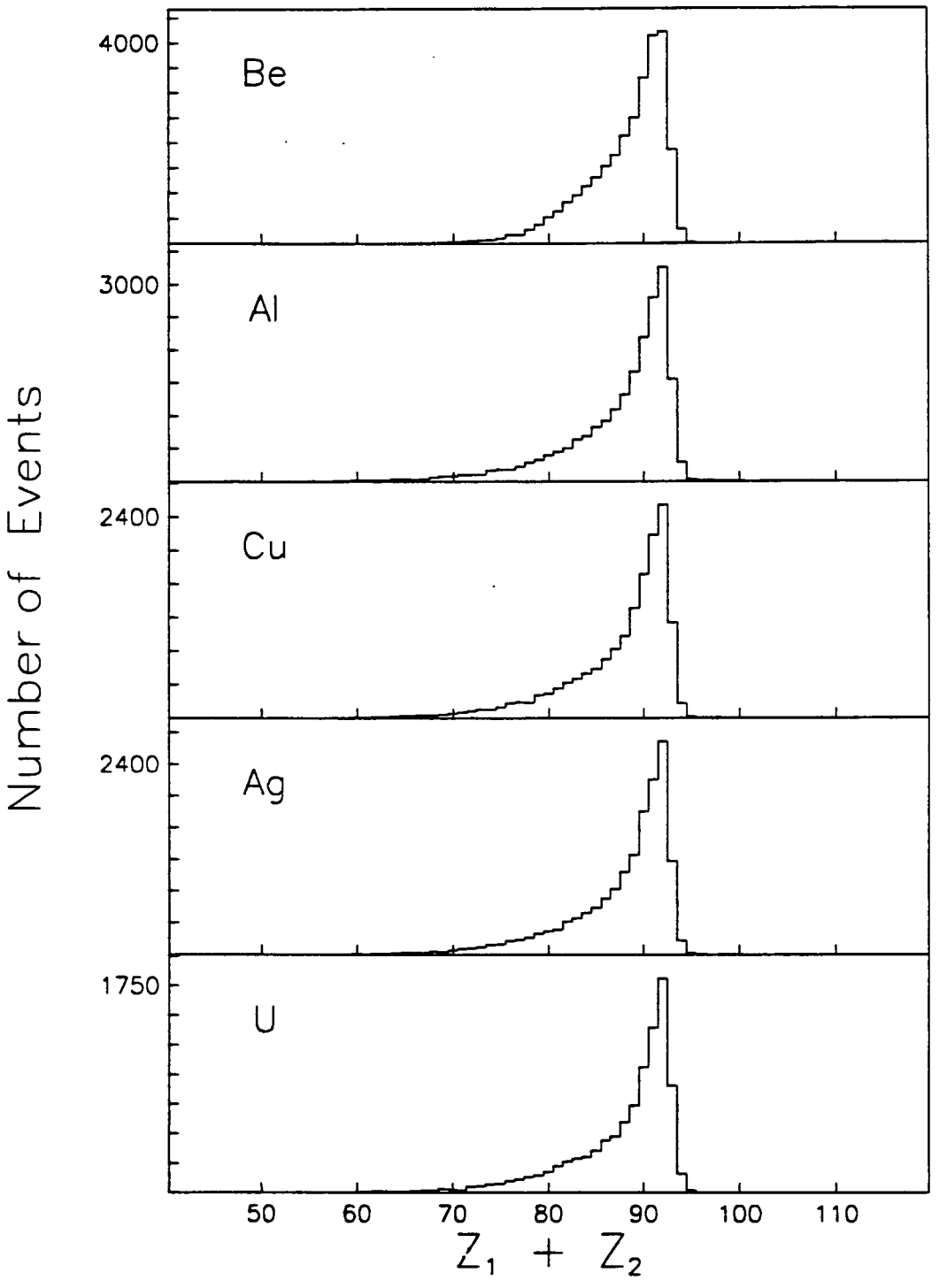

Figure 6.2: Raw $Z_1 + Z_2$ distributions.

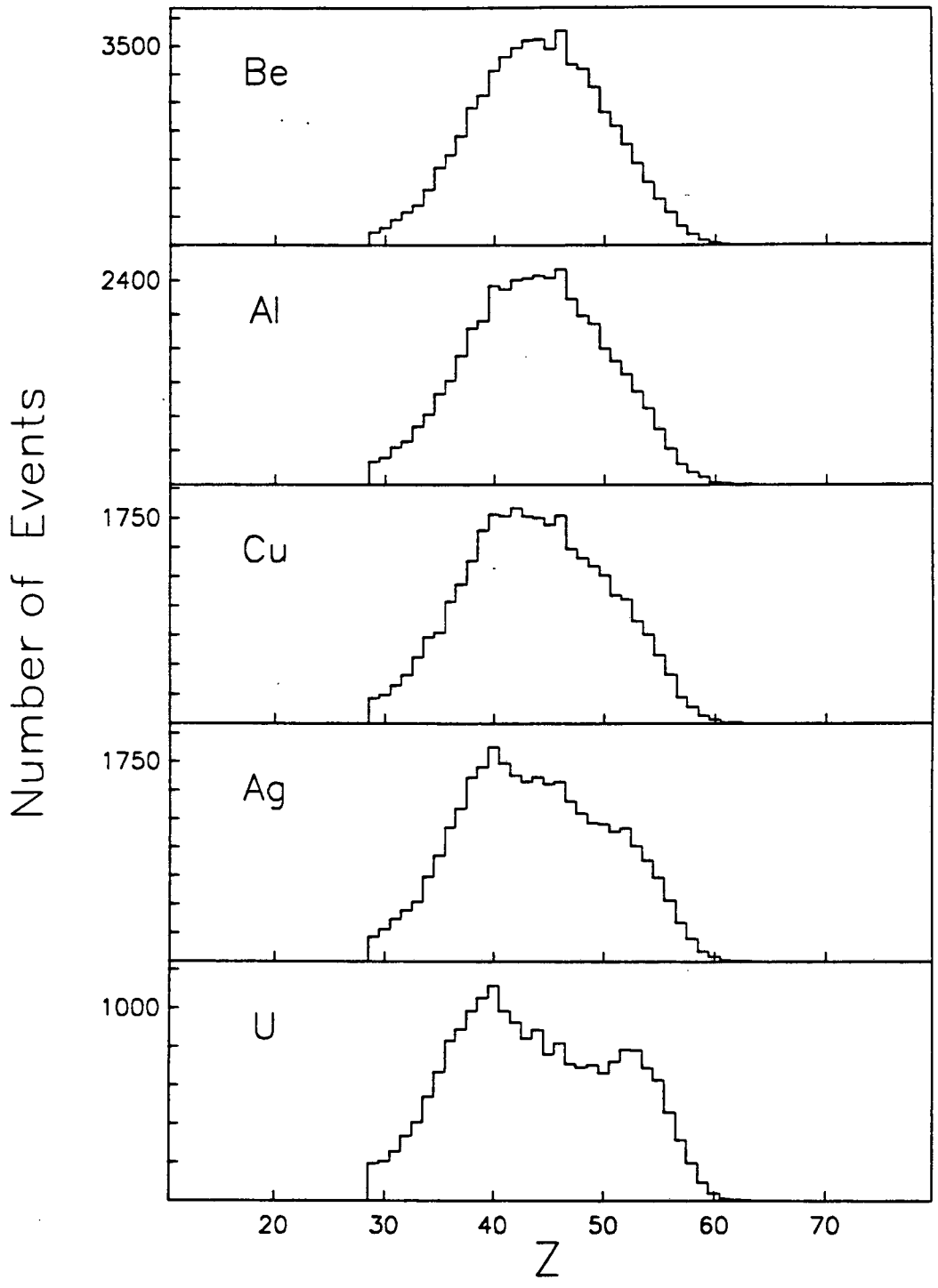

Figure 6.3: Raw Z distributions for Z_{tot} = all.

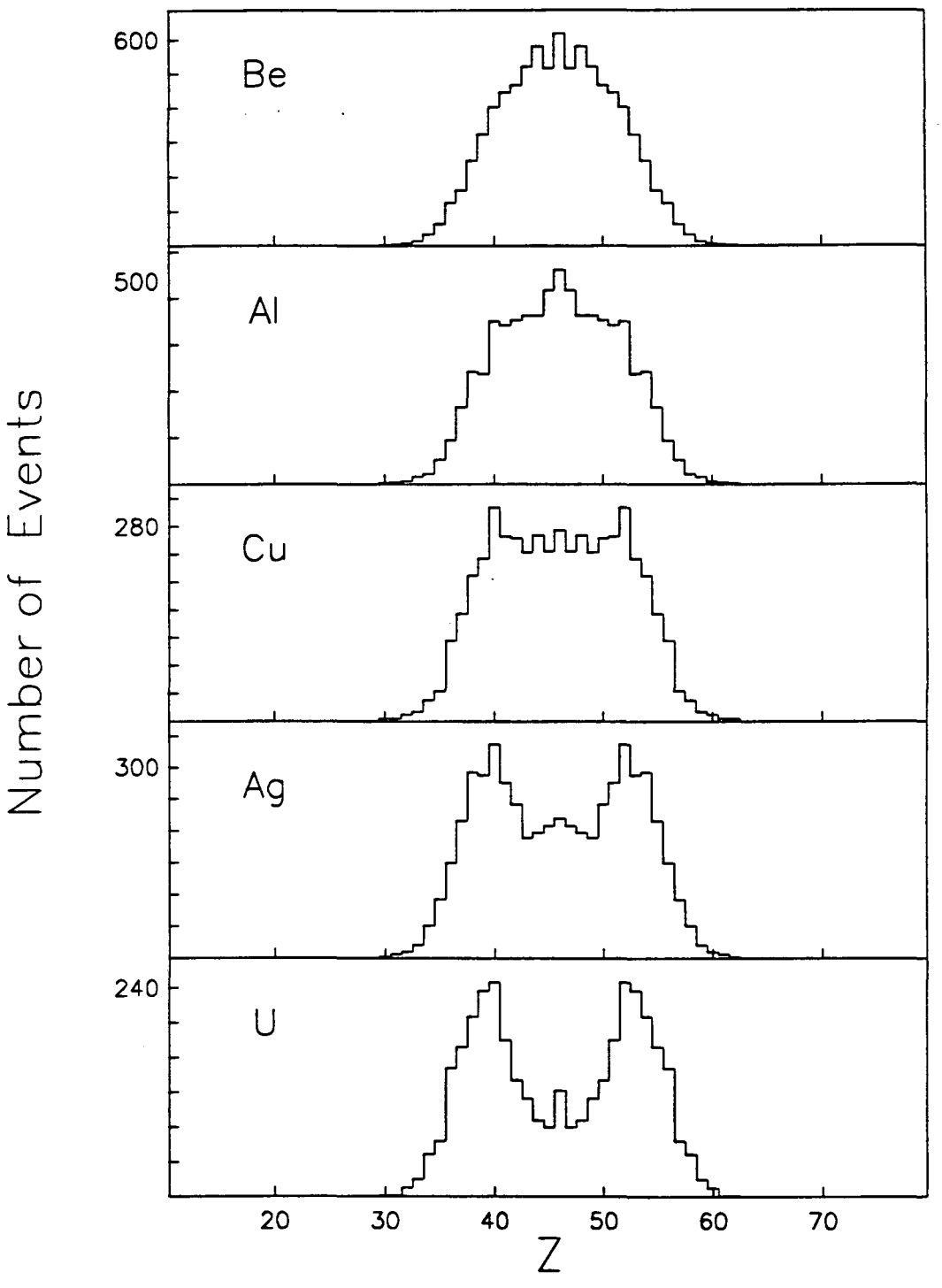

Figure 6.4: Raw Z distributions for $Z_{tot} = 92$.

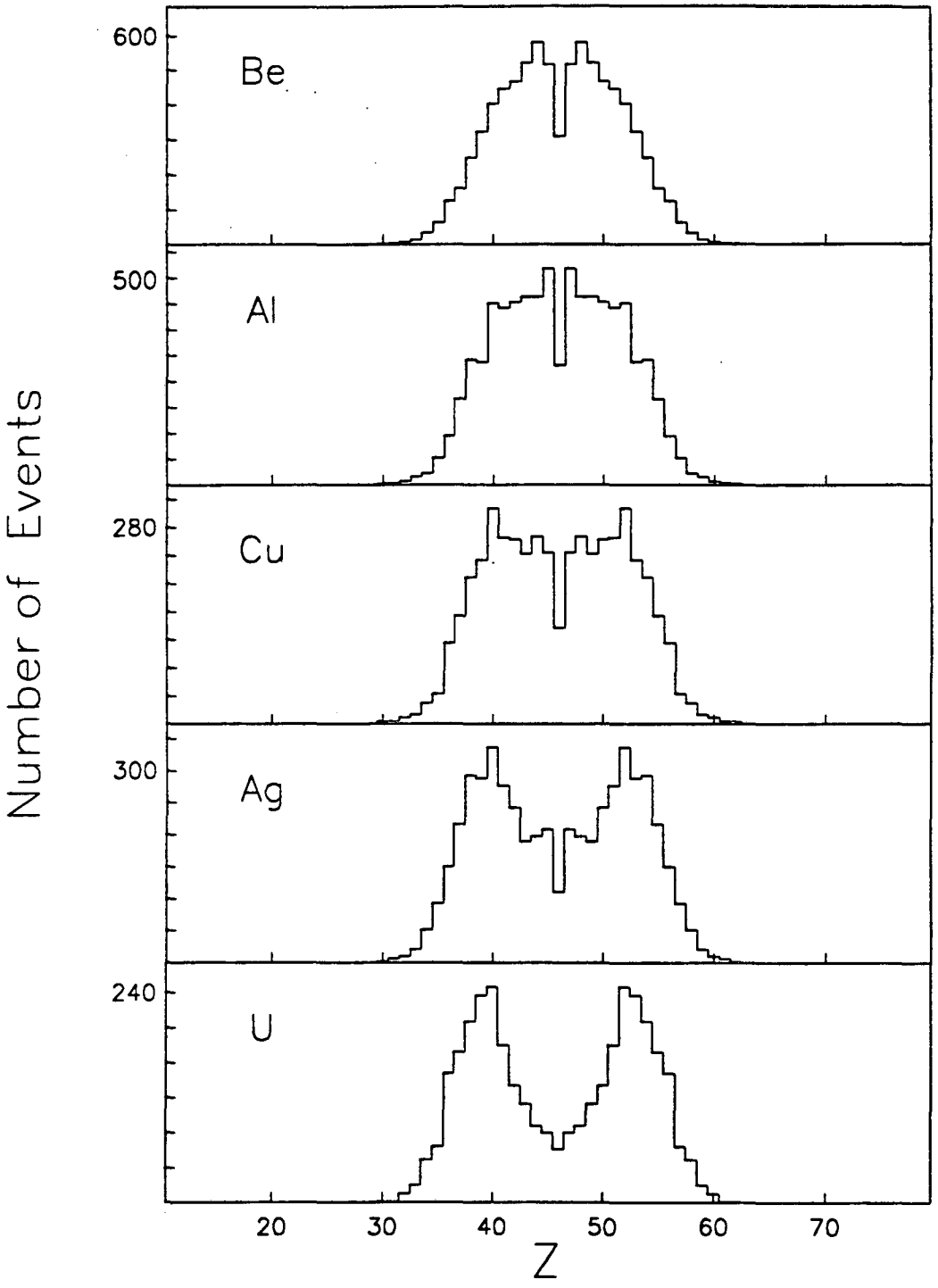

Figure 6.5: Same as Figure 6.4 but with $Z = 46$ bins divided by two.

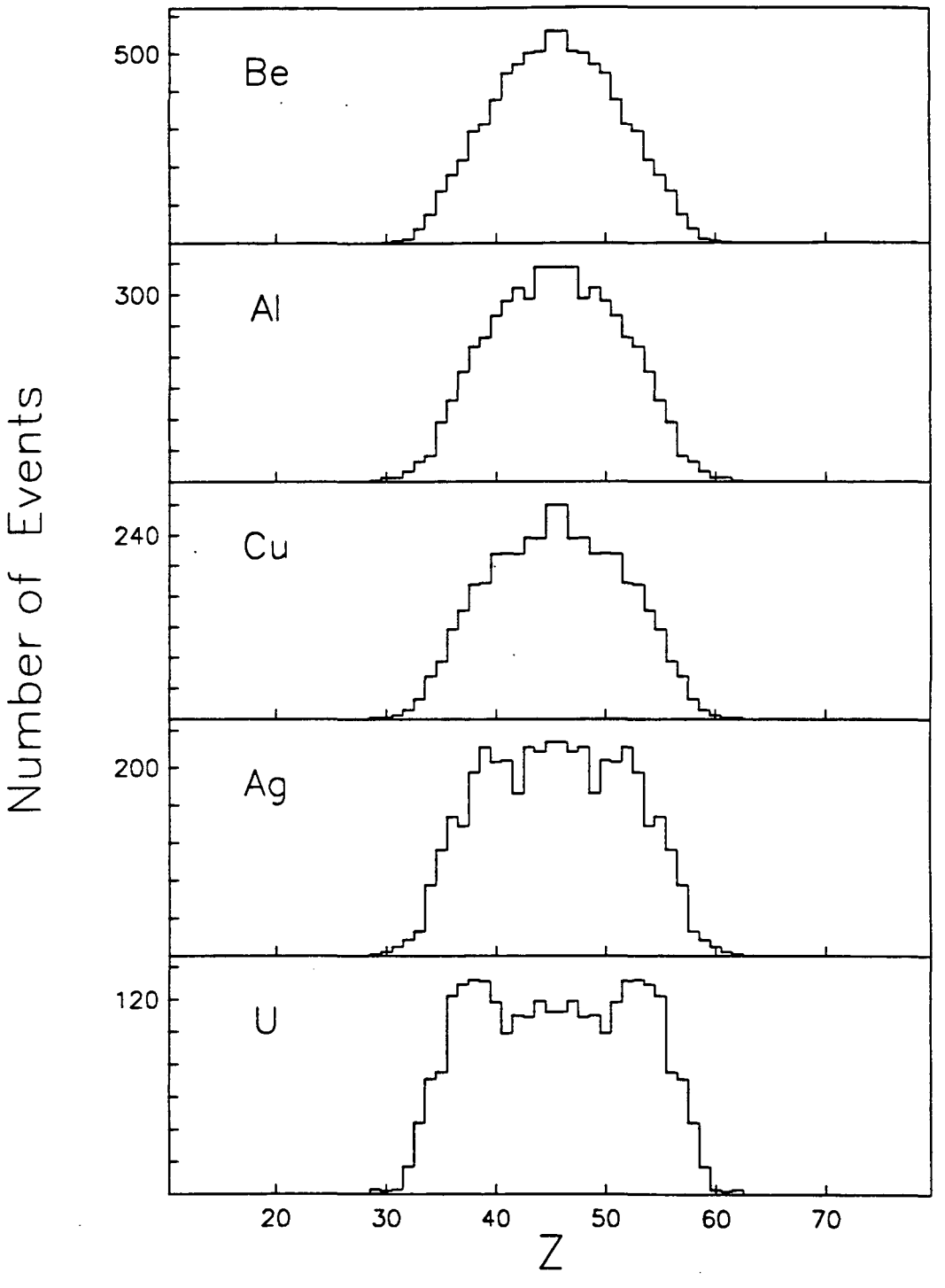

Figure 6.6: Raw Z distributions for $Z_{tot} = 91$.

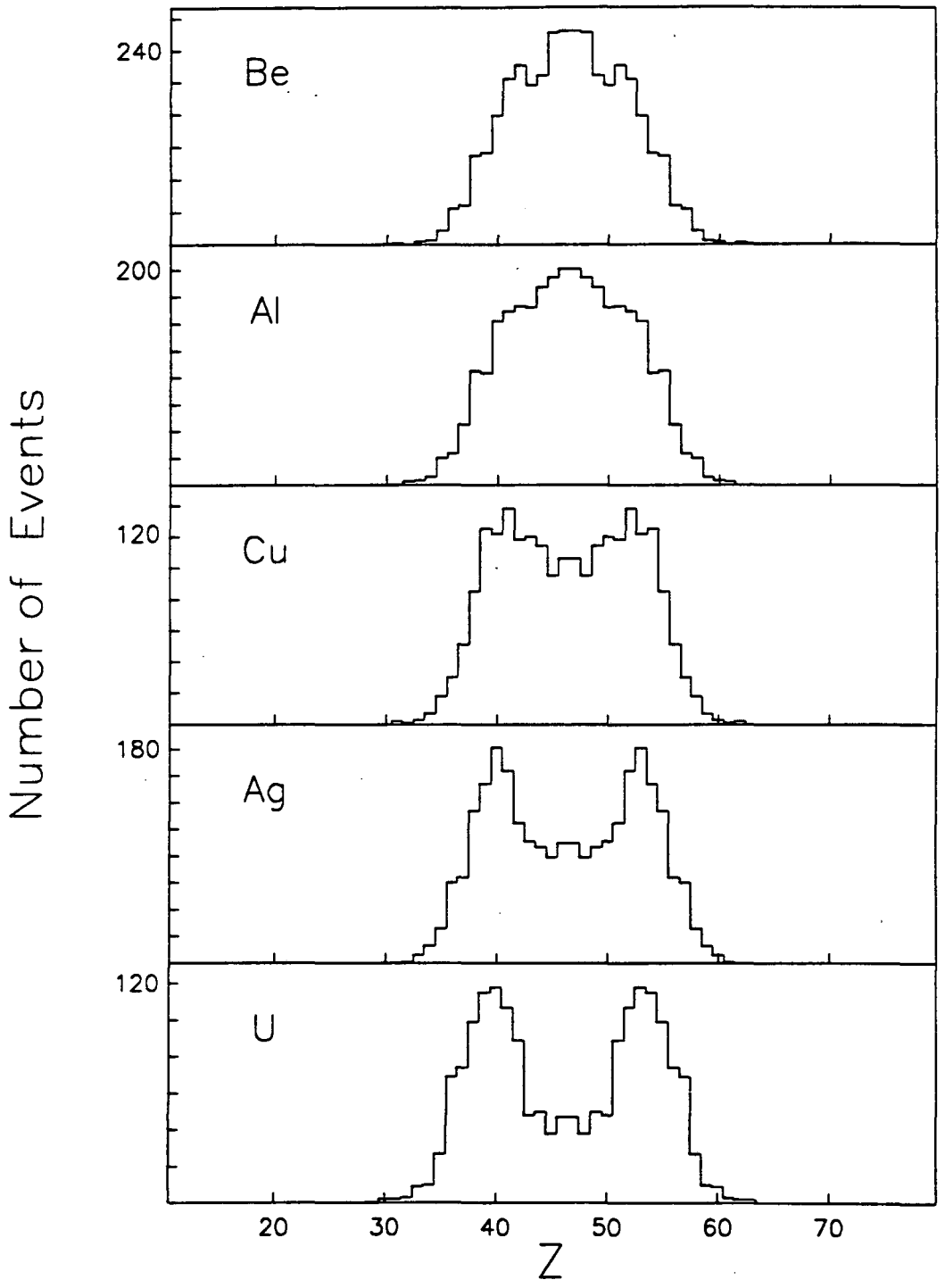

Figure 6.7: Raw Z distributions for $Z_{tot} = 93$.

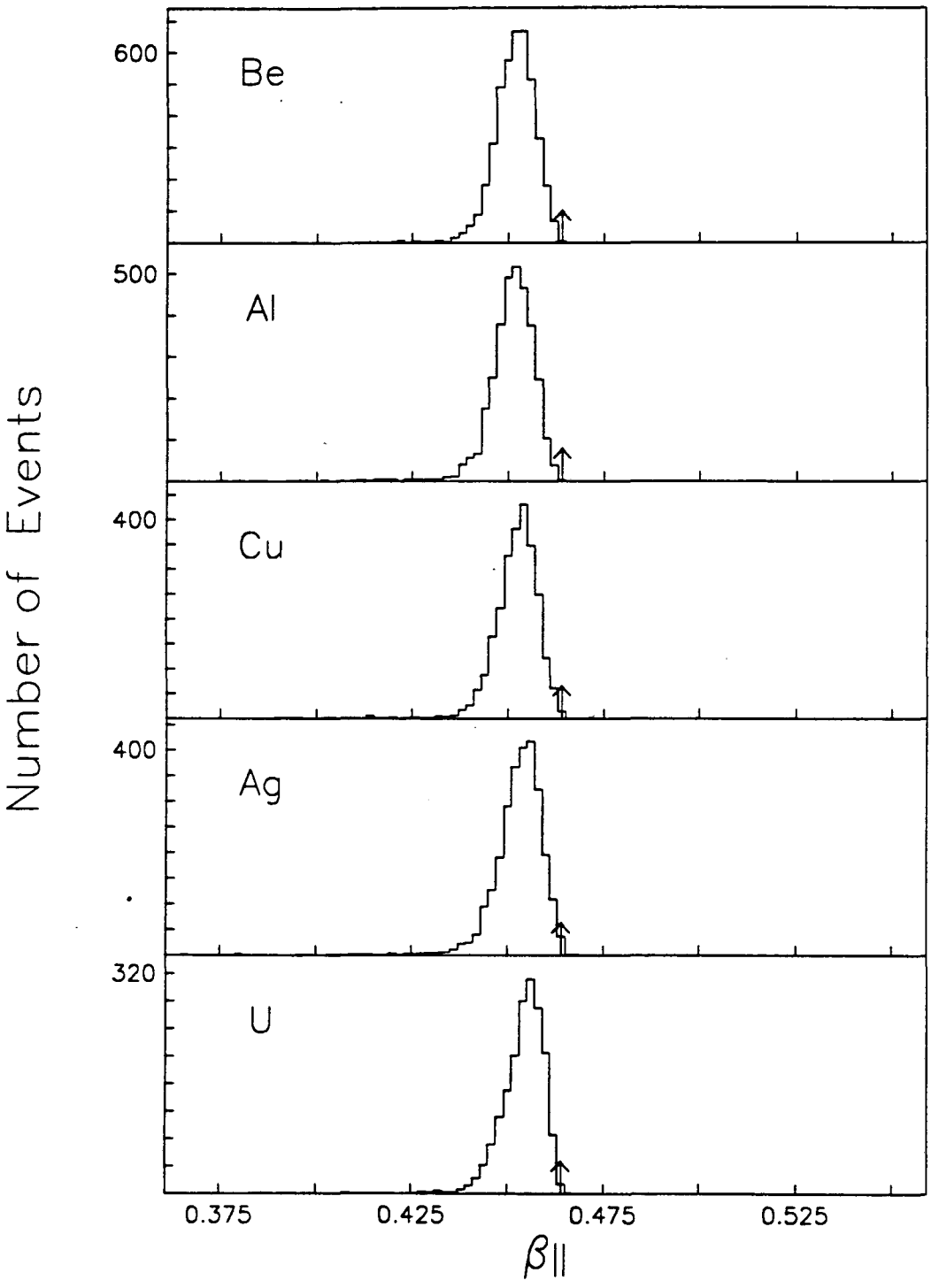

Figure 6.8: Parallel source velocities for $Z_{tot} = 92$, extracted using cold fission masses.

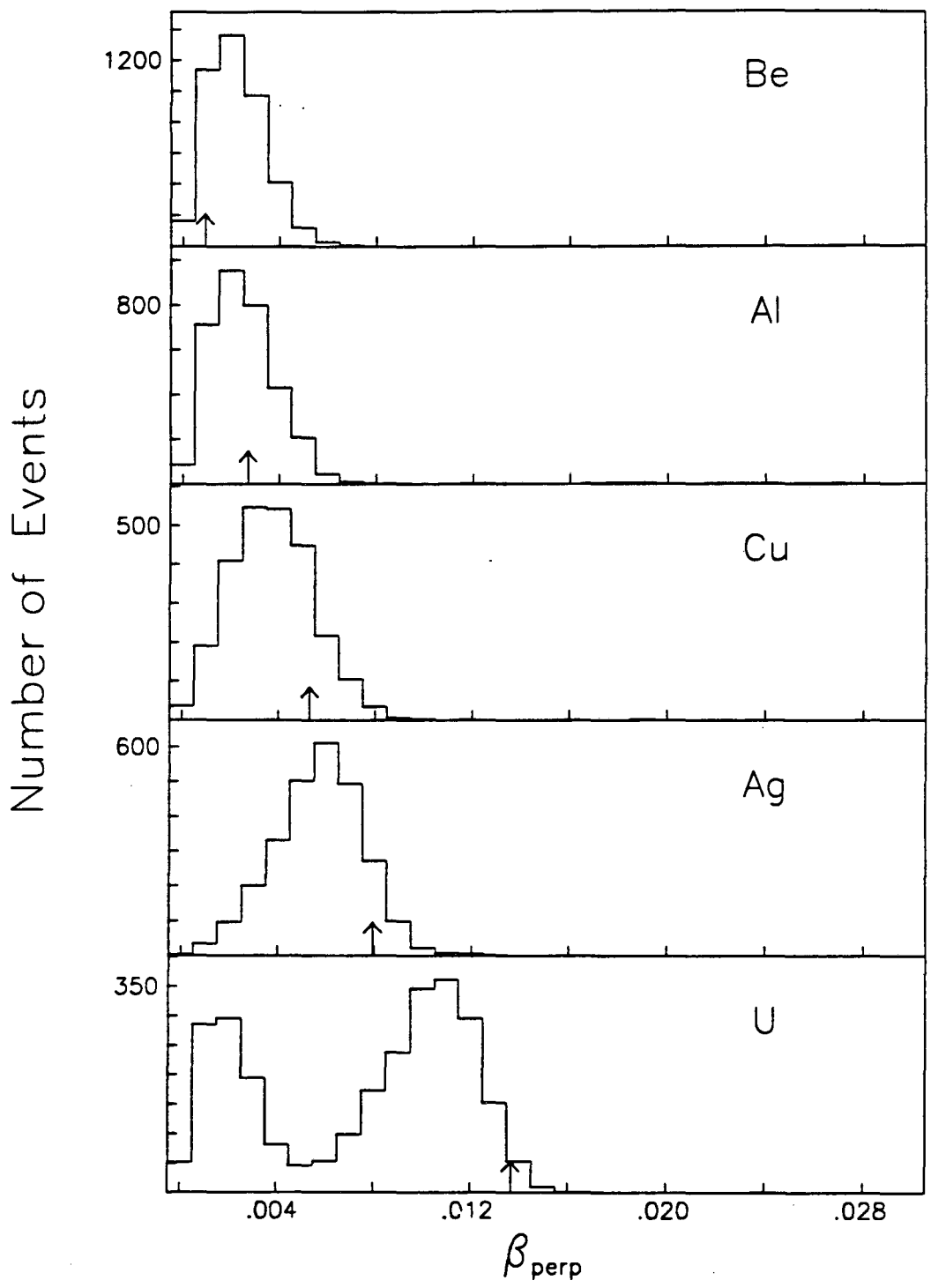

Figure 6.9: Transverse source velocities for $Z_{tot} = 92$, extracted using cold fission masses.

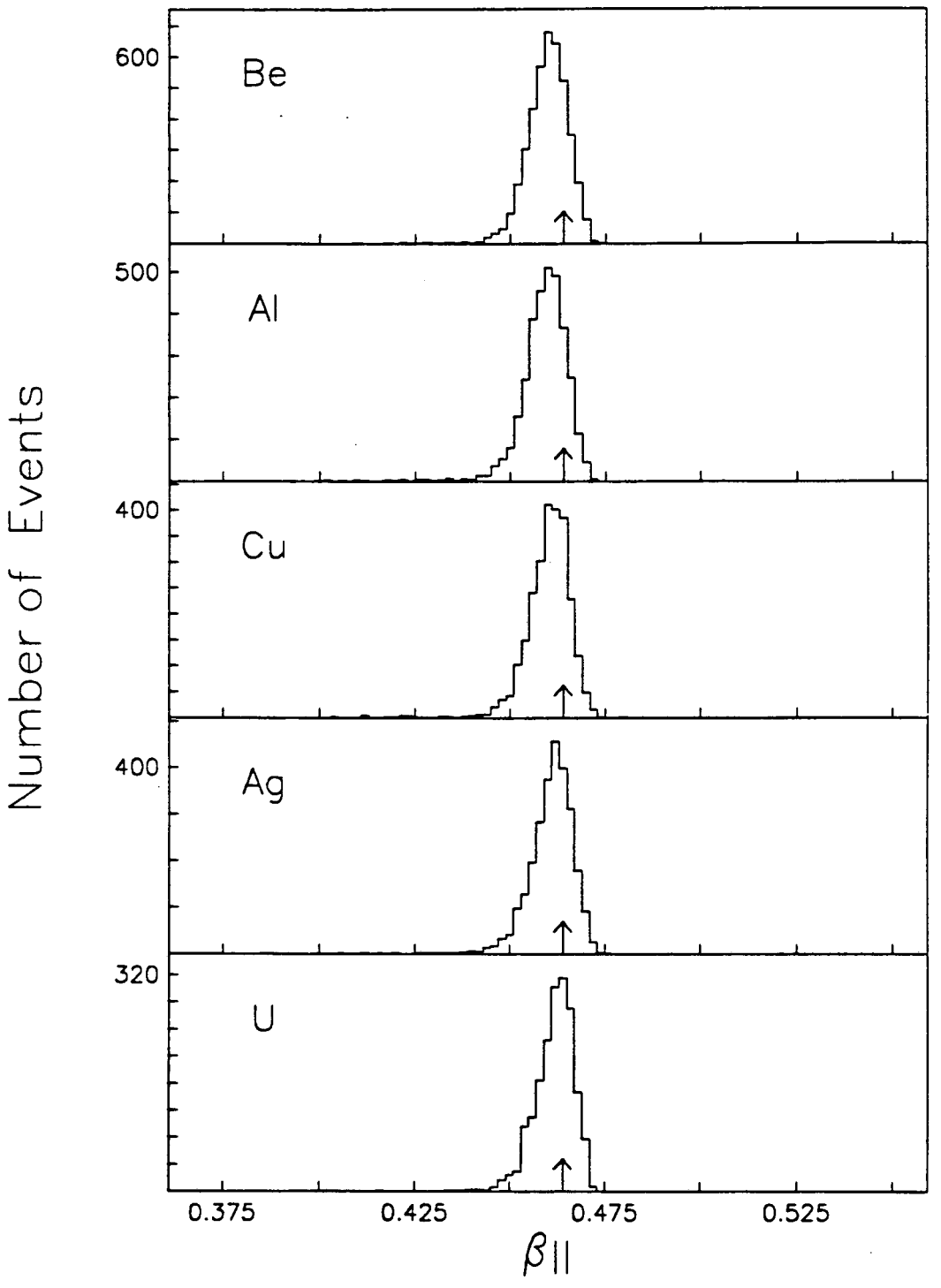

Figure 6.10: Parallel source velocities for $Z_{tot} = 92$, extracted using lighter masses.

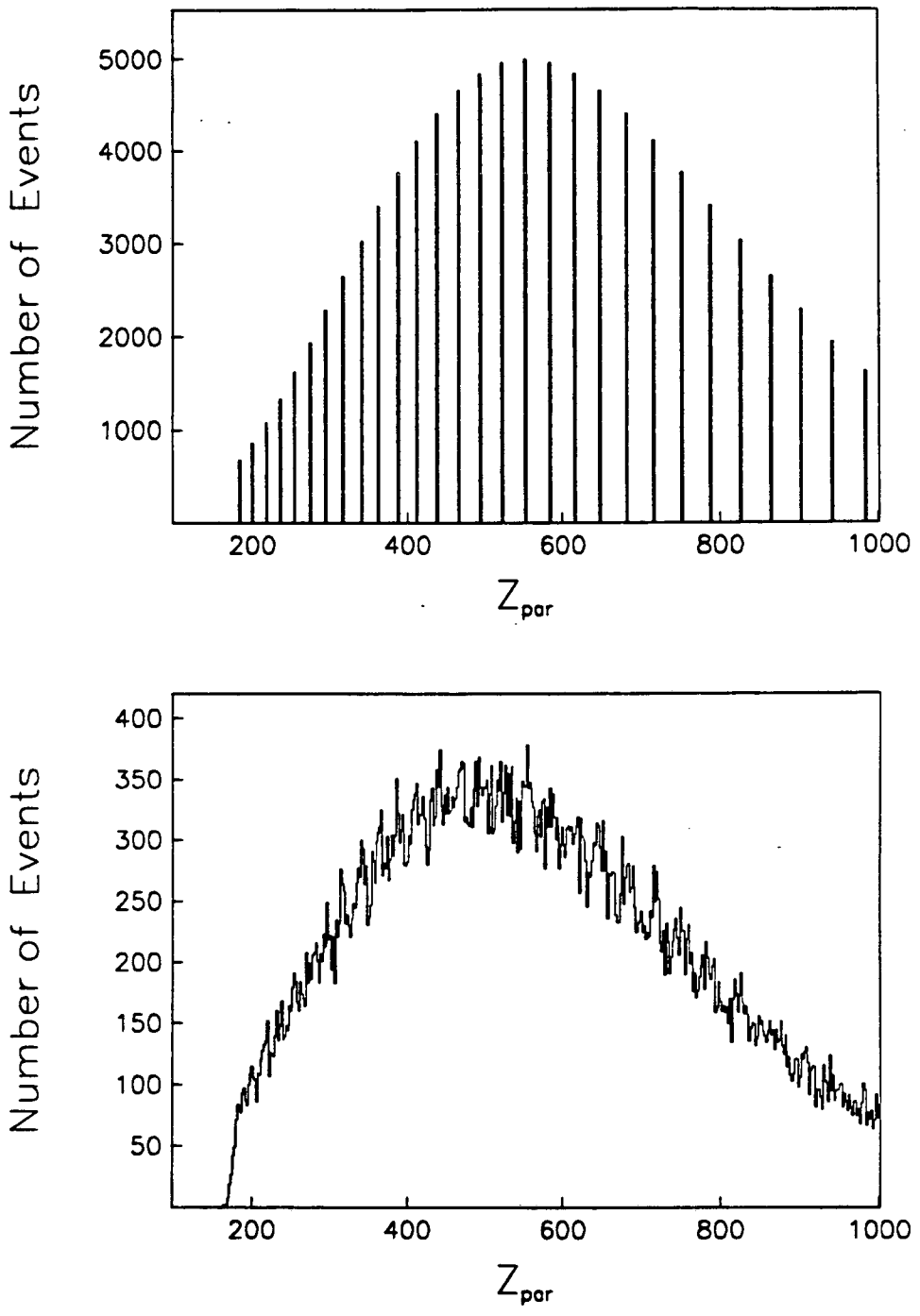

Figure 6.11: Monte Carlo Z_{par} events before and after Gaussian smearing.

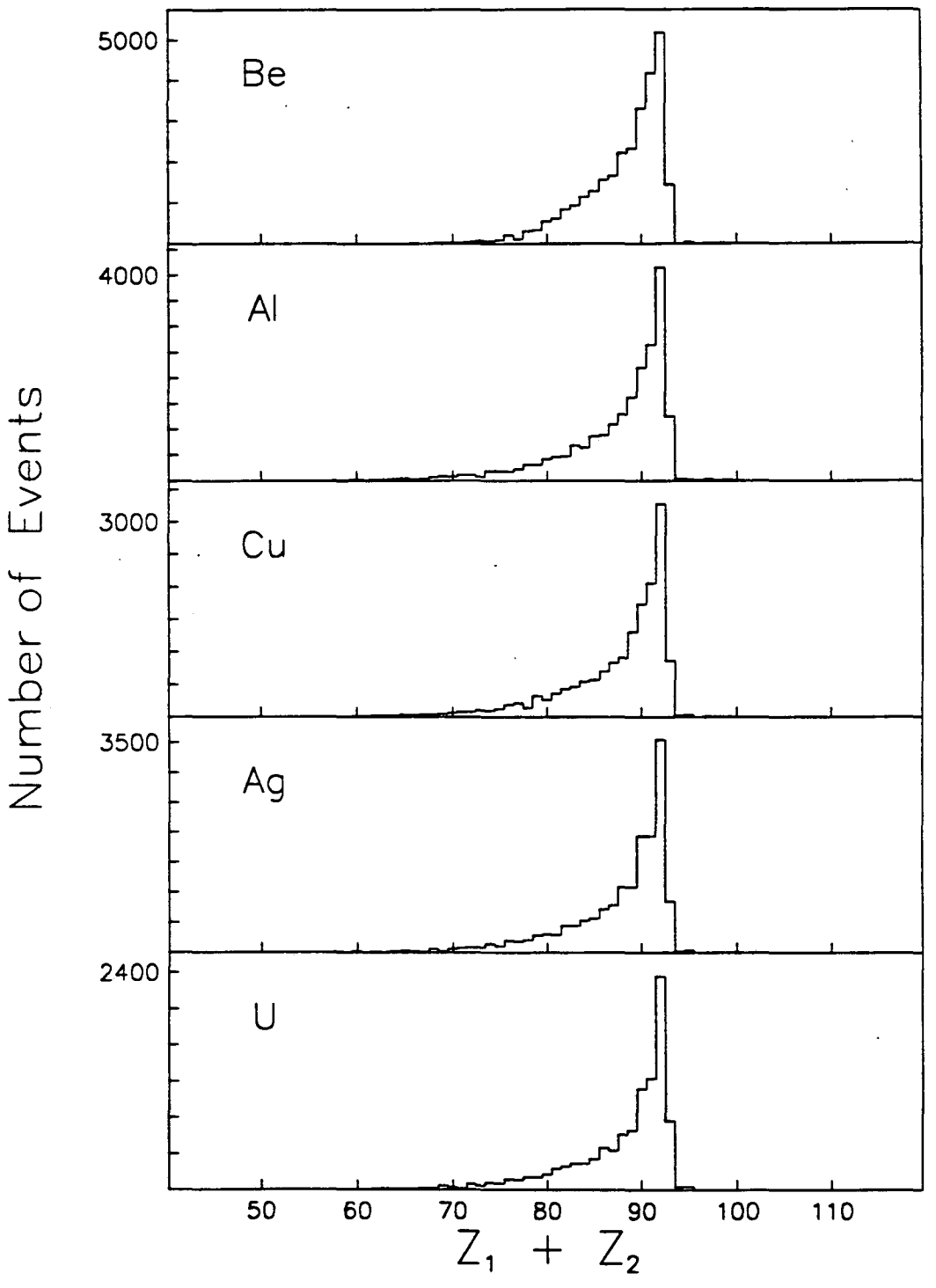

Figure 6.12: $Z_1 + Z_2$ distributions after unfolding.

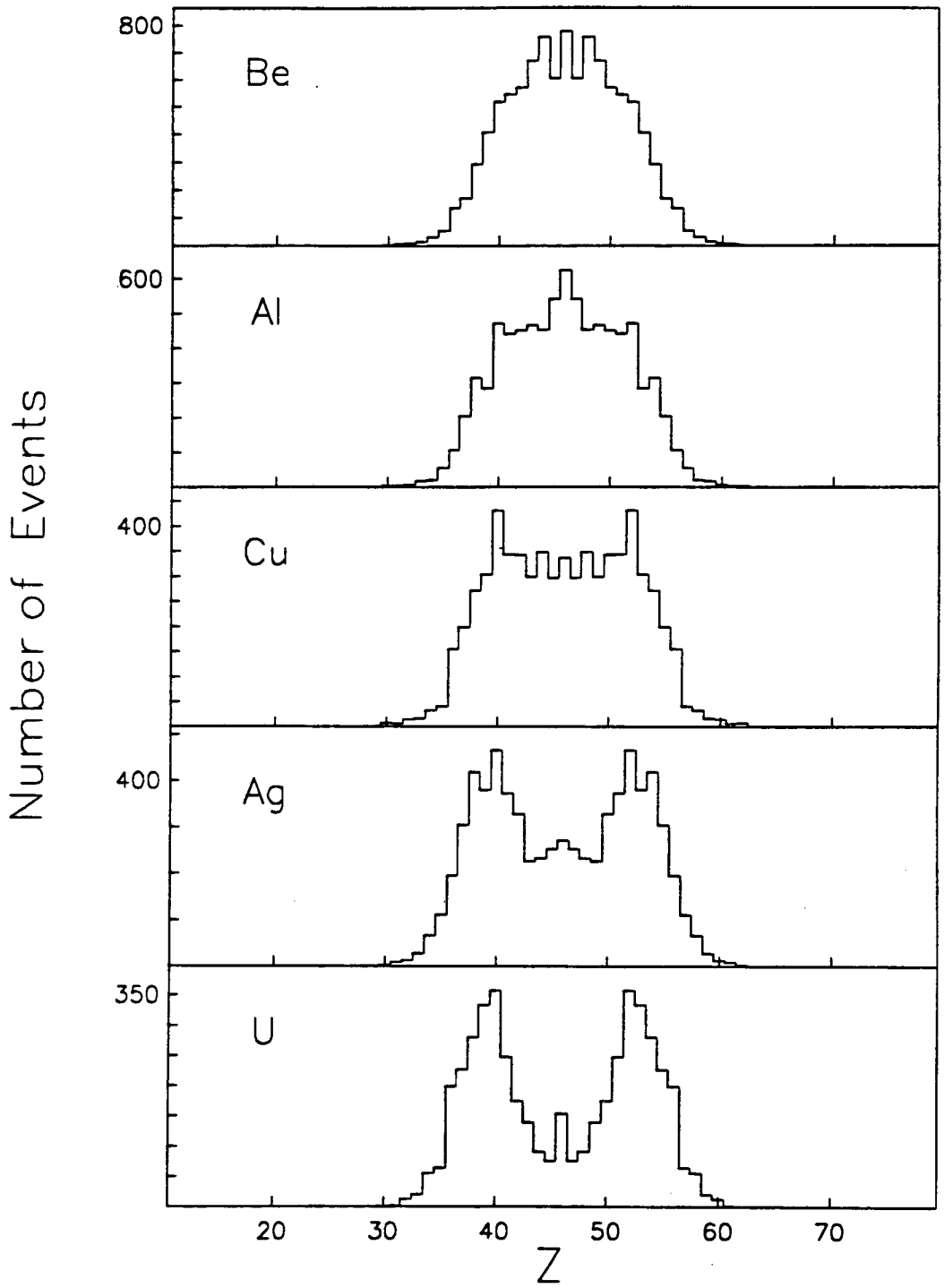

Figure 6.13: Unfolded Z distributions for $Z_{tot} = 92$.

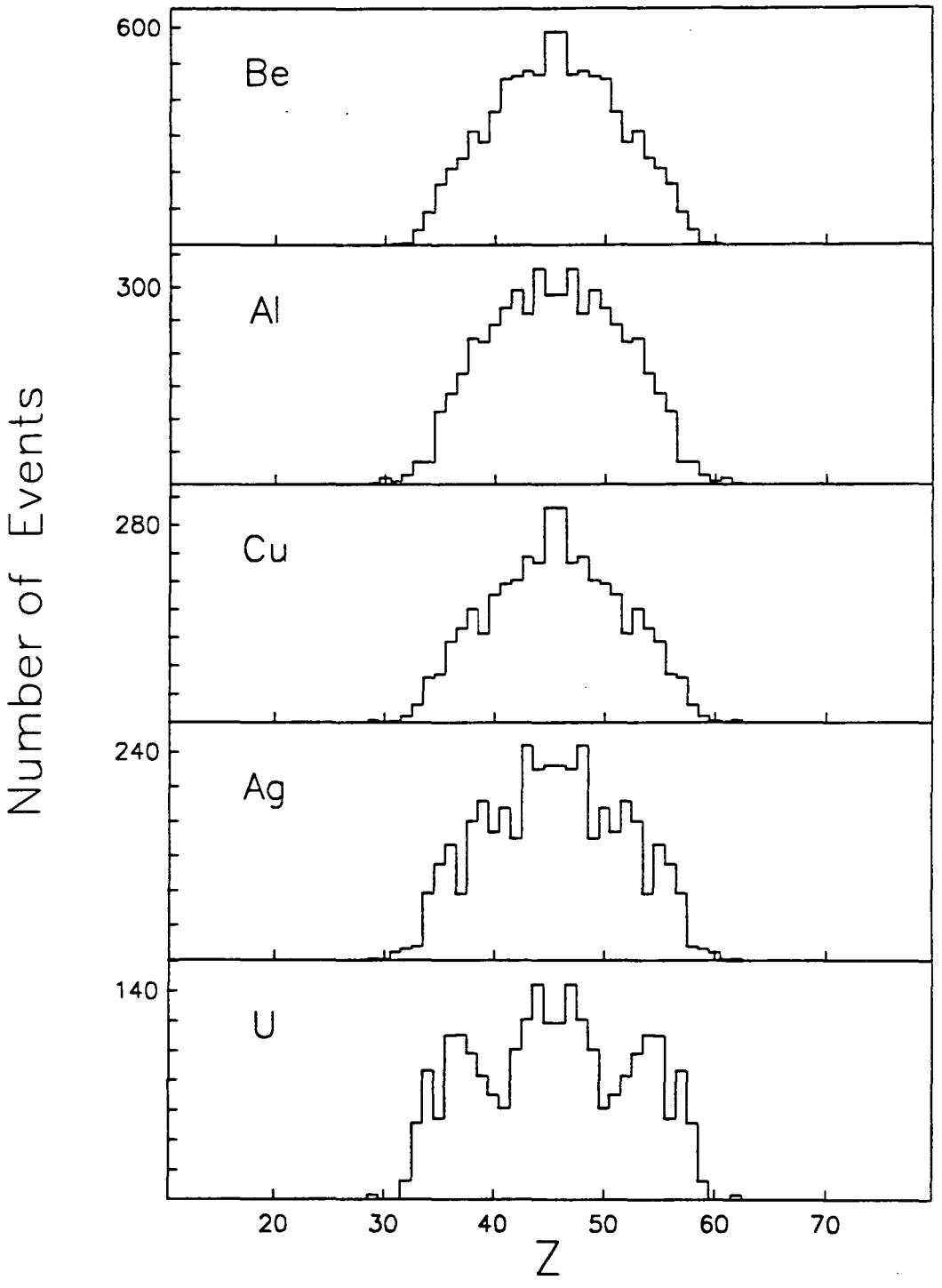

Figure 6.14: Unfolded Z distributions for $Z_{tot} = 91$.

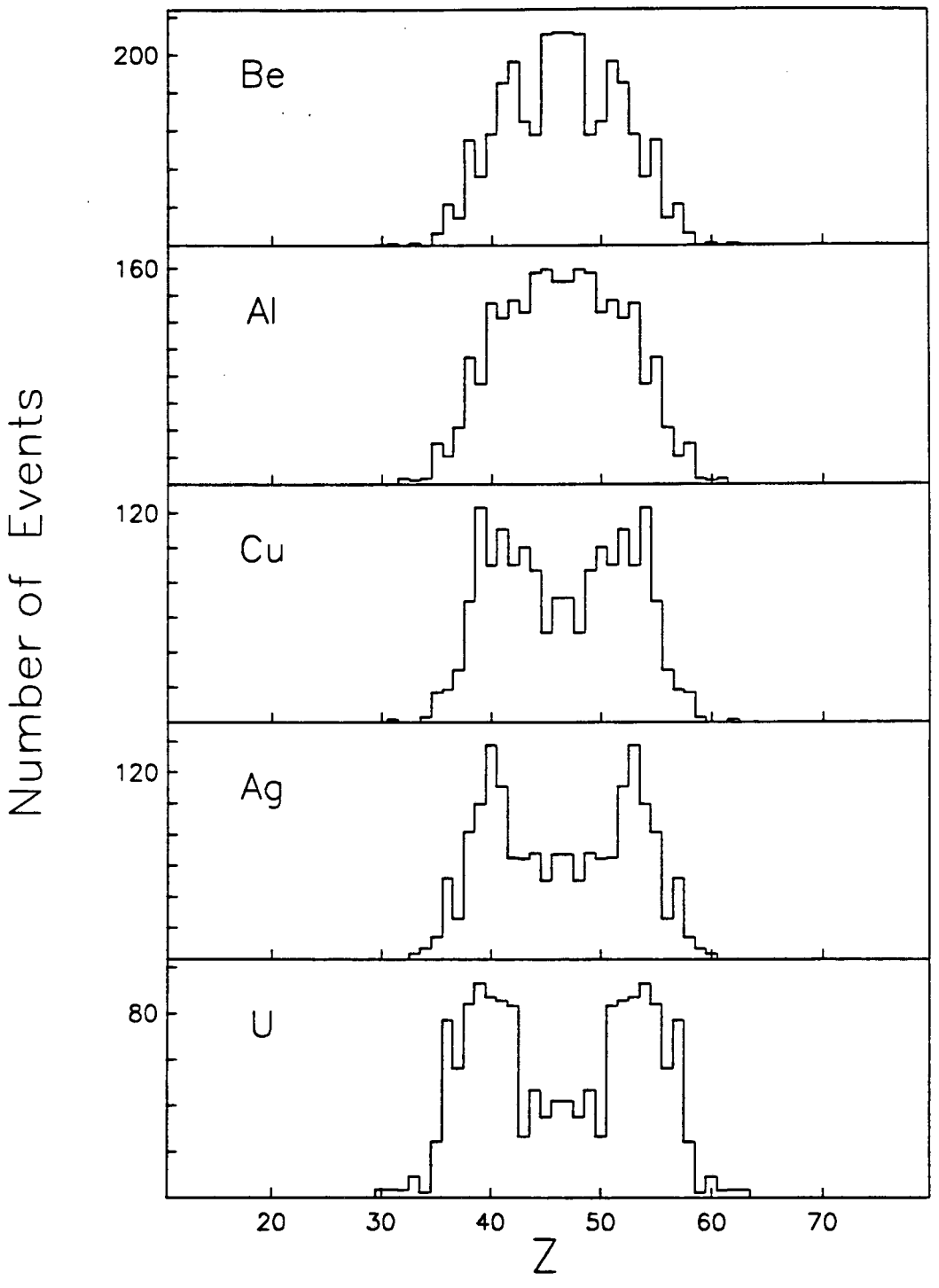

Figure 6.15: Unfolded Z distributions for $Z_{tot} = 93$.

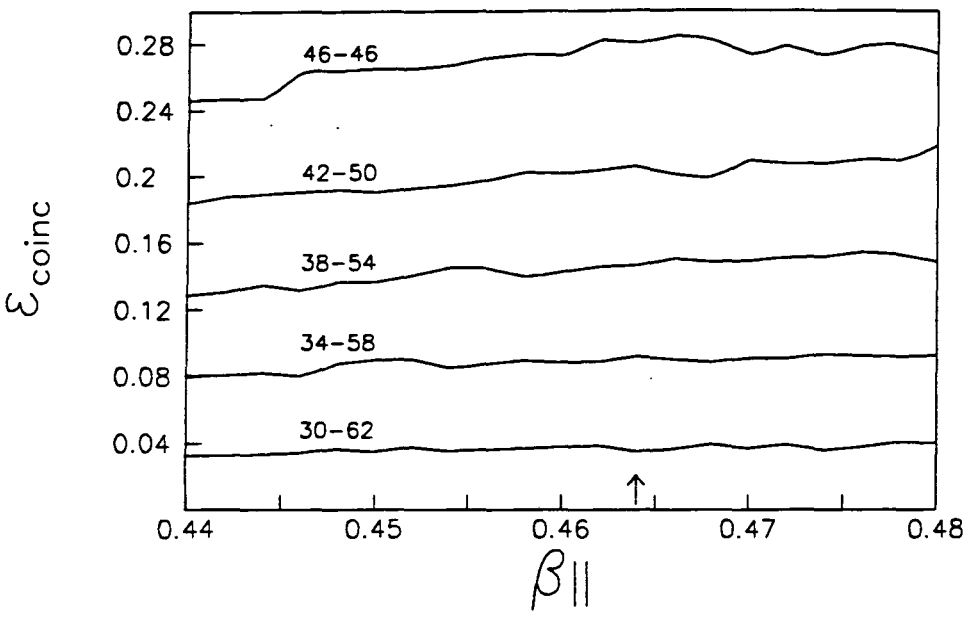

Figure 6.16: Coincidence efficiencies for selected Z_1–Z_2 splits as a function of $\beta_{||}$ at fixed $\beta_\perp = 0$. The arrow marks the beam velocity.

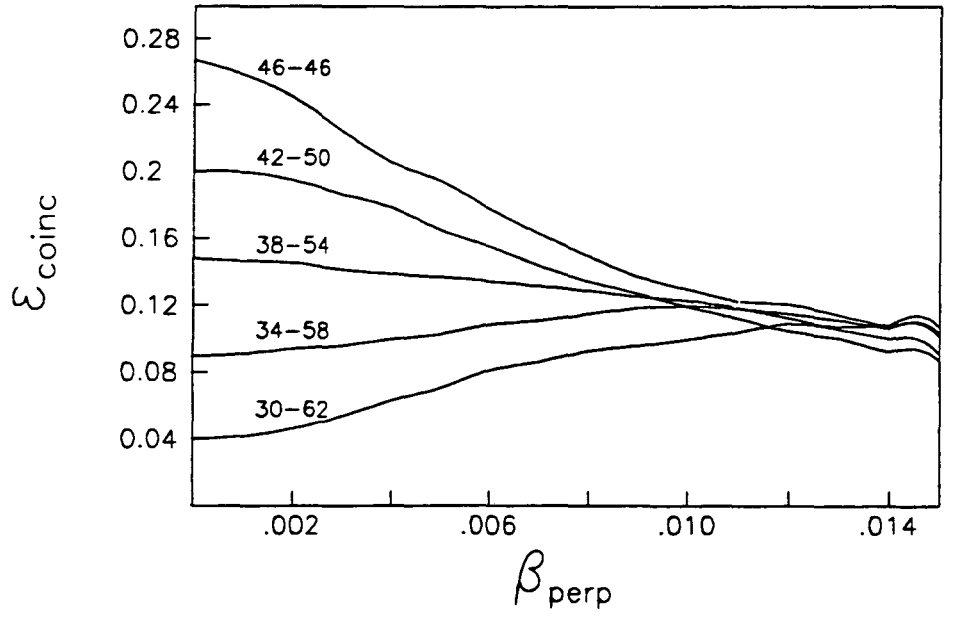

Figure 6.17: Coincidence efficiencies as a function of $\beta_\perp$ at fixed $\beta_{||} = \beta_{\text{beam}}$.

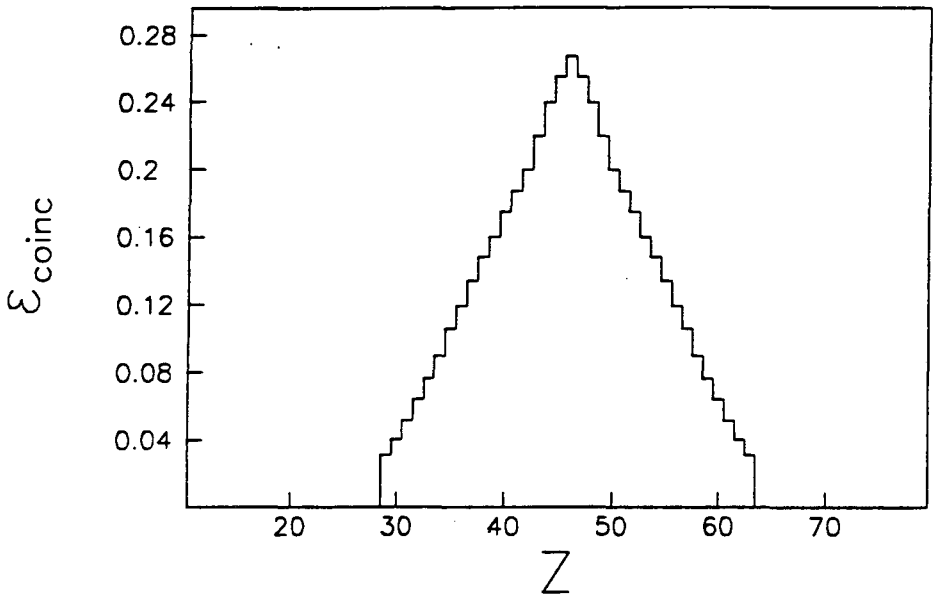

Figure 6.18: Coincidence efficiencies as a function of Z for $Z_{tot} = 92$, $\beta_{||} = \beta_{\text{beam}}$, $\beta_{\perp} = 0$.

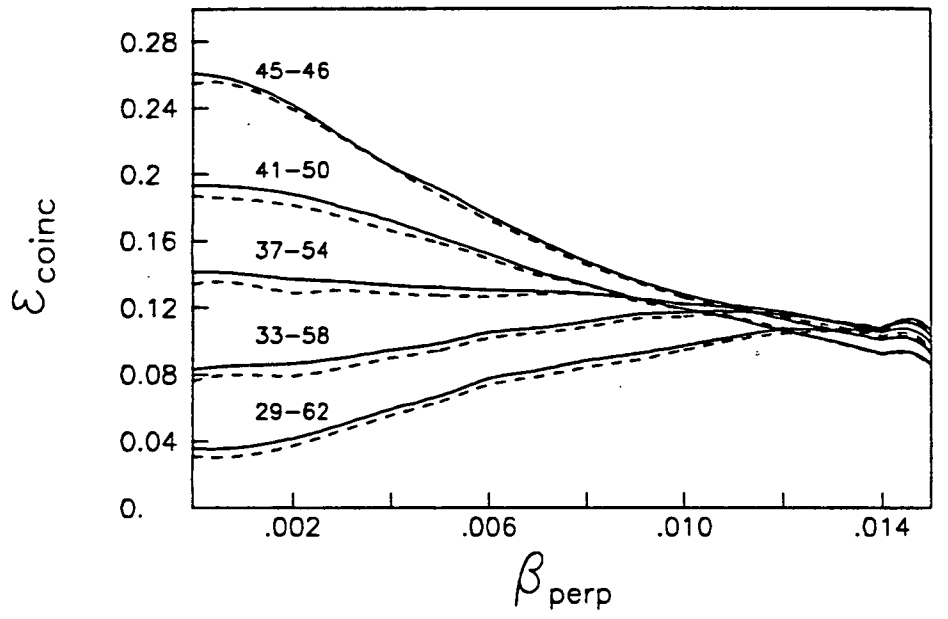

Figure 6.19: Coincidence efficiencies as a function of $\beta_\perp$ for $Z_{tot} = 91$, $\beta_{||} = \beta_{\text{beam}}$. Solid lines are extrapolations from $Z_{tot} = 92$ efficiencies, dashed lines were calculated with the touching spheres model.

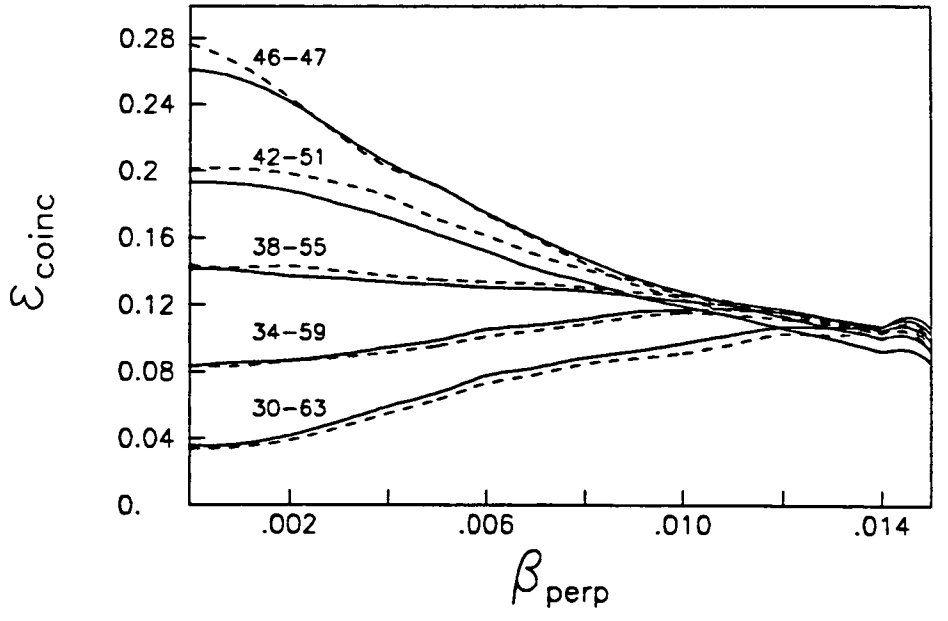

Figure 6.20: Same as Figure 6.19 but for $Z_{tot} = 93$.

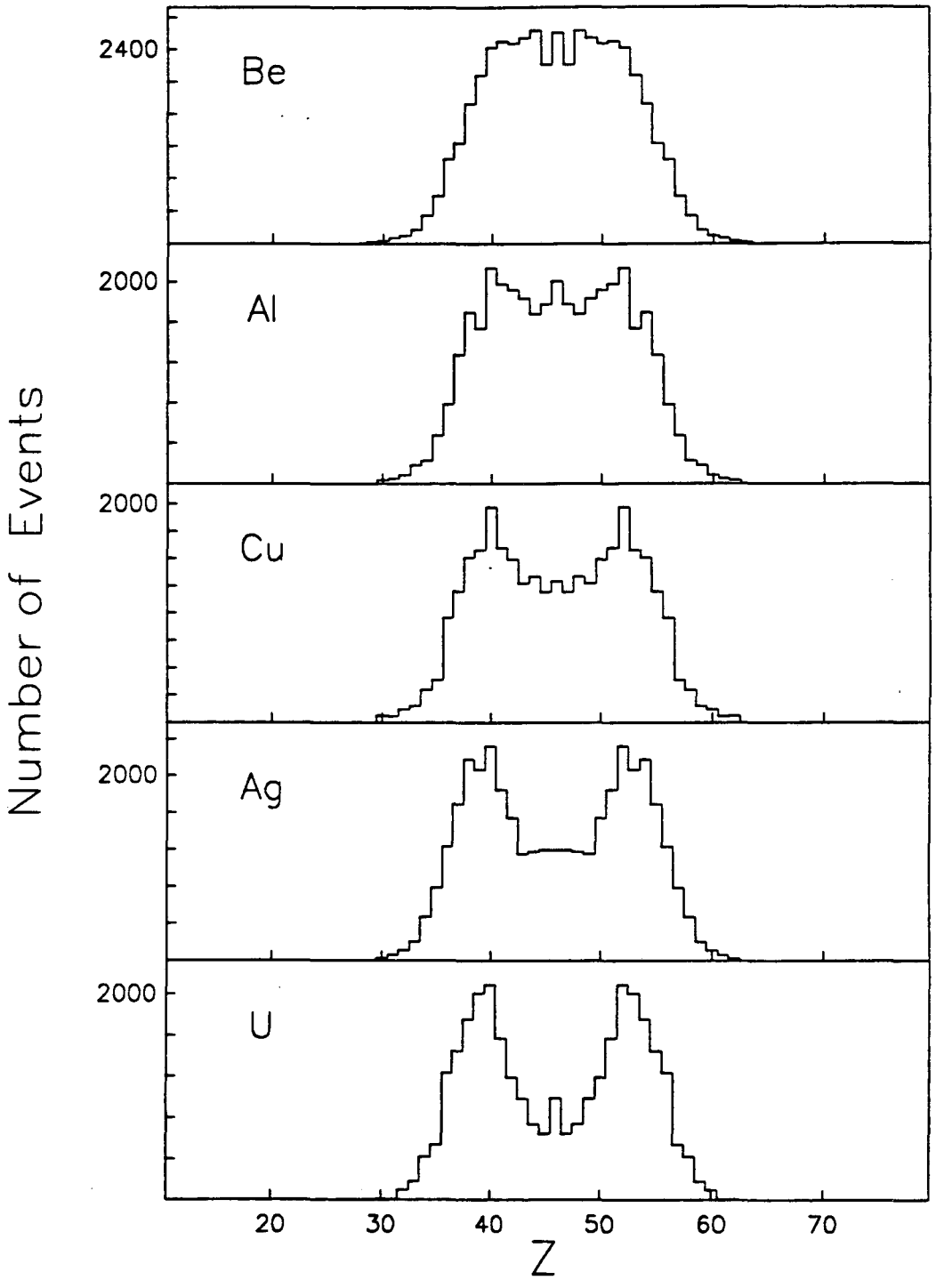

Figure 6.21: Efficiency corrected Z distributions for $Z_{tot} = 92$.

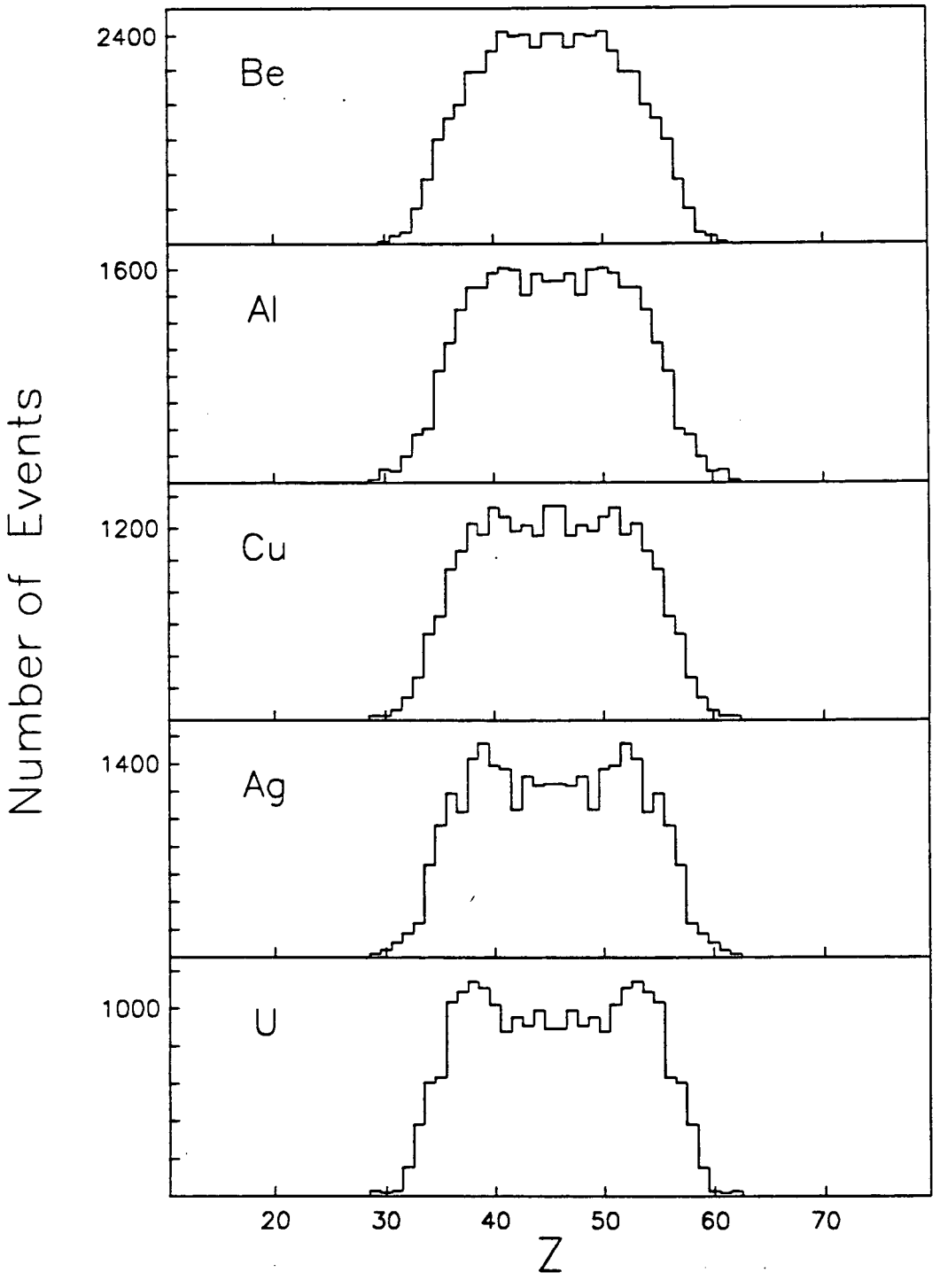

Figure 6.22: Efficiency corrected Z distributions for $Z_{tot} = 91$.

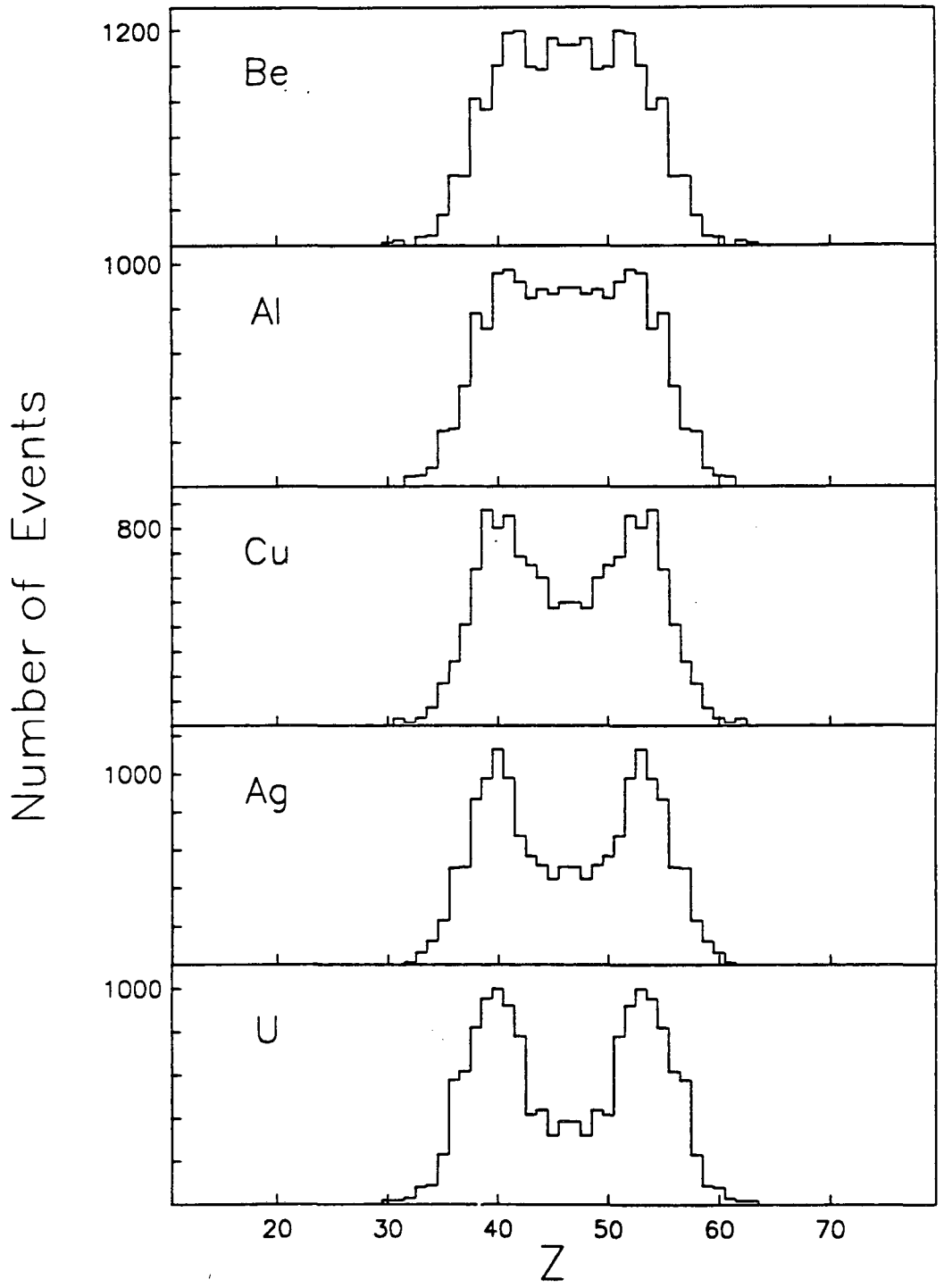

Figure 6.23: Efficiency corrected Z distributions for $Z_{tot} = 93$.

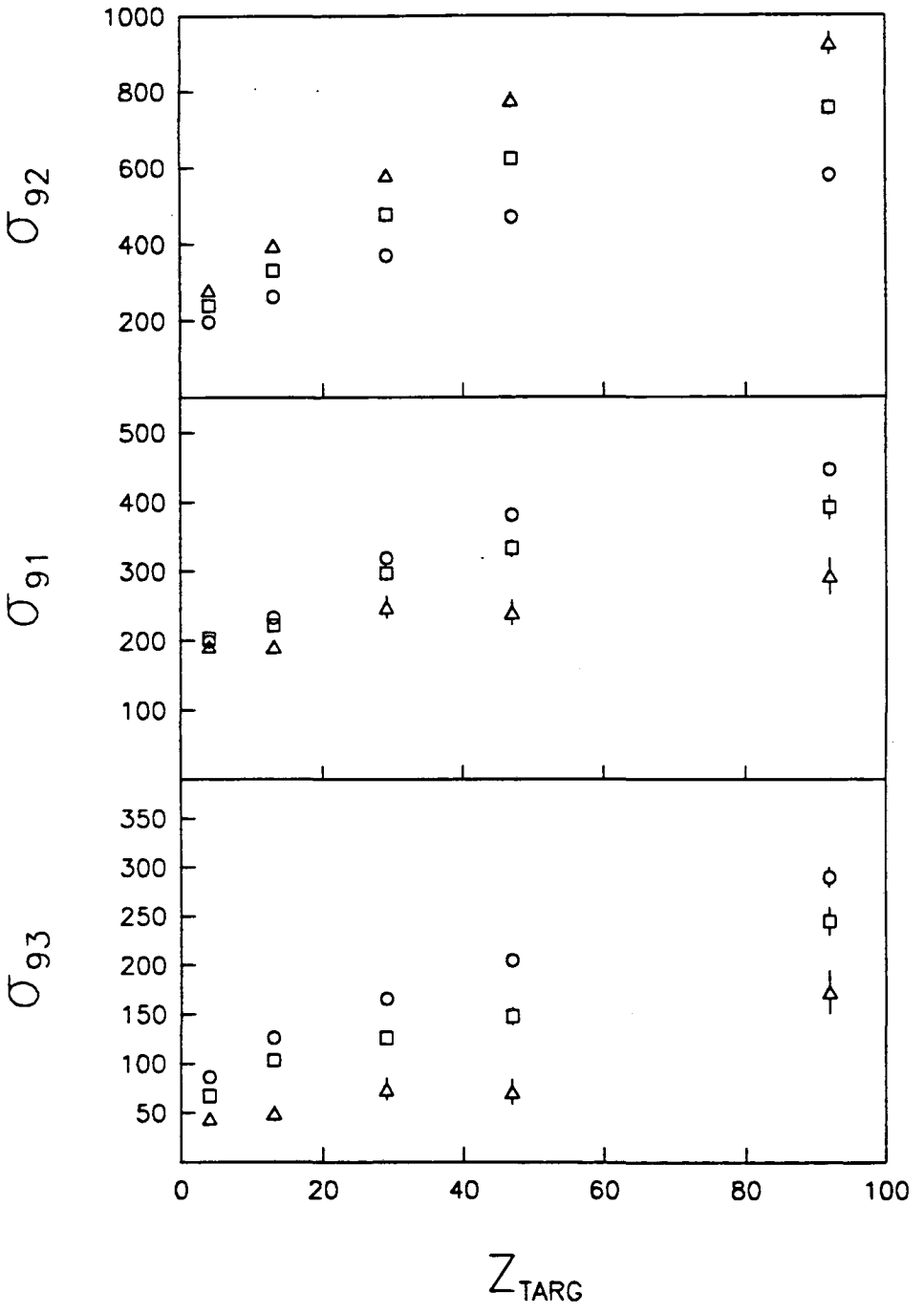

Figure 7.1: Total cross sections in mb for Z_{tot} =92, 91, and 93. The meaning of the symbols is explained in the text.

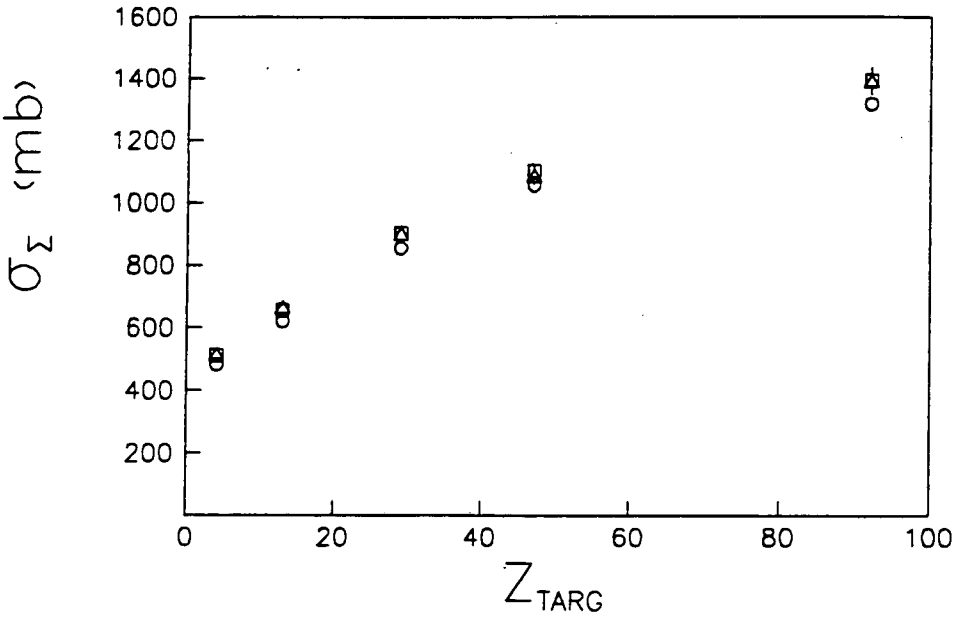

Figure 7.2: Total cross sections for the sum of 92's, 91's and 93's.

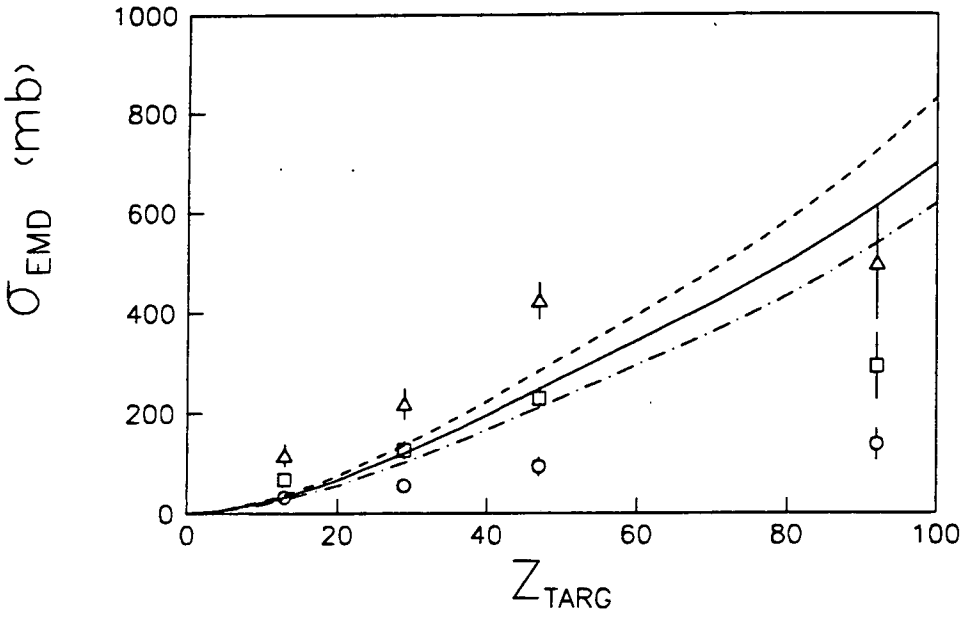

Figure 7.3: Electromagnetic dissociation cross sections extracted with the first method outlined in the text.

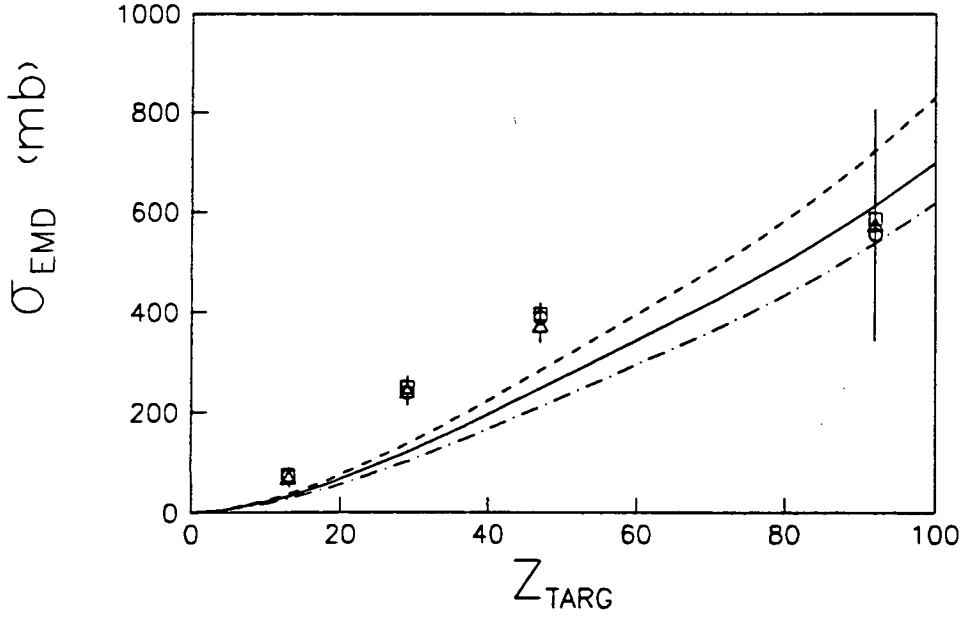

Figure 7.4: Electromagnetic dissociation cross sections extracted with the second method outlined in the text.

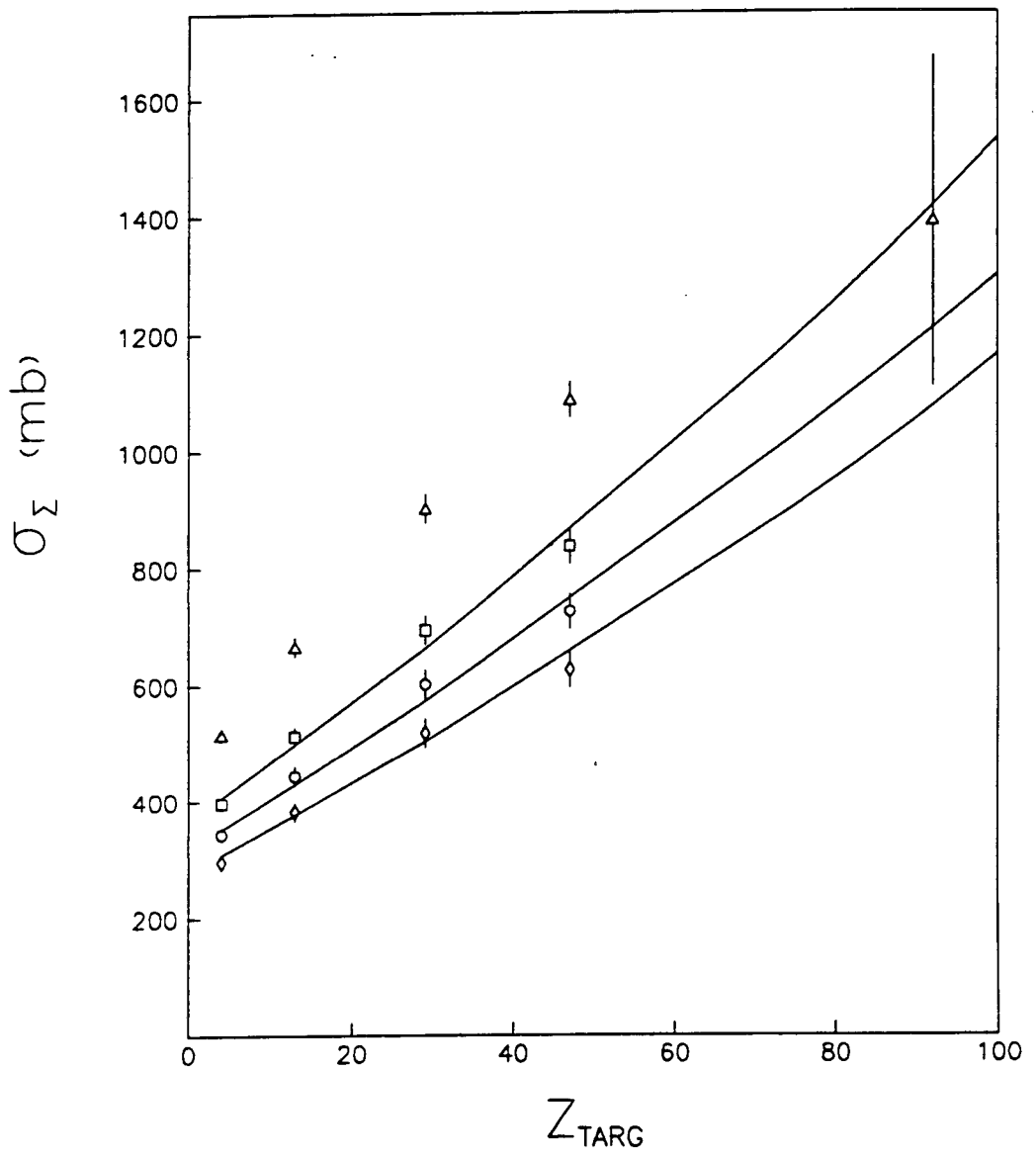

Figure 7.5: Results of the normalization fits.

Bibliography

[1] C.A. Bertulani and G. Baur, Phys. Rep. **163**, 299 (1988).

[2] E. Papageorgiu, Phys. Rev. D **40**, 92 (1989).

[3] C.J. Benesh *et al.*, Phys. Rev. C **40**, 1198 (1989).

[4] E. Fermi, Z. Phys. **29**, 315 (1924).

[5] L.F. Canto *et al.*, Phys. Rev. C **35**, 2175 (1987).

[6] J.W. Norbury, Phys. Rev. C **43**, R368 (1991).

[7] C.F. Weizsäcker, Z. Phys. **88**, 612 (1934).
E.J. Williams, Phys. Rev. **45**, 729 (1934).

[8] J.D. Jackson *Classical Electrodynamics* (Wiley, New York, 1975).

[9] A. Winther and K. Alder, Nucl. Phys. **A319**, 518 (1977).

[10] C.A. Bertulani and G. Baur, Nucl. Phys. **A442**, 739 (1985).

[11] H.L. Bradt and B. Peters, Phys. Rev. **77**, 54 (1950).

[12] G.D. Westfall *et al.*, Phys. Rev. C **19**, 1309 (1979).

[13] P.B. Price *et al.*, Phys. Rev. Lett. **61**, 2193 (1988).

[14] J.T. Caldwell *et al.*, Phys. Rev. C **21** 1215 (1980).

[15] A. Veyssière *et al.*, Nucl. Phys. **A199**, 45 (1973).

[16] A. Van der Woude, Progr. Part. Nucl. Phys. **18**, 217 (1987).

[17] J.S. O'Connell, Proc. Int. Conf. on Photonuclear Reactions and Applications, ed. B.L. Berman (Lawrence Livermore Laboratory, Livermore, CA, 1973) p. 71.

[18] Th. Weber *et al.*, Phys. Rev. Lett. **59**, 2028 (1987).

[19] J.D.T. Arruda-Neto and B.L. Berman, Physica Scripta **40**, 735 (1989).

[20] J.W. Norbury, Phys. Rev. C **41**, 372 (1990).

[21] V.K. Balasubrahmanyan *et al.*, Proc. XII Int. Conf. on Cosmic Rays (Hobart, Tasmania, 1972) p. 1207.

[22] X. Artru and G.B. Yodh, Phys. Lett. **40B**, 43 (1972).

[23] H.H. Heckmann and P.J. Lindstrom, Phys. Rev. Lett. **37**, 56 (1976).

[24] D.L. Olson *et al.*, Phys. Rev. C **24**, 1529 (1981).

[25] M.T. Mercier *et al.*, Phys. Rev. Lett. **52**, 898 (1984).

[26] M.T. Mercier *et al.*, Phys. Rev. C **33**, 1655 (1986).

[27] J.C. Hill *et al.*, Phys. Rev. Lett. **60**, 999 (1988).

[28] J.C. Hill *et al.*, Phys. Rev. C **38**, 1722 (1988).

[29] J.C. Hill *et al.*, Phys. Rev. C **39**, 524 (1989).

[30] C. Brechtmann and W. Heinrich, Z. Phys. A **330**, 407 (1988).

[31] C. Brechtmann and W. Heinrich, Z. Phys. A **331**, 463 (1988).

[32] C. Brechtmann *et al.*, Phys. Rev. C **89**, 2222 (1989).

[33] G. Baroni *et al.*, Nuc. Phys. **A516**, 673 (1990).

[34] J. Barrette *et al.*, Phys. Rev. C **41**, 1512 (1990).

[35] J.T. Walton *et al.*, IEEE Trans. Nucl. Sci. **37** 1578 (1990).

[36] H.J. Crawford, private communication.

[37] P.V. Vavilov, Transl. JETP **5**, 749 (1957).

[38] G.F. Knoll, *Radiation Detection and Measurement* (Wiley, New York, 1979).

[39] J.B. Moulton *et al.*, Nucl. Instr. and Meth. **157**, 325 (1978).

[40] F.S. Goulding and B.G. Harvey, Ann. Rev. Nuc. Sci. **25**, 167 (1975).

[41] W. Reisdorf *et al.*, Nucl. Phys. **A177**, 337 (1971).

[42] R. Vandenbosch and J.R. Huizenga, *Nuclear Fission* (Academic Press, New York, 1973).

[43] R.L. Ferguson *et al.*, Phys. Rev. C **7**, 2510 (1973).

[44] V.E. Viola, Nucl. Data Sect. A **1**, 391 (1966).

[45] R. Vandenbosch *et al.*, Phys. Rev. Lett. **52**, 1964 (1984).

[46] H.G. Pugh *et al.*, Lawrence Berkeley Laboratory Report LBL-22314 (1986).

LAWRENCE BERKELEY LABORATORY
UNIVERSITY OF CALIFORNIA
INFORMATION RESOURCES DEPARTMENT
BERKELEY, CALIFORNIA 94720